FOUNDED 1925
INCORPORATED BY
ROYAL CHARTER 1961

"To promote the advancement of radio, electronics and kindred subjects by the exchange of information in these branches of engineering."

# THE RADIO AND ELECTRONIC ENGINEER

The Journal of the Institution of Electronic and Radio Engineers

VOLUME 39 No. 2 FEBRUARY 1970

## Automatic Test Systems

THE need for more effective testing methods and the question of whether or not automatic systems should be adopted, present a challenge to many engineers. Those concerned with the design, manufacture, quality control, operation and maintenance of complex equipment have an urgent requirement for testing facilities which keep pace with technological advances. Each generation of equipment creates greater demands for higher and more consistent accuracy of measurement, economy in the employment of skilled technicians and reduction of the time taken to complete tests.

Encouraged by more than a decade of experience with automatic check-out equipment in the aircraft, space and missile fields, an increasing number of engineers is considering the use of automatic test systems to help solve their problems. As in all new developments, there have been successes and failures, and there is now an awareness that, before automatic methods can be applied with advantage to specific test requirements, there must be detailed study of all the implications. Engineers and managers realize how necessary it is to establish whether or not an automatic test system is appropriate to their particular needs, before deciding which type of test method to adopt. The number and scope of such studies, on whether and how automatic control can be applied to diverse variable programmed test procedures and performance evaluation, have grown rapidly in the last few years. As the results of these studies become available, we can expect them to make a major impact on all concerned with test and measurement problems.

The time is, therefore, appropriate to review the present state of Automatic Test System development, to study the varied requirements of A.T.S. users and potential users, to consider the problems faced by all those affected by the introduction of A.T.S., and to survey the probable direction of future development.

The main purpose of the I.E.R.E. Conference on 'Automatic Test Systems', to be held at the University of Birmingham from 13th to 17th April, is to arouse interest and stimulate thought on a subject of major importance. The provisional programme published in the January issue of the *Journal* shows that it will cover a very wide field including factual reviews of A.T.S. experience, future requirements and how such requirements are determined by major users, descriptions of A.T.S. developments, the management of A.T.S. and surveys of some new techniques which are being applied to automatic testing. The subject covers a broad band of engineering disciplines and for this reason the association of the Institutions of Electrical, Mechanical and Production Engineers and the Royal Aeronautical Society, as well as the support of the U.K. Automation Council, is particularly appropriate.

Of necessity, resulting from the continually increasing use of complex equipments, testing methods are in the throes of change. Automated methods of testing are not appropriate in every case but in others they can help to meet many of the stringent test requirements, which engineers of varied disciplines now face. Automatic Test Systems require careful planning and will not be achieved overnight, but much progress has already been made and the future is bright with promise.

R. KNOWLES

# INSTITUTION NOTICES

### Institution Dinner 1970

An Institution Dinner will be held in the Egyptian Hall at the Mansion House in the City of London on Tuesday, 12th May next, in the presence of the Right Honourable the Lord Mayor of London.

A further announcement about the arrangements will be made shortly. Members are however asked to note that tickets for personal guests will be strictly limited in number and that it will not be possible for ladies to be invited on this occasion.

### Change of Telephone Number

The Institution's telephone number has been changed to:

01-637 2771

(The 01—code prefix should only be used when calling from outside the London area.)

There are now ten incoming exchange lines to the PBX and callers should not experience the difficulties which occasionally were found when seven lines on two separate exchanges were available.

### Collaboration on Composite Engineering Register

In September 1969 a working party under the chairmanship of Sir Arnold Lindley was formed to implement a C.E.I. Board resolution to establish an Authority for registration qualification and title in the engineering community. In December C.E.I. convened a meeting of representatives of organizations interested in collaborating with them and there has been a useful exchange of views. The two principal items discussed at the meeting were standards of qualification, and structure of the Authority.

Standards proposed by the Standing Conference for National Qualification and Title for technician engineers and engineering technicians were favourably received as a basis for resolving the requirements of Bodies for entry to the new register. C.E.I. proposals for the structure of the new single Authority were considered in broad terms in which the three principal sections of the engineering community concerned, namely chartered engineers, technician engineers and engineering technicians, could subscribe to a common register set up through the medium of the Royal Charter of C.E.I.

It was agreed that a further working party consisting of representatives from C.E.I., S.C.N.Q.T., C.S.T.I. (Council of Science and Technology Institutes) and other interested bodies will be set up to develop proposals for the structure of the Authority so that it can be established as soon as possible.

### Reduced Rates for Publications of Other Institutions

A reciprocal exchange agreement has been concluded between the Institution and the Institute of Electrical and Electronics Engineers, Inc., whereby members of either body may subscribe to publications of the other at reduced rates. The rates to I.E.R.E. members for I.E.E.E. publications are equivalent to the library discount rate rather than the full non-member rate and are:

*I.E.E.E. Spectrum* $21.60.

*Proceedings of the I.E.E.E.* $32.40.

*Transactions* and *Journals:* The reduced rates for these 33 different publications range from $16.20 to $37.80 and members are advised to write for details to I.E.E.E. Subscriber Relations.

All payments and inquiries should be made to I.E.E.E. Subscriber Relations, 345 East 47 Street, New York, N.Y., U.S.A., 10036.

* * *

Members are asked to note that specially reduced subscriptions of 50% of the normal non-member customer's rates apply to the following I.E.E. publications:

*Current Papers in Physics* (*CPP*) £6

*Current Papers in Electrical and Electronic Engineering* (*CPE*) £6

*Current Papers on Computers and Control* (*CPC*) £5

The 25% reduction for I.E.R.E. members in respect of other I.E.E. publications applies as indicated in the November issue of *The Radio and Electronic Engineer* (page 250). Orders for all I.E.E. publications should be sent through the Publications Department of the I.E.R.E., 9 Bedford Square, London, W.C.1.

### Non-destructive Testing

The British National Committee for Non-Destructive Testing is collecting information on the specific application of non-destructive testing methods in industry with a view to drawing attention to economies and other advantages which may be derived from their use. It is proposed to use this information to encourage more widespread development of industrial application of these methods.

The Committee would appreciate the co-operation of readers who know of any case histories of particular applications of non-destructive testing which have resulted in improvements in design or economies in production and they are asked to send this information to: E. P. Davies, Esq., C.Eng., M.I.Mech.E., Secretary, B.N.C. for Non-Destructive Testing, 1 Birdcage Walk, Westminster, London S.W.1.

# Interconnexion of Frequency-Division and Time-Division Multiplex Transmission Systems

*By*

**Professor J. E. FLOOD,**
D.Sc., C.Eng., F.I.E.E., F.I.E.R.E.†

and

**A. C. PONDER,**
B.Sc., A.Inst.P.‡

Multichannel transmission systems are of two general types: frequency-division multiplex (f.d.m.) and time-division multiplex (t.d.m.). In order to interconnect a t.d.m. system with an f.d.m. system, it is not necessary to demodulate each channel to audio frequencies. An amplitude-modulated t.d.m. signal can be converted to f.d.m. by gating it to a bank of band-pass filters, each passing one harmonic of the pulse repetition frequency (p.r.f.). The output of these filters are connected to a common path to provide an f.d.m. signal. An f.d.m. signal can be converted to t.d.m. by separating the channels with band-pass filters and sampling the output of each filter with a pulse occupying a different position in the t.d.m. cycle. The sampled outputs are connected to a common path to provide an amplitude-modulated t.d.m. signal. It is necessary, however, for the carrier frequencies of the f.d.m. system to be harmonics of the p.r.f. of the t.d.m. system.

It is shown that resonant-transfer can be used to reduce energy losses in the conversion and so eliminate amplifiers. This has been demonstrated experimentally.

## List of Principal Symbols

$A$ amplitude of carrier wave
$B_n$ coefficient in Fourier series
$f_r$ pulse repetition frequency
$f_b$ mid-band frequency of filter
$f_c$ frequency of carrier wave
$f_m$ frequency of modulating signal
$F_m$ maximum value of $f_m$
$m$ modulation factor
$S$ duty ratio of pulse train
$T$ period of pulse train
$t_0$ duration of switch closure
$v_c$ carrier wave
$v_m$ modulating signal
$v_L$ lower-sideband signal
$v_U$ upper-sideband signal
$v_1$ modulated carrier wave
$v_2$ double-sideband suppressed-carrier signal
$v_3$ unipolar pulse train
$v_4$ amplitude-modulated unipolar pulse train
$v_5$ amplitude-modulated bipolar pulse train
$\phi$ phase angle
$\omega_b = 2\pi f_b$; $\omega_c = 2\pi f_c$;
$\omega_m = 2\pi f_m$; $\omega_r = 2\pi f_r$;
$\omega_0 = \pi/t_0$

† Formerly with Associated Electrical Industries Ltd., Telecommunications Division; now at the Department of Electrical Engineering of The University of Aston in Birmingham.

‡ Formerly with Associated Electrical Industries Ltd.; now a consultant.

## 1. Introduction

Multi-channel transmission systems are of two general types: frequency-division multiplex (f.d.m.) systems and time-division multiplex (t.d.m.) systems. In an f.d.m. system, each channel modulates a carrier wave of different frequency so that it occupies a separate frequency band on the common transmission path as shown in Fig. 1(b). In a t.d.m. system,[1] each channel modulates a pulse occurring at a different time in a periodic cycle as shown in Fig. 1(d). Thus, each channel uses practically the whole bandwidth of the common transmission path, but only for a fraction of the time. In order to interconnect a t.d.m. system with an f.d.m. system, it would appear necessary to demodulate each channel to audio frequencies. Figure 2 shows a t.d.m. system and an f.d.m. system interconnected in this way.

In recent years, attention has been given to the design of cheap multiplexing systems to permit the use of multichannel transmission over junction cables between exchanges. Some of these systems use f.d.m.[2,3,4] However, t.d.m. transmission using pulse-code modulation (p.c.m.)[5,6,7] has now been adopted. The use of p.c.m. for telephone switching has also been studied.[8,9] The use of t.d.m. for local switching and short-distance transmission, together with f.d.m. transmission for long-distance transmission will necessitate the interconnexion of systems using these two different forms of multiplexing. Economies should be obtainable if it is possible to convert a pulse-modulated waveform to a modulated carrier wave, and vice-versa, without having to demodulate to audio frequencies, and remodulate each time, as shown in Fig. 2.

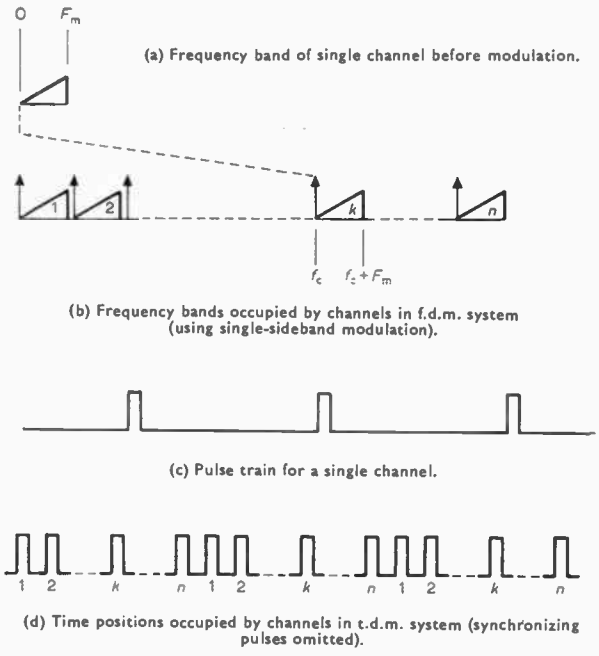


**Fig. 1.** Basic principles of frequency-division and time-division multiplexing.

The simplest method of time-division multiplexing uses pulse-amplitude modulation (p.a.m.). Other forms of pulse modulation are often used for transmission, but these are usually produced by methods that involve p.a.m. as an intermediate stage.[1] Frequency-division multiplexing systems also usually use amplitude modulation (a.m.). If another modulation method (e.g. frequency modulation) is required for the transmission path, this is usually performed on the wide-band signal comprising all the channels after they have been multiplexed using a.m. It is thus only necessary to consider methods of converting between t.d.m. using p.a.m. and f.d.m. using a.m.

## 2. Amplitude Modulation of a Carrier Wave

### 2.1. *Simple Double-sideband Modulation*

If the carrier wave is given by

$$v_c = A \cos \omega_c t \qquad \ldots\ldots(1)$$

is amplitude modulated by the signal

$$v_m = m \cos (\omega_m t + \phi) \qquad \ldots\ldots(2)$$

the output is given by:

$$\begin{aligned} v_1 &= v_c(1+v_m) \\ &= A \cos \omega_c t + \tfrac{1}{2}mA\{\cos [(\omega_c+\omega_m)t+\phi] + \\ &\qquad + \cos [(\omega_c-\omega_m)t-\phi]\} \qquad \ldots\ldots(3) \end{aligned}$$

The a.m. output signal thus comprises the original carrier frequency ($\omega_c$) together with upper and lower side-band frequencies ($\omega_c+\omega_m$ and $\omega_c-\omega_m$).

### 2.2. *Double-sideband Suppressed-carrier Modulation*

If a balanced form of modulator is used, the carrier frequency is eliminated from the output. The output signal (after passing through a band-pass filter to select a pair of side-bands) is then

$$\begin{aligned} v_2 &= v_c . v_m \\ &= \tfrac{1}{2}mA\{\cos [(\omega_c+\omega_m)t+\phi] + \\ &\qquad + \cos [(\omega_c-\omega_m)t-\phi]\} \qquad \ldots\ldots(4) \end{aligned}$$

### 2.3. *Single-sideband (s.s.b.) Modulation*

If the carrier is eliminated by a balanced modulator and one sideband is selected by a band-pass filter, the

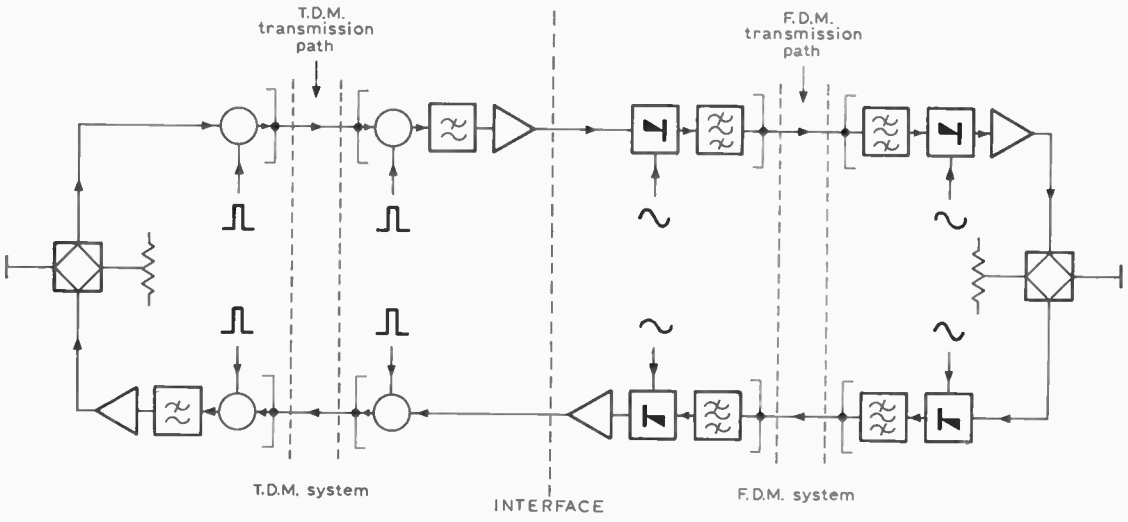


**Fig. 2.** Interconnexion of f.d.m. system and t.d.m. system by demodulating to audio frequencies.

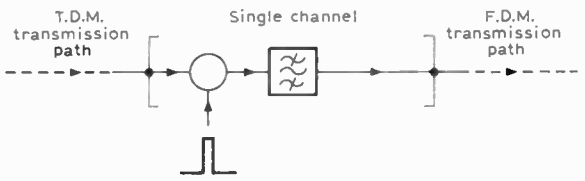


Fig. 3. Circuit for conversion from t.d.m. to f.d.m.

output signal is given by

$$v_L = \tfrac{1}{2}mA \cos [(\omega_c - \omega_m)t - \phi] \quad \text{.....(5a)}$$

or

$$v_U = \tfrac{1}{2}mA \cos [(\omega_c + \omega_m)t + \phi] \quad \text{.....(5b)}$$

depending on whether the upper or the lower sideband is selected.

## 3. Amplitude Modulation of a Pulse Train

### 3.1. Unipolar Pulse-amplitude Modulation

An unmodulated unipolar pulse train with a p.r.f. of $\omega_r/2\pi$ may be represented by a Fourier series

$$v_3 = B_0 + 2\sum_{n=1}^{\infty} B_n \cos n\omega_r t \quad \text{.....(6)}$$

where the coefficients $B_n$ are determined by the length and shape of the pulses. For example, if all the pulses are rectangular, are of unit height, and have a duty ratio $S$:

$$B_0 = S \text{ and } B_n = \frac{\sin n\pi S}{n\pi} \quad \text{.....(7)}$$

If the pulse train given by eqn. (6) is modulated by the signal given by eqn. (2), the output is given by

$$\begin{aligned} v_4 &= v_3(1 + v_m) \\ &= B_0[1 + m \cos (\omega_m t + \phi)] + \\ &\quad + \sum_{n=1}^{\infty} B_n\{2 \cos n\omega_r t + m \cos [(n\omega_r + \omega_m)t + \phi] + \\ &\qquad + m \cos [(n\omega_r - \omega_m)t - \phi]\} \end{aligned} \quad \text{.....(8)}$$

The p.a.m. output signal thus comprises d.c. and audio components, harmonics of the p.r.f. ($n\omega_r$), and upper and lower sideband frequencies about each harmonic ($n\omega_r + \omega_m$ and $n\omega_r - \omega_m$). If the lower sideband of the $n$th harmonic is not to overlap the upper sideband $(n-1)$th harmonic, we require

$$(n-1)\omega_r + \omega_m < n\omega_r - \omega_m, \quad \text{i.e. } \omega_m < \tfrac{1}{2}\omega_r \quad \text{.....(9)}$$

The highest usable modulating frequency $F_m$ is therefore half the p.r.f., which is consistent with the Sampling Theorem. The output signal given by eqn. (8) is analogous to simple double-sideband a.m., as the original carriers (given by eqn. (6)) are present in the output. The modulation is superimposed on a train of 'pedestal' pulses which are present even when there is no modulating signal (i.e. $m = 0$).

### 3.2. Bipolar Pulse-amplitude Modulation

It is possible to design a pulse modulator that does not produce an output pedestal. The height of the output pulses can then be directly proportional to the instantaneous signal values, thus producing both positive and negative pulses. This bipolar output signal is given by:

$$\begin{aligned} v_5 &= v_3 v_m \\ &= mB_0 \cos (\omega_m t + \phi) + \\ &\quad + m\sum_{n=1}^{\infty} B_n\{\cos [(n\omega_r + \omega_m)t + \phi] + \\ &\qquad + \cos [n\omega_r - \omega_m)t - \phi]\} \end{aligned} \quad \text{.....(10)}$$

This output signal is thus analogous to double-sideband suppressed-carrier modulation (c.f. eqn. (4)).

## 4. T.D.M. to F.D.M. Conversion

The modulated pulse train of a single channel (Fig. 1(c)) may be extracted from the complete signal of a t.d.m. system (Fig. 1(d)) by means of a correctly-timed gate, as shown in Fig. 3.

The spectrum of a train of unipolar pulses amplitude-modulated by a single channel is shown in Fig. 4(b). This spectrum has been separated from those of the other channels (which occupy the same frequency bands) by the gating operation. If the highest frequency $F_m$ of the channel signal is less

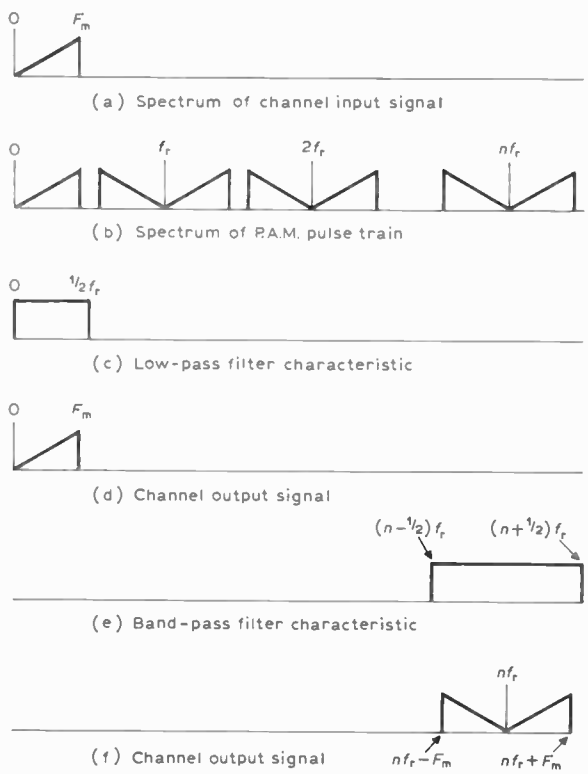


Fig. 4. Conversion from unipolar p.a.m. to simple double-sideband amplitude modulation by a band-pass filter.

than half the p.r.f., $f_r$, the sidebands do not overlap. It is therefore possible, by means of a low-pass filter having a cut-off frequency $\frac{1}{2}f_r$ to extract the original signal (plus d.c. component) from the p.a.m. waveform, as shown in Fig. 4(d). This demodulation method is used in the t.d.m. system shown in Fig. 2.

By using a band-pass filter instead of a low-pass filter, it is possible to extract one of the harmonics of $f_r$ together with its sidebands, as shown in Fig. 4(f). If the pass-band of the filter extends from $(n-\frac{1}{2})f_r$ to $(n+\frac{1}{2})f_r$, its output signal $v_6$ contains only those components within this frequency range. Thus, from eqn. (8),

$$v_6 = B_n\{2\cos n\omega_r t + m\cos[(n\omega_r+\omega_m)t+\phi] + m\cos[(n\omega_r-\omega_m)t-\phi]\}$$
$$= v_1 . 2B_n/A \qquad \text{.....(11)}$$

where $\omega_c = n\omega_r$.

The output is thus an amplitude-modulated carrier wave of frequency $n\omega_r/2\pi$ (c.f. eqn. (3)).

If a band-pass filter is provided for every channel, each selecting a different pair of sidebands, the output terminals of these filters can be connected to a common path[10] as shown in Fig. 3. The signals of all the channels are thus frequency-division multiplexed and can be transmitted over a line or radio link. This method provides both sidebands and does not suppress the carrier. Its f.d.m. signal is therefore suitable for carrier terminal equipments designed for double-sideband transmission.[2,4] To ensure compatibility, the p.r.f. of the t.d.m. system must be chosen so that its harmonics coincide with the carrier frequencies used in the f.d.m. system. Transmission of the carrier can provide a facility for signalling. A d.c. signal at the input of the t.d.m. channel modulator can determine whether it produces output pulses. Presence or absence of these pulses determines whether the band-pass filter produces a carrier. Presence or absence of this carrier can, in turn, determine whether the f.d.m. channel demodulator produces a d.c. output signal.

If the t.d.m. system uses bipolar pulses, the spectrum of its signal (from eqn. (10)) is shown in Fig. 5(b). If this signal is passed through a filter with a pass band from $(n-\frac{1}{2})\omega_r$ to $(n+\frac{1}{2})\omega_r$, the output signal is

$$v_7 = mB_n\{\cos[(n\omega_r+\omega_m)t+\phi] + \cos[(n\omega_r-\omega_m)t-\phi]\}$$
$$= v_2 . 2B_n/A. \qquad \text{.....(12)}$$

The output thus provides a double-sideband suppressed-carrier signal (c.f. eqn. (4)).

If the filter pass band is from $(n-\frac{1}{2})\omega_r$ to $n\omega_r$ the output signal is

$$v_8 = mB_n\cos[(n\omega_r-\omega_m)t-\phi]$$
$$= v_L . 2B_n/A \qquad \text{.....(13)}$$

and if the filter pass band is from $\omega_r$ to $(n+\frac{1}{2})\omega_r$, the

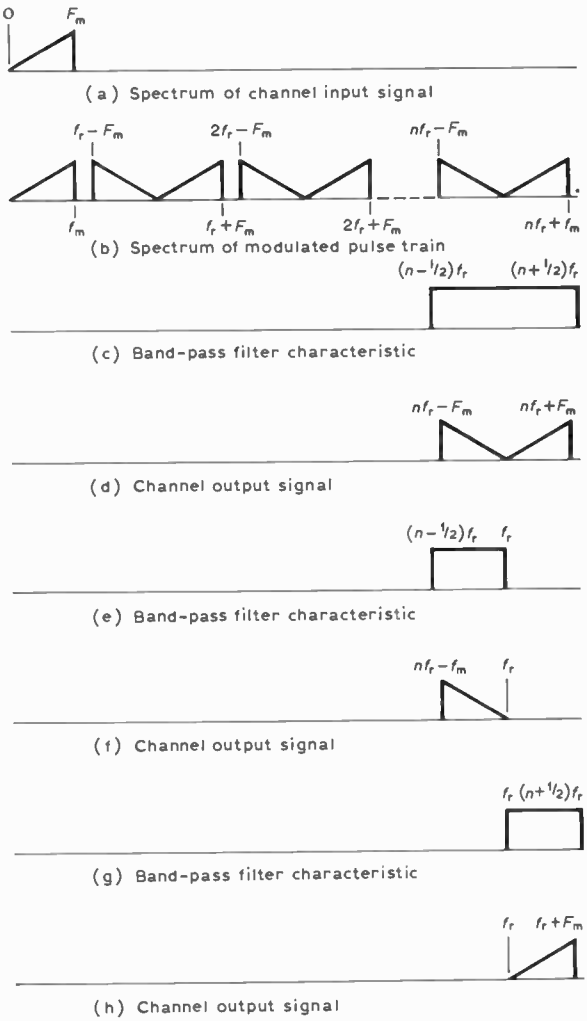


**Fig. 5.** Conversion from bipolar p.a.m. to suppressed-carrier amplitude modulation by a band-pass filter.

output signal is

$$v_9 = mB_n\cos[(n\omega_r+\omega_m)t+\phi]$$
$$= v_U . 2B_n/A. \qquad \text{.....(14)}$$

The output is thus a single-sideband signal (s.s.b.) (c.f. eqn. (5)). If a band-pass filter is provided for every channel and the output terminals are connected to a common path as shown in Fig. 3, the signals are frequency-division multiplexed. This f.d.m. signal can be sent over a line or radio link and be received by conventional s.s.b. carrier terminal equipment. To ensure compatibility, the p.r.f. of the t.d.m. system must be chosen so that its harmonics coincide with carrier frequencies used in the carrier terminal equipment. However, f.d.m. equipment using s.s.b. modulation normally uses a separation $F_m$ between adjacent carrier frequencies.† The method described

† The C.C.I.T.T. basic twelve-channel group consists of lower sidebands of virtual carriers spaced at 4 kHz intervals between 64 kHz and 108 kHz.

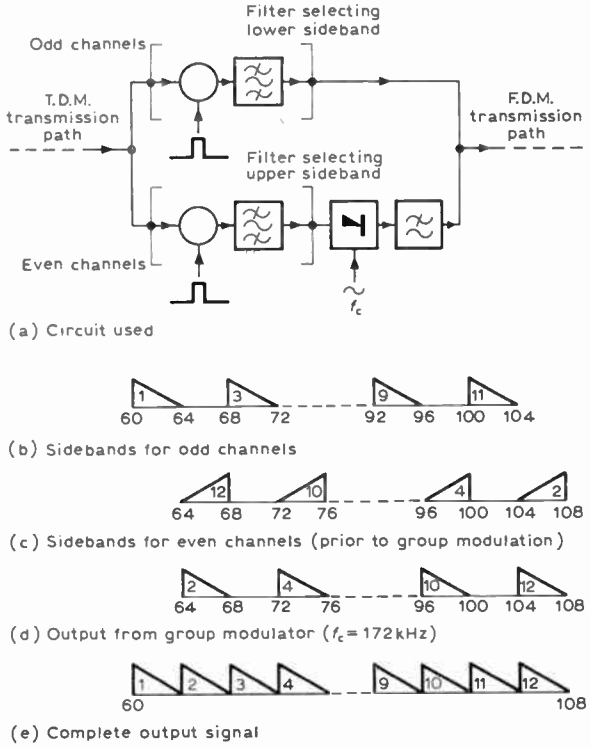


**Fig. 6.** Use of group modulation in converting bipolar t.d.m. to single-sideband f.d.m.

above results in a separation of $f_r = 2F_m$, thus utilizing only half the available bandwidth of the transmission path. This difficulty can be overcome as shown in Fig. 6. A group of filters selects lower sidebands for one-half of the channels and another group of filters selects upper sidebands for the other channels. Filters in the first group are connected directly to the transmission path and those in the second group are connected to it through a group modulator.

The method of conversion from t.d.m. to f.d.m. shown in Fig. 3 uses only a gate and a band-pass filter per channel: the method shown in Fig. 2 requires a gate, an amplifier, a modulator, a low-pass filter and a band-pass filter for each channel. Amplification is still necessary in the method of Fig. 3, but it can be provided by a common amplifier in the f.d.m. path; the method of Fig. 2 needs an individual amplifier for each channel in order to obtain an adequate signal level at the modulator input.

## 5. F.D.M. to T.D.M. Conversion

The modulated signal of a single channel may be extracted from the complete signal of an f.d.m. system by means of a band-pass filter, as shown in Fig. 7. This signal may then be gated by a train of pulses used for the corresponding channel in a t.d.m. system.

If the carrier wave given by eqn. (1) is sampled by gating it with the pulse train given by eqn. (6) the output is

$$v_{10} = v_c \cdot v_3$$
$$= AB_0 \cos \omega_c t + 2A \sum_{n=1}^{\infty} B_n \cos n\omega_r t \cos \omega_c t \quad (15)$$

If the carrier frequency is chosen to be an integral multiple, $q$, of the sampling frequency, we can write

$$v_{10} = AB_0 \cos \omega_c t + A \sum_{n=1}^{\infty} B_n[(\cos (q+n)\omega_r t + \cos (q-n)\omega_r t]$$
$$= A \sum_{x=-\infty}^{\infty} B_{x-q} \cos x\omega_r t \quad \ldots\ldots(16)$$

where $B_{-n} = B_n$ and $x = q+n$.

Provided that the sampling pulses are sufficiently short compared with the period of the carrier wave, it is possible to write

$$B_{x-q} = B_x = B_{-x} = B_{-x-q} \quad \ldots\ldots(17)$$
$$v_{10} = A \sum_{x=-\infty}^{\infty} B_x \cos x\omega_r t$$
$$= AB_0 + 2A \sum_{x=1}^{\infty} B_x \cos x\omega_r t$$
$$= Av_3. \quad \ldots\ldots(18)$$

Thus, if the gate is periodically opened by a train of short sampling pulses which coincide with the peaks of the carrier wave, the output is a train of unipolar pulses (c.f. eqn. (6)). On a basis of common sense, this result would be expected.

If an upper-sideband signal, given by eqn. (5b), is gated by the pulse train given by eqn. (6), the output is

$$v_{11} = v_U \cdot v_3$$
$$= \tfrac{1}{2}mA \cos [(\omega_c + \omega_m)t + \phi] \times \times \left\{B_0 + 2 \sum_{n=1}^{\infty} \cos n\omega_r t\right\}$$

If $\omega_c = q\omega_r$, then

$$v_{11} = \tfrac{1}{2}mAB_0 \cos [(q\omega_r + \omega_m)t + \phi] + \tfrac{1}{2}mA \sum_{n=1}^{\infty} B_n \cos \{[(q+n)\omega_r + \omega_m]t + \phi\} + \tfrac{1}{2}mA \sum_{n=1}^{\infty} B_n \cos \{[(q-n)\omega_r + \omega_m]t + \phi\}$$
$$= \tfrac{1}{2}mA \sum_{x=-\infty}^{\infty} B_{x-q} \cos [(x\omega_r + \omega_m)t + \phi]$$

where $B_{-n} = B_n$ and $x = q+n$.

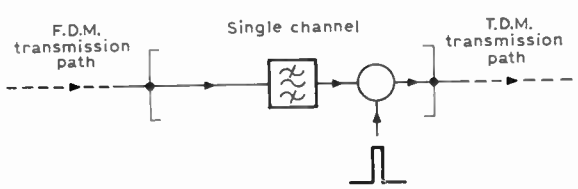


**Fig. 7.** Circuit for conversion from f.d.m. to t.d.m.

Provided that the sampling pulses are sufficiently short compared with the period of the carrier wave, eqn. (17) is satisfied and

$$v_{11} = \tfrac{1}{2}mA \sum_{x=-\infty}^{\infty} B_x \cos[(x\omega_r + \omega_m)t + \phi]$$

$$= \tfrac{1}{2}mA\Big\{B_0 \cos(\omega_m t + \phi) + \sum_{x=1}^{\infty} B_x \cos[(x\omega_r + \omega_m)t + \phi] + \sum_{x=1}^{\infty} B_x \cos[(x\omega_r - \omega_m)t - \phi]\Big\}$$

$$= \tfrac{1}{2}Av_5. \qquad \text{.....(19)}$$

The output is thus a train of bipolar amplitude-modulated pulses, as given by eqn. (10).

If a lower-sideband signal given by eqn. 5(a) is sampled by the pulse train given by eqn. (6), the output is

$$v_{12} = v_L . v_3$$

and, similarly, it can be shown that

$$v_{12} = \tfrac{1}{2}Av_5. \qquad \text{.....(20)}$$

For a double-sideband suppressed-carrier signal, the output from the gate is

$$\begin{aligned} v_{13} &= v_2 . v_3 \\ &= v_3(v_U + v_L) \\ &= v_{11} + v_{12} \\ &= Av_5 \end{aligned} \qquad \text{.....(21)}$$

Thus, if the input to the sampling gate is either a single-sideband or a double-sideband suppressed-carrier signal, the output is an amplitude-modulated bipolar train (c.f. eqn. (10)).

If the simple double-sideband amplitude-modulated signal given by eqn. (3) is sampled by the pulse train given by eqn. (6), the output is

$$\begin{aligned} v_{14} &= v_1 v_3 \\ &= v_3(v_c + v_2) \quad \text{(from eqns. (3) and (4))} \\ &= v_{10} + v_{13} \\ &= A(v_3 + v_5) \quad \text{(from eqns. (18) and (21))} \end{aligned}$$

Thus, from eqns. (6) and (10):

$$v_{14} = AB_0[1 + m\cos(\omega_m t + \phi] + 2\sum_{n=1}^{\infty} AB_n \cos n\omega_r t + mA\sum_{n=1}^{\infty} B_n\{\cos[(n\omega_r + \omega_m)t + \phi] + \cos[(n\omega_r - \omega_m)t - \phi)]\} \qquad \text{.....(22)}$$

$$= Av_4 \quad \text{(from eqn. (8))}$$

Thus, if the amplitude-modulated carrier shown in Fig. 8(a) is passed through a gate that is periodically opened by a train of short sampling pulses which coincide with the peaks of the carrier wave, the output is an amplitude-modulated unipolar pulse train, as shown in Fig. 8(c).

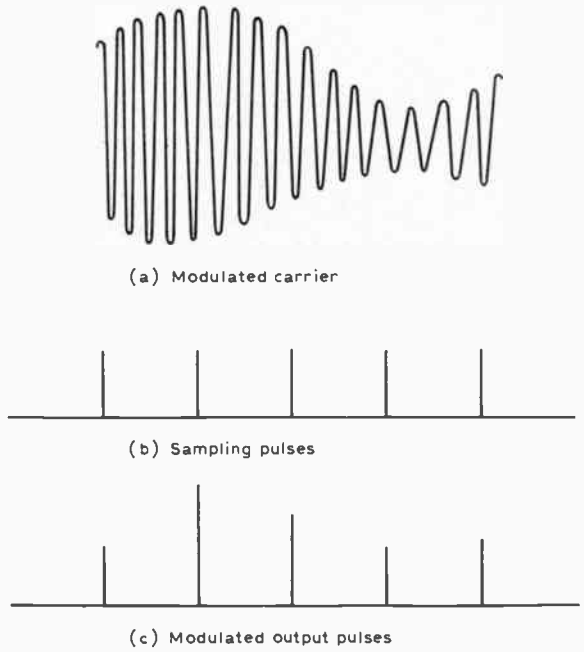


**Fig. 8.** Conversion of double-sideband amplitude-modulated carrier to unipolar amplitude-modulated pulse train.

It is therefore possible to convert from f.d.m. to t.d.m. by the method shown in Fig. 7. The channels on the common f.d.m. transmission path are separated by band-pass filters, the outputs of the filters are sampled by pulses occurring at different times in the t.d.m. cycle and the outputs of the gates are connected to the common t.d.m. transmission path.

In order to enable any f.d.m. channel to be connected to any t.d.m. channel, all the sinusoidal carriers must have peaks occurring at every sampling time in the t.d.m. period. Thus, for an $n$-channel system with a p.r.f. of $f_r$, the lowest carrier frequency used is $nf_r$ and the highest is thus $2nf_r$. If completely flexible interconnexion of the channels is not required, the carrier frequencies can be lower. The lowest possible carrier frequencies would be zero to $nf_r$. However, it may be desirable to use low frequencies for transmission over the f.d.m. link in order to minimize line attenuation and yet to retain full flexibility of interconnexion. This can be achieved by introducing a stage of group modulation. Thus, the $n$ channels may be transmitted in the range 0 to $(n+\frac{1}{2})f_r$ and then modulated with a carrier $nf_r$. The upper sideband occupies the range $nf_r$ to $(2n+\frac{1}{2})f_r$ and each channel, after separation by a band-pass filter, can then be gated to modulate any pulse in the t.d.m. cycle.

## 6. Discussion of Conversion by Sampling and Filtering

Direct demodulation of a t.d.m. pulse train by means of a simple low-pass filter produces an output in which the d.c. and audio-frequency components are proportional to the length of the pulses as well as to their amplitudes. It is therefore necessary to control pulse length very accurately if transmission levels are to remain stable with time. Moreover, if the t.d.m. system has many channels, the pulse length is short and the output level is low. The channel demodulator must therefore contain a high-gain amplifier. This amplifier must have a low noise level and a gain that is stable with time if the system is to be useful.

The method of t.d.m. to f.d.m. conversion described in Section 4 shares the defects of the simple demodulator. The amplitude of the output from each band-pass filter is proportional to the length of its input pulse as well as its height, and a high-gain amplifier is required.

A recent development in pulse transmission is the introduction of the principle of resonant-transfer.[11,12,13] This provides an alternative to voltage sampling followed by either low-pass filtering or pulse lengthening[1] as a means of t.d.m. demodulation. The extension of this principle to t.d.m./f.d.m. conversion has been proposed by M. Schlichte[14] and P. M. Thrasher[15] and has been analysed by Fettweis.[16] It will be considered in the next section. An experimental model of an integrated system using resonant transfer to interconnect a t.d.m. switching system with a double-sideband f.d.m. transmission system has been constructed by Dahlman, Roehr, Thrasher and Ward.[17]

## 7. Resonant-transfer using Low-pass Circuits

A simple t.d.m. system using the principle of resonant-transfer is shown in Fig. 9. Both the transmitter and the receiver of each channel contain an energy-storage network in the form of a low-pass filter. The end capacitor of each filter is connected to the common path through an inductor and a switch.

The circuit is designed so that the ends of the two filters at which resonant-transfer takes place are normally terminated by an open-circuit. It is a matter of good practical design to ensure that neither of the two inductors $L_1, L_2$ in Fig. 9 is shunted by a capacitor. This ensures that the capacitance which takes part in the resonant-transfer process is well defined.

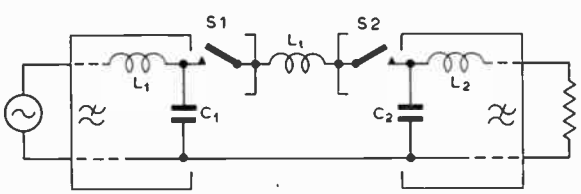


**Fig. 9.** T.d.m. system using resonant transfer between low-pass filters.

During the interval between switch closures, the capacitor ($C_1$) of the transmitting filter is slowly charged, until the moment when the switches S1 and S2 are simultaneously closed.

Provided that the inductors $L_1$ and $L_2$ satisfy the inequality

$$L_1, L_2 \gg L_t \qquad \text{.....(23)}$$

the inductors $L_1$ and $L_2$ are effectively open-circuit during the time for which the switches are closed.

Closure of the switches thus completes an oscillatory circuit consisting of $L_t$, $C_1$ and $C_2$. If $C_1 = C_2$ and the duration of the switch closure, $t_0$, is given by

$$t_0 = \pi\sqrt{\tfrac{1}{2}C_1 L_t} \qquad \text{.....(24)}$$

the capacitor $C_1$ completely discharges and its charge is transferred to $C_2$. Thus, when the switches open the p.d. across $C_2$ is equal to the p.d. which was formerly across $C_1$. Capacitor $C_2$ then discharges slowly through its low-pass filter during the interval when the switches are open.

Since the voltages at the transmitter and receiver are equal, the input and output powers are equal. Thus lossless t.d.m. transmission is theoretically possible.

In practice, a small loss occurs due to the finite resistance of the diodes or transistors used as the switches. The use of resonant transfer obviates the need for the high-gain low-noise amplifier at the t.d.m. demodulator shown in Fig. 2. The pulse length must still be closely controlled, however, to satisfy eqn. (24).

The circuit of Fig. 9 consists of reciprocal circuit elements: consequently the source and load may be interchanged. Thus the transmitter and receiver can act as 'bothway' gates providing bidirectional transmission over a two-wire common path. For four-wire transmission, separate paths in the two directions can, of course, always be provided. Alternatively, a time-division hybrid[18] arrangement may be used to connect two-wire individual channels to a common point at each end of a four-wire transmission path.

## 8. Resonant Transfer using Band-pass Circuits

During the resonant-transfer process described above, the only portions of the low-pass filters which play any part are the end shunt capacitors $C_1$ and $C_2$. Because the rest of the filters do not take part in the resonant-transfer, they can be of any form, provided that they act as high impedances across $C_1$ and $C_2$ respectively, during the pulse. Thus, if it satisfies

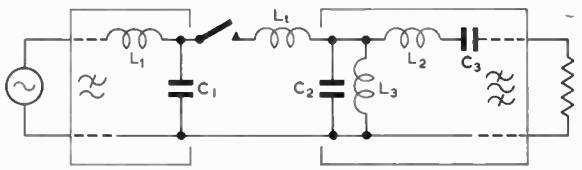


Fig. 10. Resonant transfer between a low-pass filter and a band-pass filter.

this condition, a band-pass filter may be substituted for one of the low-pass filters.

The right-hand filter of Fig. 9 may be transformed from a low-pass filter into a band-pass filter by replacing each inductor by a series resonant circuit, and each capacitor by a parallel resonant circuit. The resonant frequency of these circuits is chosen to be the mid-band frequency of the filter, $f_b$. This will produce the type of circuit which is shown in Fig. 10.

As far as the resonant-transfer process is concerned, this new circuit may be made indistinguishable from that of Fig. 9. This will happen if the impedances presented by the series and parallel $LC$ combinations to the components of the resonant-transfer current remain indistinguishable from those which would be presented by the original inductors and capacitors during the time of the switch closure. For the component at frequency $\omega_0/2\pi$ (where $\omega_0 = \pi/t_0$) the parallel circuit $L_3C_2$ has impedance

$$1/j(\omega_0 C_2 - 1/\omega_0 L_3)$$

whereas capacitor $C_2$ in the original low-pass circuit has impedance $1/j\omega_0 C_2$. It is therefore necessary that

$$\omega_0^2 C_2 L_3 \gg 1$$

But

$$C_2 L_3 = 1/\omega_b^2$$

Therefore

$$\omega_0 \gg \omega_b$$

The necessary condition for resonant transfer to take place as before is thus

$$t_0 \ll 1/f_b \qquad \text{.....(25)}$$

where $t_0$ is the duration of switch closure and $f_b$ is the mid-band frequency of the band-pass filter.

A similar argument shows that condition (25) also ensures that the series circuit $L_2C_3$ presents an impedance similar to that of inductor $L_2$ of the original low-pass circuit during resonant transfer. Thus, if condition (25) is satisfied, resonant transfer between a low-pass filter and a band-pass filter takes place in exactly the same way as between two low-pass filters. The only difference is in the frequency components selected by the filter for application to its load. Resonant-transfer gating can therefore be used for t.d.m./f.d.m. conversion and f.d.m./t.d.m. conversion by the methods described in Sections 4 and 5.

## 9. Experimental Work

In order to demonstrate conversion between t.d.m. and single-sideband f.d.m., two filters were designed, the pass-bands being 0–4 kHz and 12–16 kHz. A variety of Thomas filter[19] was used which had an $mm'$-derived termination[20] in place of the $m = 0{\cdot}6$ derived terminating half-section originally proposed by Thomas.

The Thomas method of filter synthesis produces a ladder network of reactive circuit elements terminated by a resistor, which approximates the impedance of an ideal filter at the normally open-circuit end. It was therefore necessary to use a filter analysis program to predict the variation of insertion loss with frequency.[21,22] The low-pass filter was built and the experimental performance of the filter *as such* was found to be in good agreement with the prediction.

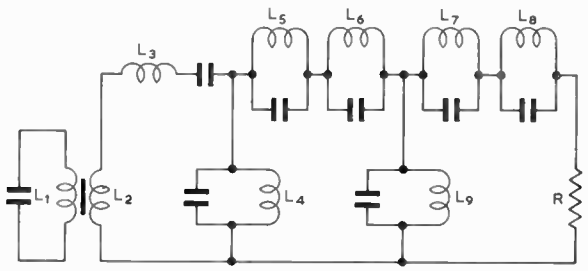


Fig. 11. Band-pass filter used in experimental work.

| Component | Value | Component | Value |
|---|---|---|---|
| L1 | 12·7 mH | L6 | 0·38 mH |
| L2 | 1·27 mH | L7 | 1·52 mH |
| L3 | 45·9 mH | L8 | 1·00 mH |
| L4 | 1·56 mH | L9 | 2·77 mH |
| L5 | 0·51 mH | R | 600 ohms |

The capacitors were adjusted to resonate with the inductors at the mid-band frequency of the filter (14 kHz).

The band-pass filter was formed by band-pass transformation of the low-pass filter. The circuit of this filter is shown in Fig. 11. This is an inherently poor method of making a band-pass filter, because an inductor in series with a capacitor must appear in at least one branch of any Thomas filter subjected to band-pass transformation. This gave rise to difficulties associated with the stray capacitance across that inductor. These difficulties were overcome by the use of a transformer to lower the impedance level of the filter. This is not good practice, but did allow the resonant transfer circuit to have a reasonably well-defined capacitance at the normally open-circuit end of the band-pass filter during the resonant transfer. Although the performance of the band-pass filter was poor when judged by the strict standards required for a channel filter in an f.d.m. system, it was adequate for the purpose of the experiment.

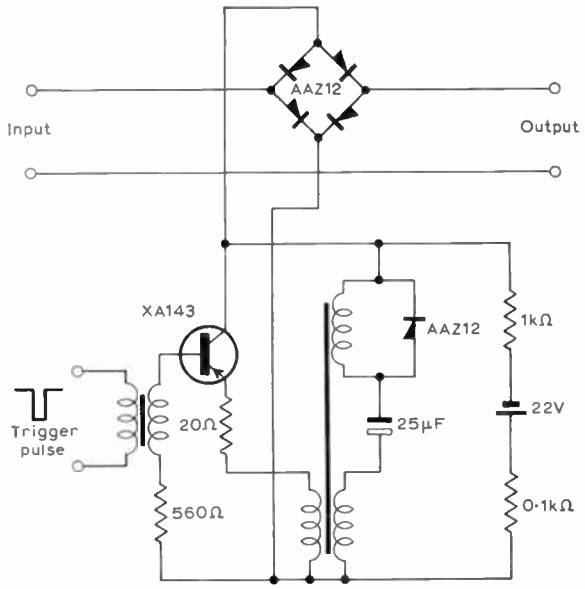


Fig. 12. Four-diode switch used as gate circuit for resonant transfer.

The filters were connected by a gate opened by pulses of approximate length 2 μs with a p.r.f. of 12 kHz. This gate consisted of a four-diode switch controlled by a blocking oscillator, as described by Perkins.[23] This circuit is shown in Fig. 12.

When a direct voltage was applied to the low-pass filter, the oscillograms shown in Fig. 13 were obtained. The lower waveform (Fig. 13(a)) illustrates the slow charging process followed by a rapid discharge which takes place at the output terminals of the low-pass filter. The upper waveform (Fig. 13(b)) demonstrates the shock excitation due to the transferred charge at the input terminals of the band-pass filter.

The oscillogram in Fig. 14 shows an input to the low-pass filter at 2 kHz causing an output at 14 kHz to appear at the load resistor of the band-pass filter. The reverse process, whereby an input at 14 kHz to the band-pass filter causes a signal at 2 kHz to occur at the load resistor of the low-pass filter, is shown in Fig. 15. The input and output amplitudes in Fig. 15 are practically the same, whereas they differ by nearly a factor of ten in Fig. 14. This is due to the presence of the transformer, which has a 10 : 1 impedance ratio. The overall conversion loss was measured and was found to be approximately 4 dB for both transmission directions.

The above experiment thus demonstrated the conversion of an audio-frequency signal to a modulated pulse train and then to a single-sideband signal, and the carrying out of the reverse process. Conversion between a modulated pulse train and a double-

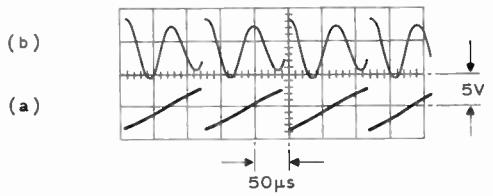


Fig. 13. Oscillogram of resonant transfer with d.c. input to low-pass filter.
(a) p.d. across output capacitor of low-pass filter.
(b) p.d. across input capacitor of band-pass filter.

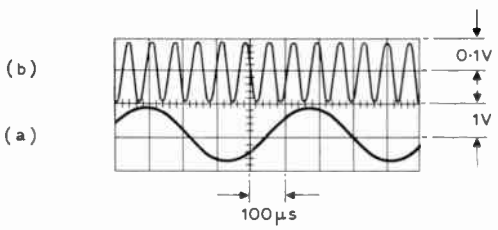


Fig. 14. Oscillogram of resonant transfer with a.c. input to low-pass filter.
(a) 2 kHz input to low-pass filter.
(b) 14 kHz output from band-pass filter.

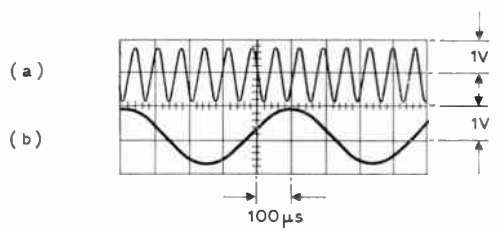


Fig. 15. Oscillogram of resonant transfer with a.c. input to band-pass filter.
(a) 14 kHz input to band-pass filter.
(b) 2 kHz output from low-pass filter.

sideband amplitude-modulated signal has been demonstrated by Dahlman, Roehr, Thrasher and Ward.[17]

## 10. Conclusions

F.d.m. and t.d.m. systems using amplitude modulation can be interconnected without demodulating individual channels to audio-frequencies. It is, however, necessary for the carrier frequencies of the f.d.m. system to be harmonics of the p.r.f. of the t.d.m. system and for these supplies to be synchronized.

Unipolar t.d.m. signals can be converted to simple double-sideband amplitude-modulated f.d.m. signals by gating them into a bank of band-pass filters, each centred on a harmonic of the p.r.f. The outputs of these filters are connected to a common path to transmit the f.d.m. signals. Simple double-sideband amplitude-modulated f.d.m. signals can be converted

to unipolar t.d.m. by separating the channels with band-pass filters and sampling the output of each filter with a pulse occupying a different position in the t.d.m. cycle. The sampled outputs are connected to a common path to transmit the t.d.m. signal.

Similar arrangements of gates and filters can be used to interconnect a t.d.m. system using bipolar pulse modulation with an f.d.m. system using suppressed-carrier double-sideband or single-sideband modulation.

It has been shown that resonant transfer can be used to reduce energy losses in the conversion processes and so eliminate amplifiers. However, it is necessary for the pulse length to be small compared with the reciprocal of the channel carrier frequency. This may be difficult to achieve with a multi-channel system and further analysis is required to determine the effect of a finite pulse length.

## 11. Acknowledgments

Acknowledgment is made to Associated Electrical Industries Limited for permission to use information contained in this paper. The authors are indebted to Mr. R. F. Hoskins and Dr. W. Saraga for helpful discussions and wish to thank Mr. F. Quelon for assistance in the experimental work.

## 12. References

1. Flood, J. E., 'Time-division multiplex transmission systems *Electronic Engng*, **25**, pp. 2, 58, 101 and 181, 1952.
2. Carruthers, R. S., 'The type N-1 carrier telephone system', *Bell Syst. Tech. J.*, **30**, p. 1, January 1951.
3. Endersby, J. C., Heal, A. W. and Vines, J. C., '12-circuit carrier on deloaded audio cable', I.E.E. Conference on Transmission Aspects of Communication Networks, 1964, p. 52.
4. Chapman, D. and Smith, E. J. E., 'An experimental local area f.d.m. system', ibid, p. 56.
5. Davis, C. G., 'An experimental pulse code modulation. system for short-haul trunks', *Bell Syst. Tech. J.*, **41**, p. 1, 1962.
6. Jessop, A. and Cattermole, K. W., 'A 23-channel p.c.m. telephone transmission system', I.E.E. Conference on Transmission Aspects of Communication Networks, 1964, p. 160.
7. Purton, R. F. and Moffett, R. H., 'A 24-channel p.c.m. junction system', ibid., p. 164.
8. Vaughan, H. E., 'Research model for time-separation integrated communication', *Bell Syst. Tech. J.*, **38**, p. 909, 1959.
9. Walker, E. and Duerdoth, W. T., 'Trunking and traffic principles of a p.c.m. telephone exchange', *Proc. Instn Elect. Engrs.* **111**, p. 1976, 1964.
10. Thomas, E. R., British Patent No. 905,838.
11. Haard, H. B. and Svala, C. G., U.S. Patent No. 2718621, 1953.
12. Cattermole, K. W., 'Efficiency and reciprocity in pulse amplitude modulation', *Proc. I.E.E.*, **105B**, p. 449, 1958.
13. French, J. A. T. and Harding, D. J., 'An efficient electronic switch—the bothway gate', *Post Office Elect. Engrs J.*, **52**, p. 37, 1959.
14. Schlichte, M., British Patent No. 941,769. (Original application made in Germany on 8th March, 1960).
15. Thrasher, P. M., 'A unique technique for frequency division multiplexing and the integration of this method with time division switching', 10th National Communications Symposium (I.E.E.E.), Uttica, N.Y., 1964, p. 41.
16. Fettweis, A., 'Théorie des Circuits à Transfert Resonnant', Dissertation for the degree of Doctor of Applied Science at the Catholic University of Louvain, Belgium, 1963.
17. Dahlman, P. O., Roehr, K. M., Thrasher, P. M. and Ward, R. J., 'Integrated Switching and Multiplexing', Report No. RADC–TRD–64–329, Rome Air Development Center, U.S.A., 1964.
18. Flood, J. E. and Parks, G. H., British Patent No. 842,481.
19. Thomas, G. B., 'Synthesis of input and output networks for a resonant-transfer gate', *I.R.E. Internat. Conv. Rec.*, **9**, Part 4, (Circuit Theory), March 1961.
20. Zobel, O. J., 'Extensions to the theory and design of electric wave filters', *Bell Syst. Tech. J.*, **10**, p. 284, April 1931.
21. Saraga, W., 'Some applications of a digital computer programme for filter response curves', *A.E.I. Engineering*, Supplement, October 1963.
22. Johnson, M. H., 'Some aspects of loss-frequency computation for filter networks', ibid.
23. Perkins, J. C., 'Transmission aspects of an electronic switchboard employing time-division multiplexing', *Trans. Amer. Inst. Elect. Engrs*, **78**, Part I, p. 949, January 1960.
24. Thrasher, P. M., 'A new method of frequency-division multiplexing and its integration with time-division switching', *I.B.M. J. Res. Development*, **9**, p. 137, March 1965.

*Manuscript first received by the Institution on 5th January 1969 and in revised form on 30th July 1969. (Paper No. 1300/Com. 26)*

U.D.C. 621.374.3:681.325.55

# Design for a Multi-Input Binary Adder

*By*

**D. W. LEWIN,**
M.Sc., A.Inst.P., C.Eng., M.I.E.R.E.†

The need often arises in digital systems for a fast multi-input adder capable of adding together $n$ distinct serial binary numbers. The normal design method is to employ a parallel-series configuration of 2-input synchronous adders. It is shown how the overall speed of a multi-input adder may be enhanced using a 3-input adder stage. A circuit is described using cascaded 2- and 3-input synchronous adders, which may be clocked at 100 ns allowing the addition of six 10-bit binary numbers in 1$\mu$s.

## 1. Introduction

In many special purpose digital system applications, for example the design of digital filters, the need often arises for the fast multiple addition of $n$ distinct binary numbers. The conventional techniques using repeated addition tend to be either too slow, if performed serially, or too costly if parallel methods are used. One solution to the problem is to use iterative techniques based on the simple two-input serial adder circuit, shown in Fig. 1. This approach has been discussed by Hennie[1] who suggested a simple cascaded system, shown in Fig. 2(a) for six inputs ABCDEF. In this circuit the inputs AB are taken to the first adder, and then the sum output of this stage, together with input C, taken to the second adder stage, and so on. Note that each 2-input adder stage is fed with basic timing pulses, i.e. clock pulses.

The operation of the circuit is such that prior to the first clock pulse the combinational logic in the adder stages produces the sum of the least significant digits, i.e. $S = A \oplus B \oplus C \oplus D \oplus E \oplus F$. Similarly the carry-producing logic presents the appropriate input conditions to the terminals of the JK carry bistable of each stage. (Note that $J_c = AB$, $K_c = \bar{A}\bar{B}$ and from the characteristic equation of the bistable we have $C_+ = J\bar{C} + \bar{K}C = AB + AC + BC$, where the suffix + indicates the next output state of the carry bistable C). When the clock pulse arrives the sum digit is shifted into an output register, the carry bistables are set, and the next input digits are entered to the circuit; the operation then proceeds as before.

Using this circuit $n$ binary numbers can be added in one wordtime, that is $N$ clock pulse times (digit-times) where $N$ is the number of bits in the binary word. For this particular circuit the maximum delaying path is through $2(n-1)$ logic levels (the AND–NOR gates in Fig. 1(b) count as one level), thus the clock pulse period ($T$) must not be less than $2\alpha(n-1)$ seconds where $\alpha$ is the average propagation delay per level and $n$ the number of binary inputs. It is interesting to observe that if adder–subtractor units are used (or two's complemented numbers) in the cascaded system, it is possible to add and subtract any combination of numbers. This is a facility which could be useful if digital scaling, or weighting, is required.

On reflection it will be apparent that the multiple addition of binary numbers can often result in a sum containing more than $N$ bits, that is, overflow will occur. For example, the maximum possible sum of six 10-bit positive numbers, represented in two's complement notation, would be 3066, i.e. a 12-bit number. If the full result is required it is necessary to clock the circuit 12 times, with the input at zero for the last two clock pulses, otherwise conventional out-of-range logic circuits must be employed to detect overflow.

The simple cascaded circuit may be restructured, so as to reduce the number of levels in the combinational logic, and hence increase its speed of operation; Fig. 2(b) shows a typical circuit. This circuit may be clocked faster since the delaying path is reduced to six logic levels allowing $T \leqslant 6\alpha$ seconds; furthermore no extra logic is required.

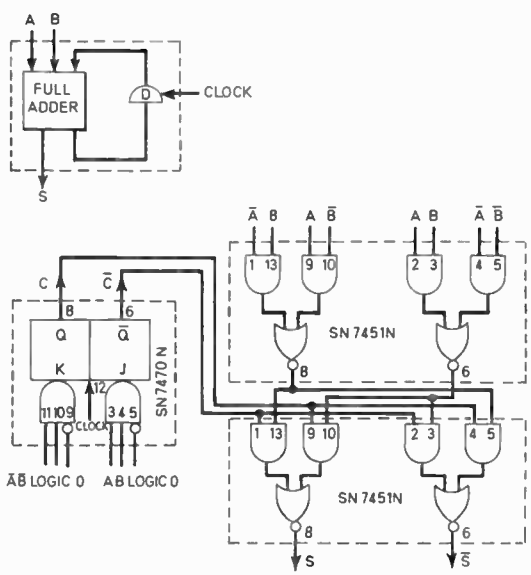


**Fig. 1.** 2-input synchronous adder.

† Department of Electronics, University of Southampton.

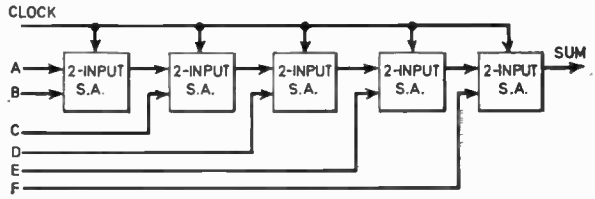


(a)

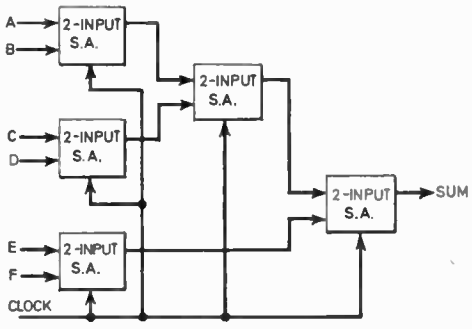


(b)

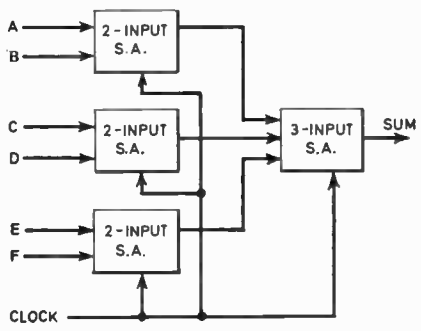


(c)

**Fig. 2.** Iterative serial adder.

However, considerably faster addition times can be achieved if instead of using 2-input adders only, a special 3-input adder is incorporated into the design, (see Fig. 2(c)). The speed of operation of this circuit is increased to $T < 4\alpha$ seconds (delaying path through 4 logic levels), but at the expense of slightly more logic. This approach can obviously be extended to handle any number of inputs, if necessary by designing a 5-input adder etc. The design and implementation of the system shown in Fig. 2(c) will now be considered in detail.

## 2. Two-Input Synchronous Adder

The logic diagram for the 2-input adder used in the system is shown in Fig. 1(b), implemented in Texas TTL circuits. This is a fairly conventional circuit, note however that $A\bar{B}+\bar{A}B$ and $\bar{A}\bar{B}+AB$ are generated independently to avoid an extra invertor level. For the same reasons the sum and $\overline{\text{sum}}$ outputs are generated separately and distributed by a double-rail arrangement to the following units. It has also been assumed that a double-rail system is employed for the binary inputs, and this is feasible since in practice the inputs would normally come from a shift-register. Exclusive-OR gates, comprising AND–NOR logic, have been used in the implementation since as the propagation delay through the AND–NOR configuration is the same as that through a basic NAND/NOR gate, they can be considered as one level of logic. The circuit uses a total of 3 logic packages at an approximate cost of £4.

## 3. Three-Input Synchronous Adder

The state tables for the synchronous 3-input adder are shown in Table 1, and these follow directly from conventional logical design theory.[2]

The first state table (Table 1(a)) shows the transition from a present state of the synchronous circuit to the next-state, and the resulting output (represented as next-state/output) for all input conditions. The major design problem for the 3-input adder is the treatment of carries over more than one stage, i.e. protracted carries. Consider the addition of the three serial numbers A = 0110, B = 1110 and C = 1110, as shown below:

| | | | | | | |
|---|---|---|---|---|---|---|
| clock | 5 | 4 | 3 | 2 | 1 | 0 |
| A | 0 | 0 | 0 | 1 | 1 | 0 |
| B | 0 | 0 | 1 | 1 | 1 | 0 |
| C | 0 | 0 | 1 | 1 | 1 | 0 |
| | 1 | 0 | 0 | 0 | 1 | 0 |

**Table 1.** State tables for 3-input adder

(a)

| Present states | Inputs ABC Next-states and output S | | | | | | | |
|---|---|---|---|---|---|---|---|---|
| | 000 | 001 | 010 | 011 | 100 | 101 | 110 | 111 |
| 1 | 1/0 | 1/1 | 1/1 | 2/0 | 1/1 | 2/0 | 2/0 | 2/1 |
| 2 | 1/1 | 2/0 | 2/0 | 2/1 | 2/0 | 2/1 | 2/1 | 3/0 |
| 3 | 2/0 | 2/1 | 2/1 | 4/0 | 2/1 | 4/0 | 4/0 | 4/1 |
| 4 | 2/0 | 2/1 | 2/1 | 3/0 | 2/1 | 3/0 | 3/0 | 3/1 |

(b)

| $Y_1Y_2$ | Inputs ABC Next-states and output S | | | | | | | |
|---|---|---|---|---|---|---|---|---|
| | 000 | 001 | 010 | 011 | 100 | 101 | 110 | 111 |
| 00 | 00/0 | 00/1 | 00/1 | 01/0 | 00/1 | 01/0 | 01/0 | 01/1 |
| 01 | 00/1 | 01/0 | 01/0 | 01/1 | 01/0 | 01/1 | 01/1 | 10/0 |
| 10 | 01/0 | 01/1 | 01/1 | 11/0 | 01/1 | 11/0 | 11/0 | 11/1 |
| 11 | 01/0 | 01/1 | 01/1 | 10/0 | 01/1 | 10/0 | 10/0 | 10/1 |

Note that there is a protracted carry produced in column 2 which must be added to the next but one

digit position. As a consequence of this, the circuit effectively requires two carry bistables, i.e. a four-state machine. From Table 1(a), if the machine is in present state 1 with input $A_0B_0C_0$, the circuit state is unchanged, i.e. this is the starting condition. The input condition $A_1B_1C_1$ in the next clock pulse causes a transition to state 2 (to indicate a single carry) and outputs a 1. A further input of $A_2B_2C_2$ sends the circuit to state 3 (indicating a protracted carry) and outputs a 0. In state 3 an input of $\bar{A}_3B_3C_3$ causes a transition to state 4 (carry plus protracted carry) and outputs 0. The next input will be all zeros (clock pulse 4) sending the circuit to state 2 (single carry) and outputs 0. The final input in clock pulse 5, again all zeros, returns the circuit to state 1 and outputs a 1. Note that the circuit overflows, since the number range is exceeded, and two additional clock pulses are required to obtain the final number. A similar analysis may be performed for input sequences of any length.

The state table has been assigned (i.e. each machine state has been allocated a unique binary code) using two internal state-variables $Y_1Y_2$ by the next-state technique[3] (Table 1(b)). Input conditions for JK bistables are then extracted and plotted on K-maps (Table 2). The input terms are obtained by comparing the present-state (Y) and next-state ($Y_+$) columns for $Y_1Y_2$ looking for the conditions:

| | | |
|---|---|---|
| J = 1 | when Y = 0 | $Y_+ = 1$ |
| J = 0 | when Y = 0 | $Y_+ = 0$ |
| J don't-care | when Y = 1 | $Y_+ = 0$ |
| | Y = 1 | $Y_+ = 1$ |
| K = 1 | when Y = 1 | $Y_+ = 0$ |
| K = 0 | when Y = 1 | $Y_+ = 1$ |
| K don't-care | when Y = 0 | $Y_+ = 1$ |
| | Y = 0 | $Y_+ = 0$ |

For example, from Table 1(b), we have for the internal state variable $Y_1$ (considering the J input condition) transitions from present-state value 0 to next-state value 1, for the present state and input conditions $\bar{Y}_1Y_2ABC$. Similarly for the K condition for transitions from present value 1 to next value 0 we have:

$$Y_1\bar{Y}_2\bar{A}\bar{B}\bar{C}+Y_1\bar{Y}_2\bar{A}B\bar{C}+Y_1\bar{Y}_2\bar{A}BC+$$
$$+Y_1\bar{Y}_2A\bar{B}\bar{C}+Y_1Y_2\bar{A}\bar{B}\bar{C}+Y_1Y_2\bar{A}BC+$$
$$+Y_1Y_2\bar{A}B\bar{C}+Y_1Y_2AB\bar{C}.$$

These are shown plotted on K-maps, together with the 'don't-care' terms in Table 2.

The minimized bistable input equations from the K-maps are as follows:

$$J_{Y_1} = ABCY_2$$
$$J_{Y_2} = Y_1+AB+AC+BC$$
$$K_{Y_1} = \bar{A}\bar{B}+\bar{A}\bar{C}+\bar{B}\bar{C}$$
$$K_{Y_2} = ABY_1+ABC+BCY_1+ACY_1+\bar{A}\bar{B}\bar{C}\bar{Y}_1$$

and the sum equations are given by:

**Table 2.** K-maps for 3-input adder

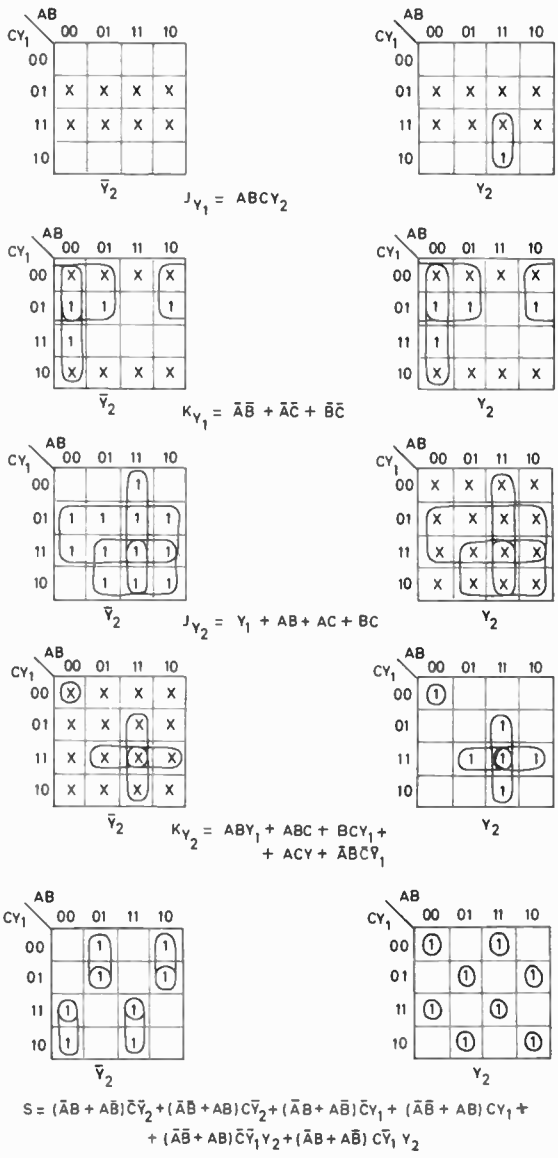


$$S = (\bar{A}B+A\bar{B})(\bar{C}Y_1+\bar{C}\bar{Y}_2+C\bar{Y}_1Y_2)+$$
$$+(AB+\bar{A}\bar{B})(CY_1+C\bar{Y}_2+\bar{C}\bar{Y}_1Y_2).$$

These logic equations are shown implemented in Texas TTL circuits in Fig. 3, where L0 and L1 are logic levels 0 and 1 respectively; as before AND/NOR gates have been used whenever possible. The circuit requires ten logic packages at a total cost of £12.

## 4. Multi-Input Adder

Using the logic circuits for the 2- and 3-input adders as described above, the system shown in Fig. 2(c) was implemented and simulated on a Marconi *Myriad II* computer. The simulation was performed using

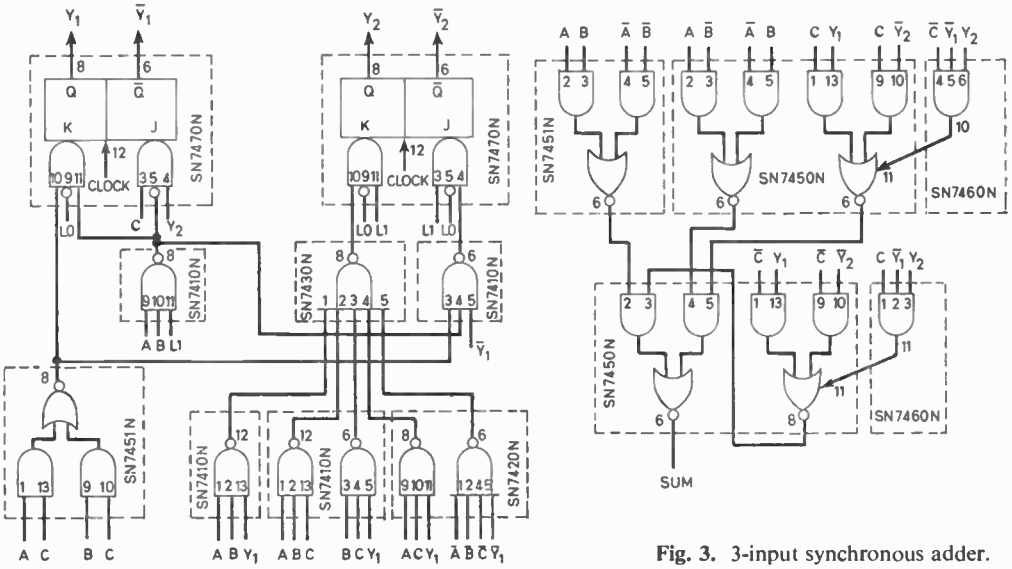


Fig. 3. 3-input synchronous adder.

**Table 3.** Propagation delay

| Logic Element | Parameter | Switching Times Minimum | Typical | Maximum | Comment |
|---|---|---|---|---|---|
| NAND, AND/NOR (SN7400, SN7450 etc.) | tpd 0 | 1 | 8 | 15 | assumed minimum |
| | tpd 1 | 7 | 18 | 29 | assumed minimum |
| JK Bistable SN7470 | tpd 0 | 10 | 18 | 50 | clock to output |
| Expander SN7460 | tpd 1 | 10 | 27 | 50 | clock to output |
| | tpd 0 | 1 | 10 | 20 | assumed minimum; delay through expander to output SN7450 |
| | tpd 1 | 6 | 20 | 34 | |

LOGSIM, a versatile logic simulator package developed by the Computer Division of the Marconi Company.

The topology of the logic circuit is defined by labelling the circuit nodes (inputs and outputs of the logic elements) and each element is then positioned by its connections to the various nodes. The basic types of logic gate available in the simulator are AND/OR, NAND/NOR, NOT and DELAY. Consequently it was first necessary to simulate the Texas SN74 elements in terms of basic gates, and then to use these as compound logic elements. The propagation delays of the compound elements (both rise and fall-times) were included in the simulation. Moreover it was possible to use the maximum and minimum values of these times (see Table 3) on successive run-times. The simulator operates on the 'event by event' principle, that is, the states of the specified circuit nodes, and the time taken to reach these states, are computed for various input conditions and presented in a tabulated or graphical form.

The results obtained for the multi-input adder using the simulator showed that the maximum delay time for the circuit was 120 ns, giving an addition time for six 10-bit numbers of 1·2 μs. Since in practice Texas elements are usually well within the upper limits of the delay specification, an average circuit delay of 76 ns can safely be assumed, giving an addition time of less than 1 μs. The total number of packages used in the multi-input adder system was nineteen, representing an overall cost of £24 for the unit, as against £20 for the cascaded 2-input adder system shown in Fig. 1(b).

## 5. Acknowledgments

The author would like to thank J. S. Wright who simulated the multi-adder system, and the Marconi Company for the use of the LOGSIM package.

## 6. References

1. Hennie, F. C., 'Finite-State Models for Logical Machines', (Wiley, New York, 1968).
2. Lewin, D. W., 'Logical Design of Switching Circuits' (Nelson, London, 1968).
3. Humphrey, W. S., 'Switching Circuits with Computer Applications' (McGraw-Hill, New York, 1958).

*Manuscript first received by the Institution on 7th July 1969 and in final form on 16th October 1969 (Short Contribution No. 130/Comp. 126).*

U.D.C. 621.382.2

# Transient Behaviour and Characteristics of the High-field Domain in Gunn-effect Diodes

*By*

Associate Professor
**AKIO SASAKI,**
Ph.D., B.S., M.S.†

Quasi-linear equations are used to analyse characteristics of a high-field domain in Gunn-effect bulk semiconductors. The analysis shows that the differential mobility appearing in the relaxation time of the large-signal analysis is not the same as that used in the small-signal analysis. It is also shown that an equivalent admittance of domain is represented by a parallel connexion of capacitance and conductance which vary with time in the transient state. The equations for the shape of domain and for the time-constant of the admittance are derived. The width of a high-field domain and the displacement current of diodes are discussed. The maximum value of the domain excess potential in the diode biased at the threshold is given. Numerical examples of characteristics of a high-field domain based on the results of the analysis are presented. It is pointed out that non-linear and parametric operations of Gunn-effect diodes can be interpreted by the use of an expression for admittance of the diode in which the effects of r.f. circuit voltage on the domain are taken into account.

## List of Principal Symbols

| | |
|---|---|
| $A$ | cross-sectional area of diode |
| $C_d$ | capacitance of domain |
| $C_d'$ | differential capacitance of domain |
| $D$ | diffusion coefficient |
| $E$ | electric field in high-field domain |
| $E_b$ | bias field of diode |
| $E_m$ | maximum field in high-field domain |
| $E_0$ | electric field in low-field region |
| $\Delta E$ | domain excess field, $E-E_0$ |
| $\Delta E_l$ | excess field in trailing edge of high-field domain |
| $\Delta E_r$ | excess field in leading edge of high-field domain |
| $\Delta E(0)$ | initial amplitude of excess field |
| $\Delta E(x_0, t)$ | maximum excess field |
| $G_d$ | conductance of domain |
| $I(t)$ | total current |
| $J(t)$ | total current density |
| $k$ | length parameter by which value of excess field is assumed zero at cathode |
| $L$ | length of diode |
| $n_0$ | doping concentration |
| $u$ | drift velocity of carriers in high-field domain |
| $u_0$ | drift velocity of carriers in low-field region |
| $V_b$ | bias voltage of diode |
| $\Delta V$ | domain excess potential |
| $\Delta V(0)$ | initial amplitude of domain excess potential |
| $x_0$ | position of disturbance occurring near cathode |
| $x'$ | coordinate moving with carrier drift velocity $u$ |
| $\varepsilon$ | permittivity of semiconductor lattice |
| $\mu_d$ | mobility defined by $(u-u_0)/(E-E_0)$ |
| $\mu_L$ | mobility in low-field region |
| $\bar{\mu}_d$ | mobility $\mu_d$ averaged with respect to carrier density |
| $\rho$ | charge density in high-field domain |
| $\rho_0$ | charge density of doping concentration |
| $\Delta\rho$ | density of excess charge in high-field domain, $\rho-\rho_0$ |

## 1. Introduction

A small-signal theory has been applied to Gunn-effect diodes to derive a small-signal admittance, and the conditions for current instability and for a negative resistance.[1-3] A large-signal theory has been used to analyse stable behaviour of a high-field domain in Gunn-effect diodes.[4] Theory is not sufficient to understand transient behaviour of the domain, which has been investigated mostly by computer analysis.[2,5] Theoretical work on transient behaviour of the domain is required to understand transient phenomena of Gunn-effect oscillations and non-linear parametric operations, and of Gunn-effect diodes, such as are used in high-speed switching elements, frequency mixers, frequency up-converters, and self-pumped oscillators.[6-9]

Quasi-linear equations are used in this paper to analyse transient and stable behaviour of a high-field domain in Gunn-effect diodes. The analysis shows that an equivalent admittance of a domain is represented by a parallel connexion of capacitance and conductance which vary with time in the transient state. The equations for the shape of a high-field domain and for the time-constant of the admittance are derived. The width of a high-field domain and the

† Department of Electrical Engineering, Kyoto University, Kyoto, Japan.

displacement current of diodes are discussed. Numerical examples of characteristics of a high-field domain based on the results of the analysis are given. It is pointed out that non-linear and parametric operations of Gunn-effect diodes can be interpreted by the use of an expression for admittance of the diode in which the effects of r.f. circuit voltage on the domain are taken into account.

## 2. Equations for Domain

Transient behaviour of a high-field domain has been in most cases studied by computer analysis in which the understanding of transient behaviour is limited to specified cases reported previously.[2,5] Only a few papers have studied the growth of the domain in a theoretical analysis.[10,19] Transient behaviour has thus not been sufficiently investigated to provide an understanding of non-linear or parametric phenomena in Gunn-effect diodes. In this section quasi-linear differential equations for the domain in a transient state are derived, and in subsequent sections the solutions to the equations are given.

We consider a uniformly-doped bulk semiconductor in which the drift velocity of carriers depends non-linearly on the electric field, such as in GaAs and InP. A bulk semiconductor diode of uniform cross-sectional area $A$ and of length $L$ is considered. As discovered by J. B. Gunn[11], a disturbance in the field near the cathode contact (the low-voltage side) of a diode grows to a high-field domain when the applied field to the diode is in the range where the bulk semiconductor shows a negative differential mobility. There are two regions of the field in an oscillating diode: one is a low-field region; the other is a high-field region (customarily called a high-field domain), as shown in Fig. 1(a). The total current density $J(t)$ in the low-field region is given by

$$J(t) = \rho_0 u_0(t) + \varepsilon \frac{\partial}{\partial t} E_0(t) \qquad \text{.....(1)}$$

where, for convenience in the analysis, the charge of the carriers is assumed positive. The results obtained from the analysis are applicable to n-GaAs and n-InP by changing the sign of the charge. In the low-field region the field $E_0(t)$ is assumed to have no spatial variation which implies by Poisson's equation that the value of the charge density is equal to the value of the charge of the doping concentration $\rho_0$. In eqn. (1), a conduction current is given by the first term where $u_0(t)$ is the drift velocity of the carriers in the low-field region, and a displacement current is given by the second term where $\varepsilon$ is the permittivity of the semiconductor. The diffusion current in the low-field region is zero because of spatial uniformity of charge density. The total current density in the high-field domain is given by

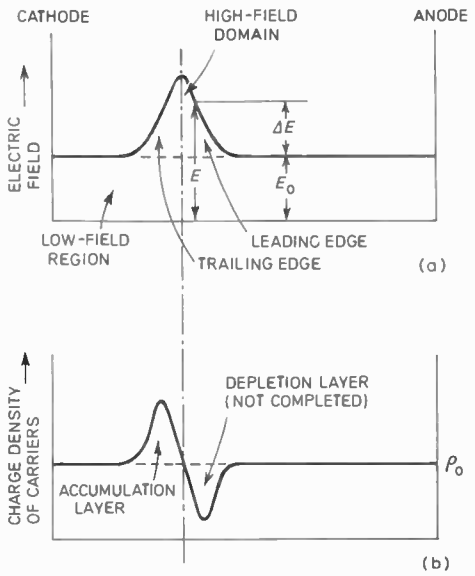


Fig. 1. Distribution of electric field (a) and charge density of carriers (b) in Gunn-effect diode with fractional depletion of carriers in leading edge.

$$J(t) = \rho(x, t)u(x, t) + \varepsilon \frac{\partial}{\partial t} E(x, t) - D \frac{\partial}{\partial x} \rho(x, t) \text{.....(2)}$$

where the charge density $\rho$, the drift velocity $u$ of carriers, and the electric field $E$ vary not only with time $t$ but also with position $x$ in the high-field domain. In eqn. (2) the total current in the high-field domain is obtained by the sum of the conduction, the displacement, and the diffusion currents, respectively, where $D$ is the diffusion coefficient. The term $\rho(\partial D/\partial x)$ is neglected in eqn. (2) since it has little effect on the analysis and complicates physical understanding of the results. The field dependency of the diffusion coefficient is, however, taken into account when the value of the average diffusion coefficient of the domain is computed in Section 6. The total current density $J$ is a function of only the time $t$ since total current density is continuous through a diode with a uniform cross-sectional area. The Poisson equation in a high-field domain is

$$\frac{\partial}{\partial x} E(x, t) = \frac{1}{\varepsilon} \left\{ \rho(x, t) - \rho_0 \right\} \equiv \frac{1}{\varepsilon} \Delta\rho(x, t) \text{ .....(3)}$$

Using the continuity of total current, and putting equation (1) equal to equation (2), we have

$$D \frac{\partial^2}{\partial x^2} \Delta E(x, t) - u(x, t) \frac{\partial}{\partial x} \Delta E(x, t) - \frac{\rho_0 \mu_d}{\varepsilon} \Delta E(x, t) = \frac{\partial}{\partial t} \Delta E(x, t) \qquad \text{.....(4a)}$$

$$\Delta E(x, t) = E(x, t) - E_0(t) \qquad \text{.....(4b)}$$

$$\mu_d(E, E_0) = \frac{u(E) - u_0(E_0)}{E = E_0} \qquad \text{.....(4c)}$$

where $\Delta E(x,t)$ is the electric field which is the difference between the fields in the high-field domain and the low-field region, as shown in Fig. 1(a). The parameter $\mu_d$ has the dimensions of mobility and is considered to be a function of the fields $E$ and $E_0$. It is interesting to notice that eqn. (4a) is a very similar equation to that for the perturbation in the charge density of a bulk semiconductor examined by the Haynes-Shockley experiment,[12,13] although in eqn. (4a) the diffusion coefficient and the mobility parameter depend strongly on the field. In eqn. (4a), which is the equation for a domain excess field $\Delta E$, the three terms in the left-hand side can be interpreted in the following way: the first term represents the diffusion effect of spreading in width; the second term represents the propagation of the domain excess field $\Delta E$ with the velocity $u(x, t)$; and the third term represents change of the domain at the rate of the relaxation time $\varepsilon/\rho_0\mu_d$, growing with negative $\mu_d$ and decaying with positive $\mu_d$. In a semiconductor in which the drift velocity is linearly proportional to the field, a perturbation in the field decays to zero since the mobility given in eqn. (4c) is always positive. On the other hand, in a semiconductor which exhibits the Gunn-effect, the mobility $\mu_d$ can be negative as long as the drift velocity $u(E)$ of carriers in the domain is slower than the drift velocity $u_0(E)$ of carriers in the low-field region. Thus a perturbation in the field grows because the slow velocity of carriers in the domain causes a depletion region in the leading edge and an accumulation region in the trailing edge. The mobility $\mu_d$ given in eqn. (4c) reduces to the differential mobility $(\partial u/\partial E)$ in a small-signal treatment when the difference of the field $\Delta E$ tends to the value being considered as a perturbation. In a large-signal treatment, the mobility in the relaxation time is not given by the differential mobility. As long as the mobility $\mu_d$ is positive, there is a decay of the domain in diodes even if the differential mobility $(\partial u/\partial E)$ of the carriers in the domain is negative. The decay of the domain, other than at the anode contact (the high-voltage side) of diodes, has been seen in the figures of a high-field domain presented in the flip-page sequence III given by computer analysis.[2]

## 3. Transient Behaviour of Domain

The distribution of the charge density of the carriers in a high-field domain is shown in Figs. 1(b) and 3(b). The carriers are depleted in the leading edge and accumulated in the trailing edge. The carriers in the leading edge cannot be depleted more than the doping concentration. When the carrier depletion in the leading edge becomes complete, the leading edge spreads in width, as shown in Fig. 3(b). For simplicity, the analysis of the domain growth is divided in two parts: the first analyses the transient behaviour with a fractional depletion of carriers in the leading edge and does not take into account the effects on the domain growth of the limitation in carrier depletion; the second analyses the transient behaviour with a complete depletion of carriers in the leading edge, assuming the replacement of an almost complete depletion by a complete depletion with the same amount of depleted charge.

### 3.1 Growth of Domain with Fractional Depletion

The diffusion coefficient $D$, the drift velocity $u$, and the mobility $\mu_d$ in eqn. (4a) depend strongly on the field. They could be assumed nearly constant, however, when eqn. (4a) is applied in a sufficiently short time that their variations are small enough to neglect. The coefficients for the subsequent short time can be obtained from the field distribution for the previous short time since the coefficients are functions of the field. By postulating an initial disturbance in the field, we could study transient behaviour of the domain in successive short time intervals until the domain reaches a stable state. By transferring eqn. (4a) to the coordinate

$$x' = x - ut \qquad \text{.....(5)}$$

we analyse the field in the coordinates moving with the carrier velocity $u$ in the domain and we obtain

$$D\frac{\partial^2}{\partial x'^2}\Delta E(x', t) - \frac{\rho_0\mu_d}{\varepsilon}\Delta E(x', t) = \frac{\partial}{\partial t}\Delta E(x', t) \qquad \text{.....(6)}$$

The field in an initial disturbance is assumed to have a Gussian distribution which is expressed by

$$\Delta E(x, 0) = \Delta E(0)\exp\left[-\frac{(x-x_0)^2}{k}\right] \qquad \text{.....(7)}$$

where $\Delta E(0)$ is an initial amplitude of the field, $x_0$ is the position of the disturbance occurring near the cathode $x = 0$, and $k$ is such a small value of the length parameter that the value of the excess field $\Delta E$ is assumed zero at the cathode in the analysis. The potential in an initial disturbance is obtained by integrating eqn. (7) from the cathode $x = 0$ to the anode $x = L$, we have

$$\Delta V(0) = \sqrt{k\pi}\,\Delta E(0) \qquad \text{.....(8)}$$

where zero excess fields at the cathode and the anode are assumed. From eqn. (6) the field distribution in the domain is obtained as

$$\Delta E(x', t) = \frac{\Delta V(0)}{\sqrt{k\pi + 4\pi Dt}}\exp\left[-\frac{\rho_0\mu_d}{\varepsilon}t - \frac{(x'-x_0)^2}{k+4Dt}\right] \qquad \text{.....(9)}$$

which satisfies the initial disturbance given by eqn. (7). In eqn. (9) the term $\exp[-(x'-x_0)^2/(k+4Dt)]$ describes the Gaussian distribution of the field in the

domain, the term $\exp(-\rho_0\mu_d t/\varepsilon)$ describes the domain growth at the rate of the inverse relaxation time $(\rho_0\mu_d/\varepsilon)$, when the mobility $\mu_d$ is negative, and the term $\sqrt{k\pi+4\pi Dt}$ describes the spread in width with time by the diffusion effect. The integration of the field distribution gives the potential of the domain,

$$\Delta V(t) = \Delta V(0)\exp\left[-\frac{\rho_0\mu_d}{\varepsilon}t\right] = \sqrt{k\pi+4\pi Dt}\cdot\Delta E(x_0, t) \quad \text{.....(10)}$$

where $\Delta E(x_0, t)$ is the maximum field in the domain. The expression of eqn. (6) in terms of the potential rather than the field becomes

$$\left(\rho_0\mu_d+\frac{2\varepsilon D}{k+4Dt}\right)\frac{\Delta V(t)}{\sqrt{k\pi+4\pi Dt}} + \frac{\partial}{\partial t}\left\{\frac{\varepsilon}{\sqrt{k\pi+4\pi Dt}}\cdot\Delta V(t)\right\} = 0 \quad \text{.....(11)}$$

It can be seen that the admittance of the domain of the excess field can be represented by the parallel connexion of the conductance

$$G_d(t) = \left(\rho_0\mu_d+\frac{2\varepsilon D}{k+4Dt}\right)\frac{1}{\sqrt{k\pi+4\pi Dt}} \quad \text{...(12)}$$

and the capacitance

$$C_d(t) = \frac{\varepsilon}{\sqrt{k\pi+4\pi Dt}} \quad \text{.....(13)}$$

both of which show time variation. It is seen in eqn. (11) that the total current is zero in the domain. The term $\sqrt{(k\pi+4\pi Dt)}$ in eqns. (12) and (13) is the effective length of the domain, as can be understood in eqn. (10), where it appears as the ratio of the potential $\Delta V(t)$ to the field $\Delta E(x_0, t)$. The term $\rho_0\mu_d$ is a negative conductivity resulting from the negative mobility, and the term $2\varepsilon D/(k+4Dt)$ is positive conductivity resulting from the diffusion effect. It should be noticed that the time variation of the effective length $\sqrt{(k\pi+4\pi Dt)}$ depends on the relative value of the initial length $\sqrt{(k\pi)}$ to the variable length $\sqrt{(k\pi Dt)}$; large variation of the effective length or of the capacitance could not be expected if $k\pi \gg 4\pi Dt$ for the time period being considered. Substituting eqn. (9) into Poisson's equation (3), we obtain the distribution of the charge density of the carriers in the domain:

$$\Delta\rho(x', t) = \frac{2\varepsilon(x'-x_0)}{k+4Dt}\Delta E(x', t) \quad \text{.....(14)}$$

which is shown in Fig. 1(b). The integration of the charge density in the leading or trailing edge gives the charge $\Delta Q(t) = \varepsilon\Delta V(t)/\sqrt{(k\pi+4\pi Dt)}$. Using the definition of the capacitance $C_d(t) = \Delta Q(t)/\Delta V(t)$, we obtain the domain capacitance already derived in eqn. (13). The differential capacitance, defined as

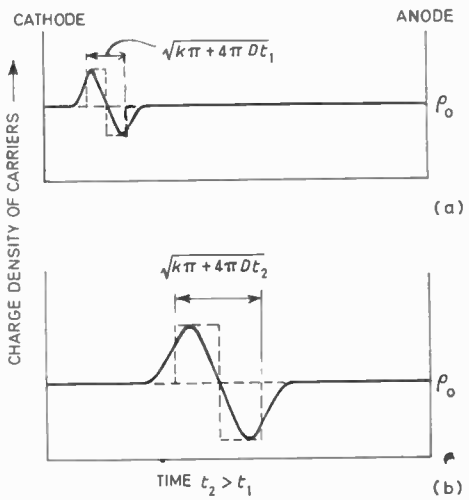


Fig. 2. Distribution of charge density of carriers where the area under the dotted line is equal to the area under the solid line, and thus $\sqrt{k\pi+4\pi Dt}$ can be considered as effective width of domain.

$C'_d(t) = \partial\{\Delta Q(t)\}/\partial\{\Delta V(t)\}$, is often of interest and is in the present case given by $C'_d(t) = C_d(t)$ since the charge $Q(t)$ is a linear function of the voltage $\Delta V(t)$.

The admittance of the domain can be interpreted in Fig. 2 where the charge distributions of the carriers are shown. With the domain growing, the carriers are being depleted in the leading edge and accumulated in the trailing edge. There are, in Fig. 2(b), larger depleted and accumulated regions than in Fig. 2(a). Although in practice the accumulation is formed by carriers coming behind the trailing edge of the domain, and the depletion by carriers moving forward from the leading edge, it could be considered that both the depletion and the accumulation are formed by a virtual transfer from the leading edge to the trailing edge. There is in the domain an effective velocity component directed from the leading edge to the trailing edge whereas the total carrier in the diode moves from the cathode contact to the anode. Negative conductance of the domain thus can be considered as resulting from the inverse directed velocity component of the carriers in the domain. Positive conductance of the domain, on the other hand, results from the diffusion velocity directed from the trailing edge to the leading since the carrier density in the trailing edge is larger than that in the leading edge. The existence of the capacitance in the domain can be interpreted by saying that the carrier distribution of the domain corresponds to the charge distribution of the space-charge region in a p-n diode where the width of the region is given by $\sqrt{(k\pi+4\pi Dt)}$.

On applying a bias voltage $V_b$ to a diode of length $L$, we have

$$V_b = E_b L + \Delta V(0) \quad \text{.....(15)}$$

where $E_b$ is the bias field of the diode. After an initial potential $\Delta V(0)$ grows up to $\Delta V(t)$ in the diode, the electric field of the low-field region decreases from $E_b$ to $E_0(t)$ which satisfies

$$V_b \cong E_0(t)L + \Delta V(t) \qquad \text{.....(16)}$$

where the r.f. circuit voltage induced by the diode is assumed small compared with the d.c. bias voltage $V_b$. From eqns. (15) and (16), we obtain the field of the low-field region

$$E_0(t) = E_b - \frac{1}{L}\{\Delta V(t) - \Delta V(0)\} \qquad \text{.....(17)}$$

Substituting the field $E_0(t)$ into the equation:

$$J_0(t) = \rho_0 \mu_L E_0(t) + \varepsilon \frac{\partial}{\partial t} E_0(t) \qquad \text{.....(18)}$$

we can calculate the total current density of the diode. In eqn. (18), the conduction current is given by the first term where $\mu_L$ is the carrier mobility in the low-field region, and the displacement current is given by the second term.

### 3.2 Growth of Domain with Complete Depletion

The leading edge spreads in width as the charge depletion in the leading edge approaches completion. For simplicity of analysis, an almost complete depletion is replaced by a complete depletion with the same amount of depleted charge. The accumulation region is assumed to grow continuously according to the results obtained in Section 3.1. The field distribution of the trailing edge $\Delta E_l(x', t)$ is thus given by eqn. (9). The subscript $_l$ of $\Delta E_l$ denotes the left-hand side of the domain, but not the leading edge which is in the right-hand side of the domain. The field distribution of the leading edge $\Delta E_r(x', t)$ is obtained by solving Poisson's equation and applying the condition of field continuity, $E_l(x_0, t) = E_r(x_0, t)$, at $x' = x_0$ which is the boundary between the trailing and leading edges as shown in Fig. 3.

$$\Delta E_r(x', t) = -\frac{\rho_0}{\varepsilon}(x' - x_0) + \frac{\Delta V(0)}{\sqrt{k\pi + 4\pi Dt}} \exp\left[-\frac{\rho_0 \mu_d}{\varepsilon} t\right] \qquad \text{.....(19)}$$

The field distribution of the trailing edge is mainly affected by the diffusion effect; the field distribution of the leading edge is mainly affected by the charge of the impurity concentration, $\rho_0$. The width $(w' - x_0)$ of a complete depletion region is derived from the equation $\Delta E_r(w', t) = 0$ which represents zero excess field at the edge $x' = w'$ of the depletion region.

$$w' - x_0 = \frac{\varepsilon \Delta V(0)}{\rho_0 \sqrt{k\pi + 4\pi Dt}} \exp\left[-\frac{\rho_0 \mu_d}{\varepsilon} t\right] \qquad \text{...(20)}$$

This shows that the width of a complete depletion region spreads with growth of the maximum field of the domain,

$$\Delta E(x_0, t) = \Delta V(0) \exp(-\rho_0 \mu_d t/\varepsilon)/\sqrt{k\pi + 4\pi Dt}.$$

The potential of a domain is obtained by the integration of the field $\Delta E_l(x', t)$ from the cathode contact to $x' = x_0$ and the integration of the field $\Delta E_r(x', t)$ from $x' = x_0$ to $x' = w'$.

$$\Delta V(t) = \frac{\Delta V(0)}{2} \exp\left[-\frac{\rho_0 \mu_d}{\varepsilon} t\right] + \frac{\varepsilon}{2\rho_0}\{\Delta E(x_0, t)\}^2 \qquad \text{.....(21)}$$

where the first term presents the potential of the trailing edge and the second the potential of the leading edge. With sufficient growth of the domain, the potential of the leading edge becomes larger than

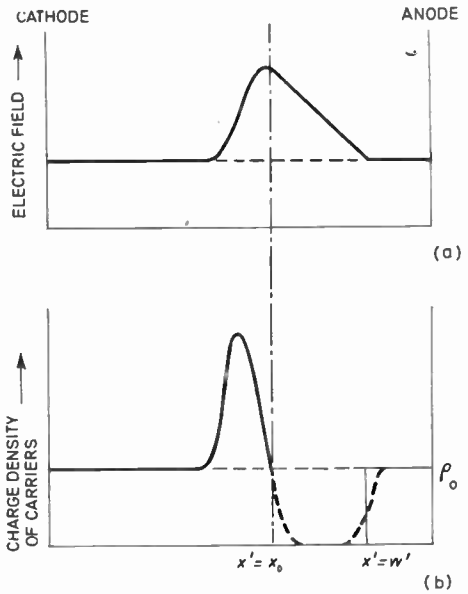


Fig. 3. Distribution of electric field (a) and charge density of carriers (b) in Gunn-effect diode with complete depletion of carriers in leading edge.

the potential of the trailing edge. Thus the potential, with sufficient growth of the domain, becomes proportional to the square of the maximum excess field of the domain, $\Delta E(x_0, t)$. This proportionality has been observed in the experiments on the shape of travelling domains in GaAs by J. B. Gunn[14] and the experiments on high-field dipole domains in GaAs by I. Kuru *et al.*[15] The charge of the domain, $\Delta Q(t)$, is obtained by the assumption of charge neutrality in the diode:

$$\Delta Q(t) = \rho_0(w' - x_0) = \varepsilon \Delta E(x_0, t) \qquad \text{.....(22)}$$

With sufficient growth of the domain, the charge

$\Delta Q(t)$ is proportional to the square root of the domain voltage, $\sqrt{\Delta V(t)} \cong \sqrt{\varepsilon/2\rho_0}.\Delta E(x_0, t)$, which has been measured experimentally.[14] The application of the definitions of the capacitance and the differential capacitance to eqns. (21) and (22) gives

$$C_d(t) = \frac{\Delta Q(t)}{\Delta V(t)} = \frac{2\varepsilon}{\sqrt{k\pi + 4\pi Dt} + (w' - x_0)} \quad \text{.....(23a}$$

and

$$C'_d(t) = \frac{\partial \Delta Q(t)}{\partial \Delta V(t)} = \frac{\varepsilon}{\frac{1}{2}\sqrt{k\pi + 4\pi Dt} + (w' - x_0)} \quad \text{.....(23b)}$$

which show that the values of these capacitances are decreasing with time. The differential capacitance $C'_d(t)$ is different from the capacitance $C_d(t)$ since the charge is not a linear function of the voltage $\Delta V(t)$. In the differential capacitance, the first term of the denominator represents the effective width of the accumulation region and the second the width of the depletion region. If, as obtained in Section 3.1, the total current in the domain is assumed to be zero here,

$$G_d(t).\,\Delta V(t) + \frac{\partial}{\partial}\{C_d(t).\Delta V(t)\} = 0, \quad \text{.....(24)}$$

we can derive the conductance $G_d(t)$:

$$G_d(t) = \left(\rho_0\mu_d + \frac{2\varepsilon D}{k + 4D}\right) \times \frac{2}{\sqrt{k\pi + 4\pi Dt} + (w' - x_0)} \quad \text{.....(25)}$$

where the denominator has length dimensions and the same value as that in the capacitance $C_d(t)$; and where the term $\rho_0\mu_d$ represents negative conductivity resulting from the negative mobility and the term $2\varepsilon D/(k + 4Dt)$ represents positive conductivity resulting from the diffusion effect. The fields of the low-field region $E_0(t)$ and the total current density of the diode $J_0(t)$ are calculated by eqns. (17) and (18) given in Section 3.1.

When the domain reaches a steady state, it can be expected for the domain not to vary with time. There is no displacement current in the domain, which by eqn. (24) implies zero conductance of the domain. In a steady state, no effective transfer of the carriers occurs between the leading and trailing edges. The admittance of the domain in a steady state is represented by the capacitance determined by the carrier distributions of the leading and trailing edges.

### *3.3 Extinction of Domain at the Anode Contact*

The carrier distribution of the metal near the anode contact is disturbed by the arrival of the depletion region of the domain. The disturbances are extinguished at the rate of the dielectric relaxation time $\varepsilon/\sigma_m$ where $\sigma_m$ is the conductivity of the metal. As the conductivity of the metal is large, the disturbances would be assumed to be extinguished the instant the depletion region of the domain arrives at the anode contact. Transient behaviour of the domain being extinguished at the anode contact is studied in this section by a simple analysis in which zero relaxation time of the metal is assumed. At the time $t$ after the depletion region arrives at the anode contact, the width of the depletion region is given by

$$(w'_s - x_0 - \mu_L E_0(t)t),$$

where $(w'_s - x_0)$ is the width of the domain in the steady state and the domain velocity is approximated by the velocity of the carriers in the low-field region, $\mu_L E_0(t)$. The neutrality of total charge in the diode implies

$$\frac{\varepsilon \Delta V(0)}{\sqrt{k\pi + 4\pi Dt'}} \exp\left[-\frac{\rho_0\mu_d}{\varepsilon}\,t'\right] = \rho_0\{w'_s - x_0 - \mu_L E_0(t)t\} \quad \text{.....(26)}$$

where the left-hand side gives the charge in the accumulation region and the right the charge in the depletion region. In eqn. (26), $t'$ denotes a time parameter which decreases with increasing values of the time $t$ because the accumulation region must decrease with the time $t$. The bias voltage $V_b$ is expressed by

$$V_b = E_0(t)L + \frac{\Delta V(0)}{2} \exp\left[-\frac{\rho_0\mu_d}{\varepsilon}\,t'\right] + \frac{\rho_0}{2\varepsilon}\{w'_s - x_0 - \mu_L E_0(t)t\}^2 \quad \text{.....(27)}$$

where the r.f. circuit voltage is assumed small compared with the d.c. bias voltage $V_b$. In eqn. (27) the first, second, and third terms represent the potentials of the low-field region, of the trailing edge, and of the leading edge, respectively. The field $E_0(t)$ and the time parameter $t'$ are obtained from eqns. (26) and (27) at a given time $t$. The use of the potential of the domain and the charge given by eqn. (26) with the definitions for capacitance and differential capacitance gives the domain capacitance:

$$C_d(t) = \frac{2\varepsilon}{\sqrt{k\pi + 4\pi Dt'} + \{w'_s - x_0 - \mu_L E_0(t)t\}} \quad \text{.....(28a)}$$

and the differential capacitance of the domain:

$$C'_d(t) = \frac{\varepsilon}{\frac{1}{2}\sqrt{k\pi + 4\pi Dt'} + \{w'_s - x_0 - \mu_L E_0(t)t\}} \quad \text{.....(28b)}$$

The first and second terms in the denominator of $C'_d(t)$ are respectively the effective widths of the trailing and the leading edges. As these terms decrease with time the capacitances $C_d(t)$ and $C'_d(t)$ of the domain being extinguished at the anode contact, increase with time. The conductance is obtained from eqn. (24); the width of the domain is given by the denominator of eqn. (28b); the field distribution of the trailing edge is given by eqn. (9), using the time parameter $t'$ in place of the time $t$; the field distribution of

the leading edge is given by

$$\Delta E_r(x', t) = -\frac{\rho_0}{\varepsilon}\{w_s' - x_0 - \mu_L E_0(t)t\} + \\ + \frac{\Delta V(0)}{\sqrt{k\pi + 4\pi D t'}} \exp\left[-\frac{\rho_0 \mu_d}{\varepsilon} t'\right];$$

the domain potential is given by the second and third terms in eqn. (27); and the total current density is obtained from eqn. (18). The time for the domain to be extinguished at the anode contact can be approximated by the time when the width of the domain reduces to the width of the initial disturbance, $\sqrt{(k\pi)}$. The time obtained from this calculation would not be an accurate value of the time for extinction, but could give an approximate value of it.

## 4. Domain Characteristics

### *4.1 Domain Shape*

Two types of domain shape could be considered when the domain reaches a steady state: one with a fractional depletion in the leading edge; the other with a complete depletion in the leading edge. As shown in Fig.1(a), a domain with a fractional depletion is in the shape of a Gaussian distribution which is symmetrical with respect to the position of maximum field. The shape of a domain with a complete depletion is asymmetrical as shown in Fig. 3(a). The potential of a domain with a complete depletion is generally larger than that of a domain with a fractional depletion because it reaches a steady state through the process of growth of a domain with a fractional depletion. It can be said that the shape of the domain with a relatively small potential is a symmetrical triangle and that the shape of the domain with a relatively large potential is an asymmetrical triangle. These shapes have been observed in experiments.[14]

### *4.2 Domain Excess Potential*

The approximate value of the potential of a domain in a steady state is calculated by a simple equation. Neglecting an initial potential $\Delta V(0)$ in eqns. (16) and (17), we obtain

$$\frac{\Delta V(t)}{V_b} = 1 - \frac{E_0}{E_b} \qquad \text{.....(29)}$$

in which the value of $\Delta V(t)/V_b$ is 54% when the threshold field 3·25 kV/cm is used for the bias field $E_b$ and a minimum sustaining field (about 1·5 kV/cm) is used for the field $E_0$ in the low-field region.

### *4.3 Time-Constant of the Domain Admittance*

The time-constant of the admittance of the domain with a fractional depletion is derived by using eqns. (12) and (13).

$$\frac{1}{\tau_c} = \frac{G_d(t)}{C_d(t)} = \frac{\rho_0 \mu_d}{\varepsilon} + \frac{2D}{k + 4Dt} \qquad \text{.....(30)}$$

It is interesting to see that the time-constant of the domain admittance relates closely to the dielectric relaxation time. As $\mu_d$ is negative for the domain growth, the second term in eqn. (30) indicates the reduction of the growth rate by the diffusion effect. The time-constant of the admittance of the domain with a complete depletion is derived from eqns. (23a) and (25), and it is given by the same expression as that of eqn. (30).

## 5. Non-linear or Parametric Operation of Diode

A time-varying admittance is derived for a diode which is treated as an active element of a circuit. When the diode is biased by the direct voltage $V_b$ and the r.f. circuit voltage $\Delta V_c(t)$, the voltage equation (16) is rewritten as

$$V_b + \Delta V_c(t) = E_0(t)L + \Delta V(t) \qquad \text{.....(31)}$$

where the r.f. circuit voltage can either be induced in the circuit by the domain voltage or introduced as an applied r.f. voltage, not necessarily of the same frequency or variation as the domain voltage. Substituting $E_0(t)$ into the total current $I(t) = A.J(t)$ where $A$ is the cross-sectional area of a diode and $J(t)$ is the total current density given by eqn. (1), we obtain

$$\Delta I(t) = G_p(t) \,.\, \Delta V_c(t) + \frac{\partial}{\partial t}\{C_p(t) . \Delta V_c(t)\} \qquad \text{.....(32a)}$$

$$\Delta I(t) = I_0(t) - I\,, \quad I = \frac{1}{T}\int_0^T I_0(t)\mathrm{d}t \qquad \text{.....(32b)}$$

$$G_p(t) = \frac{G_0 . V_b - I}{\Delta V_c(t)} + G_0\left\{1 - \frac{\Delta V(t)}{\Delta V_c(t)}\right\} \qquad \text{.....(32c)}$$

$$C_p(t) = C_0\left\{1 - \frac{\Delta V(t)}{\Delta V_c(t)}\right\} \qquad \text{.....(32d)}$$

where $T$ is the period of the domain transit in a diode, $G_0$ is a low-field conductance given by $A\rho_0\mu_L/L$, $C_0$ is the geometrical capacitance given by $A\varepsilon/L$, and $\Delta I(t)$ is the r.f. current obtained by subtracting the d.c. component $I$ from the total current $I_0(t)$. It is seen in eqn. (32a) that the terms $G_p(t)$ and $C_p(t)$ could be considered to be the conductance and the capacitance of the diode which is treated as an active element of a circuit. The domain voltage $\Delta V(t)$ in the conductance $G_p(t)$ and capacitance $C_p(t)$ varies not only with the frequency determined by the length of the diode but also with the frequency of the circuit voltage which affects the domain growth non-linearly. The conductance $G_p(t)$ and the capacitance $C_p(t)$, which vary non-linearly with respect to the applied r.f. voltage

and parametrically with respect to time, allow interpretation of the non-linear or parametric operation† of diodes when used as frequency mixers, frequency up-converters and self-pumped oscillators.

## 6. Numerical Examples of Domain Characteristics

Transient and stable characteristics of domains are shown in numerical examples calculated by the analytical results obtained in previous sections where the diffusion coefficient $D$, the drift velocity $u$, and the mobility $\mu_d$ have been assumed approximately constant in a very short time $\Delta t$. The growth of the disturbance for the time $t = \Delta t$, from $t = 0$ to $t = \Delta t$, can be calculated by using an initial disturbance in field and potential, and initital values of the diffusion $D$, the velocity $u$ and the mobility $\mu_d$. In a subsequent time interval from $t = \Delta t$ to $t = 2\Delta t$, the growth of the disturbance is calculated by using the coefficients which are averaged with respect to the carrier density at time $t = \Delta t$; for example,

$$\bar{\mu}_d = \frac{\int_{E_o}^{E_m} \mu_d \cdot (\rho_l + \rho_r) dE}{\int_{E_o}^{E_m} (\rho_l + \rho_r) dE} \qquad \ldots\ldots(33)$$

where $E_m$ is a maximum field in a high-field domain, and $\rho_l$ and $\rho_r$ are the distributions of the charge density expressed in terms of the electric field. The subscripts l and r denote the left-hand side (trailing edge) and the right-hand side (leading edge) of the domain, respectively. When the charge distributions are symmetrical as shown in Fig. 1(b) and written as $\rho_l = \rho_0 + \Delta\rho(E)$ and $\rho_r = \rho_0 - \Delta\rho(E)$, the average mobility is given by

$$\bar{\mu}_d = \int_{E_0}^{E_m} \mu_d dE/(E_m - E_0) \qquad \ldots\ldots(34)$$

In a domain with a complete depletion region, the leading edge is not taken into account for evaluating the average mobility $\bar{\mu}_d$ since there are no carriers in the leading edge: $\rho_r = 0$. The mobility of the region between a low-field $E_0$ and the threshold field $E_T$ in a domain would act to suppress the growth of the domain because the mobility in this region reduces the absolute value of a negative mobility $\mu_d$ in the evaluation of eqn. (33). Thus the average mobility given by eqn. (33) takes into consideration such effects as the lack of carriers in the leading edge and the suppression of domain growth by the low-field mobility in the domain. The velocity-field characteristic shown in Fig. 4, which is approximated from that derived theoretically by Butcher and Fawcett,[16] is used in making the calculations. The field dependency of the diffusion coefficient is also taken into account in the calculations, and the diffusion coefficient-field characteristic approximated from that given theoretically by Butcher *et al.*[17] is used. The average diffusion is evaluated by the technique of eqn. (33).

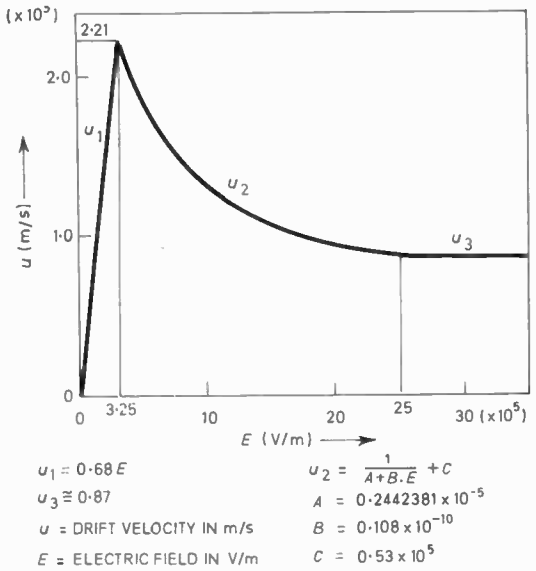


**Fig. 4.** Velocity-field characteristic used in computation.

The potential corresponding to thermal energy at room temperature, 0·025 V, is assumed as the value of the initial potential $\Delta V(0)$. It is generally considered[18] that significant departures from electrical neutrality are not found over distances greater than about four or five times the Debye length $L_d$. Thus we could choose five times the Debye length as an initial value of the effective width of the domain, $\sqrt{(k\pi)}$. It could be understood for uniformly-doped semiconductors that the values of $\Delta V(0) = 0{\cdot}025$ V and $\sqrt{(k\pi)} = 5L_D$ were determined by one of the methods to decide what are initial disturbances in theoretical analysis. In actual cases of the Gunn-effect diodes, initial disturbances could be caused, for example, by non-uniformity in doping and non-ohmic characteristics of the cathode contact.

The impurity concentration of $2{\cdot}0 \times 10^{20}\text{m}^{-3}$ and a low-field resistivity of 4·6 ohm-cm are used in the calculations of transient and stable characteristics of domains in Gunn-effect diodes. Numerical examples of domain characteristics are shown in Figs. 5–7, for three different values of the product $n_0L$, the time for the domain growth is taken as the time from the initial perturbation until the field of the domain stops increasing. The value of $t/T$ in the abscissa of the figures indicates the ratio of the time $t$ to the period $T$, which is the transit time of the domain through the sample length with average velocity $10^5$m/s.

† A parametric operation of the Gunn-effect diode has been verified by the experiments on a self-pumped parametric amplifier which will be published.

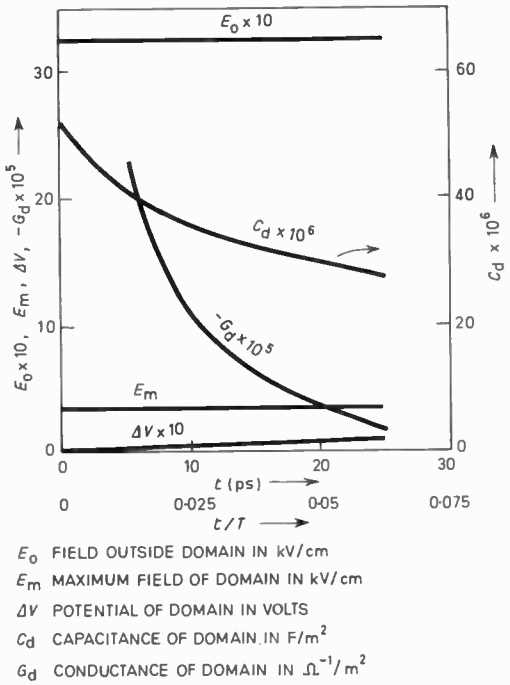


**Fig. 5.** Transient characteristics of domain growing in diode with $n_0 = 2{\cdot}0 \times 10^{20}$ m$^{-3}$ and $L = 40$ μm ($n_0L = 0{\cdot}8 \times 10^{12}$ cm$^{-2}$) and biased at threshold.

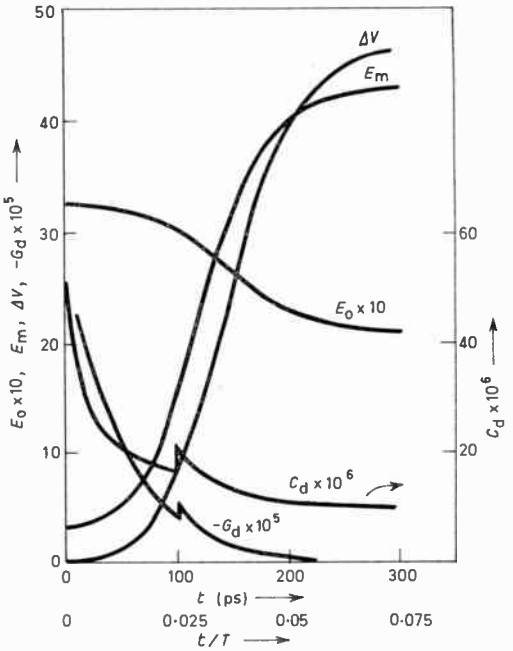


**Fig. 7.** Transient characteristics of domain growing in diode with $n_0 = 2{\cdot}0 \times 10^{20}$ m$^{-3}$ and $L = 400$ μm ($n_0L = 8 \times 10^{12}$ cm$^{-2}$) and biased at threshold. $E_0$, $E_m$, $\Delta V$, $G_d$ and $C_d$ are in the same units as in Fig. 5.

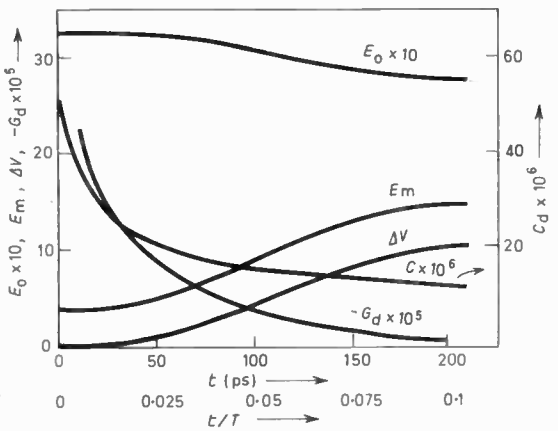


**Fig. 6.** Transient characteristics of domain growing in diode with $n_0 = 2{\cdot}0 \times 10^{20}$ m$^{-3}$ and $L = 200$ μm ($n_0L = 4 \times 10^{12}$ cm$^{-2}$) and biased at threshold. $E_0$, $E_m$, $\Delta V$, $G_d$, and $C_d$ are in the same units as in Fig. 5.

It can be seen in Figs. 5–7 that the capacitance of a domain decreases during domain growth because the effective width of the domain is spreaded by the diffusion effect. It can also be seen that a negative conductance of domain is large at the beginning of the domain growth and then decreases during growth of a domain. The domain growth in a diode always accompanies these variations of the capacitance and the conductance. Larger variations in the fields, the potential, and the admittance of a domain are observed with larger values of the product $n_0L$. The discontinuity appearing in the variations of the capacitance and the conductance in Fig. 7 is attributed to the abrupt change of the effective length of the domain, resulting from the assumption of the replacement of an almost depleted region in the leading edge by a completely depleted region.

Characteristics of domains in a steady state are summarized in Table 1. It is understood in Table 1 that the value of the time for the domain growth ranges between 5 and 10% of the period of the transit-time oscillation of the diode and thus a long time is required to achieve a steady state in a long sample. The potentials of domains are less than 54% of the bias voltage which was the percentage obtained in Section 4.2 as the maximum value of the potential in the domain of a diode biased at the threshold field. The displacement current in a sample is much less than the conduction current. The variation of the total current in a sample biased at the threshold field is approximated by the variation of the electric field outside the domain, as shown in Figs. 5–7. A small capacitance accompanies a large domain potential since the domain grows with spreading width of the domain by the diffusion effect. The width of the leading edge until complete depletion appears in the leading

**Table 1.** Characteristics of domain when it reaches a steady state. Diodes are biased at threshold.

| | | Length of diode μm | | | |
|---|---|---|---|---|---|
| | | 40 | 200 | 400 | 600 |
| $n_0L$ | $cm^{-2}$ | $0{\cdot}8\times10^{12}$ | $4\times10^{12}$ | $8\times10^{12}$ | $12\times10^{12}$ |
| Time for domain growth | ps | 25 | 210 | 300 | 340 |
| Time for domain growth/period of oscillation | | 0·063 | 0·11 | 0·075 | 0·057 |
| Maximum field of domain | kV/cm | 3·4 | 14 | 43 | 58 |
| Potential of domain | volt | 0·08 | 10 | 46 | 77 |
| Potential of domain/bias voltage | | 0·0062 | 0·16 | 0·35 | 0·40 |
| Current density | $A/m^2$ | $7{\cdot}0\times10^{8}$ | $5{\cdot}9\times10^{8}$ | $4{\cdot}6\times10^{8}$ | $4{\cdot}3\times10^{8}$ |
| Displacement current/conduction current | | $0{\cdot}65\times10^{-3}$ | $1{\cdot}7\times10^{-3}$ | $0{\cdot}084\times10^{-3}$ | $0{\cdot}66\times10^{-3}$ |
| Capacitance per unit area | $F/m^2$ | $27\times10^{-6}$ | $12\times10^{-6}$ | $9{\cdot}8\times10^{-6}$ | $8{\cdot}0\times10^{-6}$ |
| Effective width of domain | μm | 4·1 | 9·1 | 18 | 23 |
| Effective width of domain/length of diode | | 0·10 | 0·046 | 0·045 | 0·038 |
| Accumulation width/depletion width | | 1 | 1 | 0·3 | 0·21 |

$n_0 = 2{\cdot}0\times10^{20}\ m^{-3}$
The ratios of the displacement current of the conduction current are given just before the arrival at a steady state.

edge, then the width of the leading edge becomes large compared with the width of the trailing edge. The ratio of the accumulation width to the depletion width becomes small, as shown in the last row in Table 1.

The characteristics of a domain at a steady state are shown in Fig. 8 where the analytical results

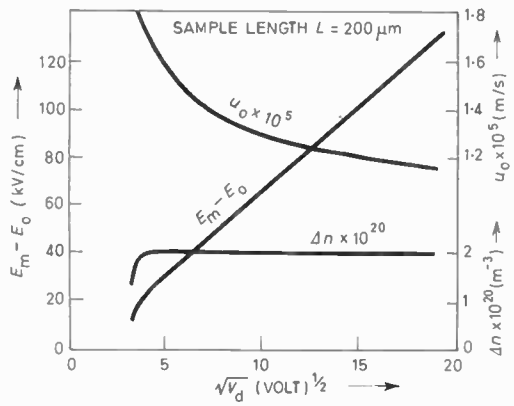


**Fig. 8.** Theoretical variations of carrier velocity $u_0$ outside domain, excess field $(E_m - E_0)$ of domain, and ionized impurity density $\Delta n = \Delta\rho/q$ appearing in the leading depleted region, plotted as functions of the square root of domain voltage $\sqrt{V_D}$. Note different scales and zeros in each quantity.

obtained in Sections 2 and 3 are applied to a diode of $n_0 = 2{\cdot}0\times10^{20}\ m^{-3}$ and $L = 200\ \mu m$ at various applied bias voltages. The voltages are assumed to bias the diode instantaneously beyond the threshold. The characteristics shown in Fig. 8 are qualitatively in good agreement with the experimental data measured by the capacitive probe techniques.[14] The domain excess field $(E_m - E_0)$ is linearly proportional to the square root of the domain voltage, $\sqrt{V_D}$. The carriers in the leading edge are almost depleted, except when the domain field and potential are relatively small. Outside the domain the carrier velocity $u_0$, which is approximately equal to the domain velocity at a steady state, decreases with the increase of domain voltage or domain field. The decrease of the domain velocity can be understood by the negative differential characteristic shown in Fig. 4 which implies slower velocity at higher field. Quantitative agreement can be obtained by the use of slightly different initial conditions and velocity-field characteristic in the computation since the trends of the variations given in Fig. 8 are the same as those measured experimentally.[14]

The time for domain extinction at the anode can be roughly estimated by the ratio of the domain width to the average velocity. In Table 1, the domain width is 18 μm for the diode, biased at the threshold, with

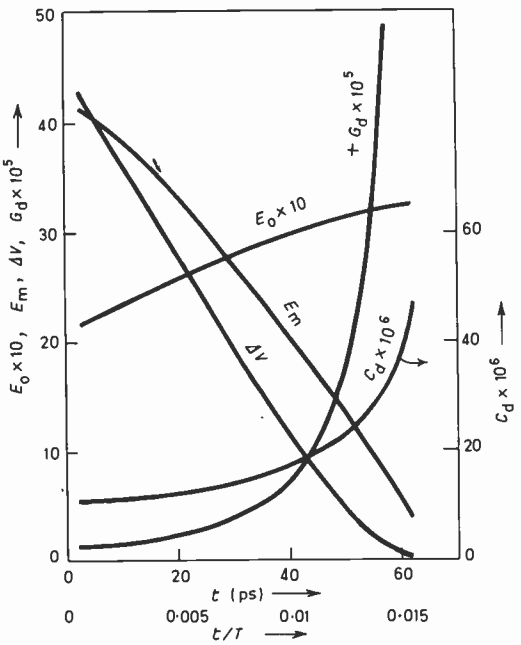


Fig. 9. Transient characteristics of domain being extinguished at the anode of diode with $n_0 = 2{\cdot}0 \times 10^{20}$ m$^{-3}$ and $L = 400$ μm ($n_0 L = 8 \times 10^{12}$ cm$^{-2}$) and biased at threshold. $E_0$, $E_m$, $\Delta V$, $G_d$, and $C_d$ are in the same units as in Fig. 5.

$n_0 = 2{\cdot}0 \times 10^{20}$ m$^{-3}$ and $L = 400$ μm. The time for domain extinction is 180 ps when the average velocity is assumed to be $10^5$m/s. Using the analytical results obtained in Section 3.3, we obtain in Fig. 9, transient characteristics of domain being extinguished at the anode. The time chosen for the extinction is from the arrival of the edge of the domain at the anode to the reduction of the domain width to the width of the initital perturbation. In Fig. 9 we see that the time for the extinction is 63 ps, which is shorter than the value of 180 ps, since the domain velocity becomes larger as the domain field is decreased (see Fig. 4). It is shown in Fig. 9 that the capacitance of a domain being extinguished at the anode is increased because the domain width is becoming shorter. The conductance of a domain being extinguished at the anode is positive and becomes infinite when the domain approaches complete extinction. The variations of the capacitance and the conductance for domain extinction are the inverse of those for domain growth. The sign of the conductance for extinction is opposite to that for growth.

## 7. Conclusions

Quasi-linear equations have been used to analyse the characteristics of domains in Gunn-effect bulk semiconductors. Since the equations have been treated analytically, some physical interpretations have been given to the behaviour of high-field domains observed in experiments. The analysis shows that the differential mobility appearing in the relaxation time of the large-signal analysis is not the same as that used in the small-signal analysis. The differential mobility of the large-signal analysis, however, becomes equal to that of the small-signal analysis when the domain reduces to a perturbation. It is shown in the analysis that an equivalent admittance of a domain is represented by a parallel connexion of capacitance and conductance which vary with time in the transient state. The time-constant of the admittance is shown to equal the dielectric relaxation time plus a term dependent on the diffusion effect. The shape of a domain with a fractional depletion of carriers in the leading edge is expressed by a symmetrical triangle. The shape of a domain with a complete depletion, however, is expressed by an asymmetrical triangle in which the gradient of the leading edge is determined by the density of the ionized impurity and the shape of the trailing edge is determined by the diffusion effect. The depletion width is equal to the accumulation width for a domain of relatively small field and potential. The depletion width increases relative to the accumulation width after complete depletion appears in the leading edge. The maximum value of the domain potential in a diode biased at the threshold is derived to be approximately 54% of the threshold voltage. The displacement current of the diode is shown numerically to be very small in comparison with the conduction current. Thus the total current of the diode is given mainly by the conduction current. The characteristics of a domain calculated from the results of the analysis have been given as numerical examples, which show qualitatively good agreement with the measured values of experiments. It has been pointed out that non-linear and parametric operations of Gunn-effect diodes can be interpreted by the use of an expression for admittance of the diode in which the effects of r.f. circuit voltage on the domain are taken into account.

## 8. Acknowledgments

The author is grateful to the late Professor M. Terada of Osaka University for his suggestions on the definitions of the capacitance and the differential capacitance. He is also grateful to Professors T. Tanaka and T. Takagi for their constant encouragement.

This work was supported in part by the 1967 RCA Research Grant of RCA Research Laboratories, Inc. in Japan.

## 9. References

1. Hobson, G. S., 'Small-signal admittance of a Gunn-effect device', *Electronics Letters*, **2**, pp. 207–8, June 1966.

2. McCumber, D. E. and Chynoweth, A. G., 'Theory of negative-conductance amplification and of Gunn instabilities in "two-valley" semiconductor', *Trans. I.E.E.E.*, **ED-13**, pp. 4–21, January 1966.
3. Sasaki, A. and Takagi, T., 'Conditions for space-charge-wave growth and differential negative resistance in "two-valley" semiconductor', *Proc. I.E.E.E.*, **55**, p. 732, May 1967.
4. Butcher, P. N., Fawcett, W. and Hilsum, C., 'A simple analysis of stable domain propagation in the Gunn effect', *Brit. J. Appl. Phys.*, **17**, pp. 841–50, July 1966.
5. Kroemer, H., 'Non-linear space-charge domain dynamics in a semiconductor with negative differential mobility', *Trans. I.E.E.E.*, **ED-13**, pp. 27–40, January 1966.
6. Shoji, M., 'Bulk semiconductor high-speed current waveform generator', *Proc. I.E.E.E.*, **55**, pp. 720–1, May 1967.
7. Hakki, B. W., 'GaAs post threshold microwave amplifier, mixer, and oscillator', *Proc. I.E.E.E.*, **54**, pp. 290–300, February 1966.
8. Sugimoto, S., 'Up-conversion with Gunn-effect diode', *Proc. I.E.E.E.*, **55**, p. 1520, August 1967.
9. Carroll, J. E., 'Resonant-circuit operation of Gunn diode, a self-pumped parametric oscillator', *Electronics Letters*, **2**, pp. 215–216, June 1966.
10. Kurokawa, K., 'The dynamics of high-field propagating domains in bulk semiconductors', *Bell System Tech. J.*, **46**, pp. 2235–2259, December 1967.
11. Gunn, J. B., 'Instabilities of current in III–V semiconductors', *IBM J. Res. Devl.*, **8**, pp. 141–159, April 1964.
12. Haynes, J. R. and Shockley, W., 'Investigation of hole injection in transistor action', *Phys. Rev.*, **75**, p. 691, February 15, 1949.
13. Adler, R. B., Smith, A. C. and Longini, R. L., 'Introduction to Semiconductor Physics', pp. 177–81 (Wiley, New York, 1964).
14. Gunn, J. B., 'On the shape of traveling domains in gallium arsenide', *Trans. I.E.E.E.*, **ED-14**, pp. 720–1, October 1967.
15. Kuru, I., Robson, P. N. and Kino, G. S., 'Some measurements of the steady-state and transient characteristics of high-field dipole domain in GaAs', *Trans. I.E.E.E.*, **ED-15**, pp. 21–9, January 1968.
16. Butcher, P. N. and Fawcett, W., 'Calculation of the velocity-field characteristics for gallium arsenide', *Phys. Letters*, **21**, pp. 489–90, June 15, 1966.
17. Butcher, P. N., Fawcett, W. and Ogg, N. R., 'Effect of field dependent diffusion on stable domain propagation in the Gunn effect', *Brit. J. Appl. Phys.*, **18**, pp. 755–759, June 1967.
18. Adler, R. B., *et al.*, *op. cit.*, p. 151.
19. Harrison, R., 'Simple transient and non-linear analysis of high-field domain in GaAs', *Brit. J. Appl. Phys.* (*J. Phys. D*), Series 2, **1**, pp. 973–82, August 1968.

*Manuscript first received by the Institution on 11th July 1969 and in final form on 9th October 1969. (Paper No. 1301/CC63)*



## The Author

**Dr. Akio Sasaki** received his B.S. and M.S. degrees in electrical engineering from Kyoto University, Kyoto, Japan, in 1955 and 1957 respectively, and his Ph.D. degree from the University of California, Berkeley, U.S.A., in 1966. From 1957 to 1962 he was engaged in investigations into the interactions between electromagnetic and electron beam waves in microwave devices at the Kobe Industries Corp., Kobe, Japan. From 1963 to 1966 he was a Research Assistant in the Electronics Research Laboratory of the University of California, Berkeley. In 1966 he was appointed as an Assistant in the Department of Electrical Engineering of Kyoto University. He is now an Associate Professor engaged in research in physical electronics and solid-state electronics.

# Automation of Optical Astronomy

The Royal Observatory Edinburgh, one of the seven establishments of the Science Research Council, has accepted and completed post-delivery trials of the GALAXY (General Automatic Luminosity and XY) measuring machine from its manufacturers, Faul Coradi Scotland Limited.

The GALAXY machine is the first of its kind anywhere to bring complete automation to processes of optical astronomy. Coupled with the Observatory's 16-in Schmidt telescope and Elliott 4130 computer system it enables astronomers to program their work in such a way that considerable quantities of astronomical data can be taken from the telescope by the GALAXY machine and fed into the computer for the results to be analysed in a fraction of the time that it has taken in the past.

Work on the machine was first started at the Observatory over five years ago and since then hardware has been designed and constructed by Faul Coradi Scotland Ltd. in conjunction with astrophysicists working at the Observatory.

A GALAXY machine has been ordered for the Royal Greenwich Observatory at Herstmonceux, another establishment of the S.R.C., and delivery is expected in 1971. It is hoped that as a result of this work, further GALAXY machines will find application in medical and industrial, as well as astronomical, fields.

## Exploring the stars

The invention of the Schmidt telescope more than thirty years ago provided astronomers with the means of recording information about the stars at an unprecedented rate. A single photograph of an area of the sky a few times the size of the Moon, taken in a few minutes on a clear, dark night by a Schmidt telescope of even moderate size, records images of tens of thousands of stars. Such photographs contain a wealth of information. Precise measurements of the positions of star images on photographs taken at different times give the angular motions of the stars, enabling their distances to be calculated. The distribution and motions of the stars which make up our Galaxy can be obtained in this way. Measurement of the strengths of the images give the brightnesses of the stars, and by taking photographs through different colour filters the temperatures of the stars can be deduced. Similar measurements enable the distribution of interstellar dust—the Galactic fog—to be determined, dust which increasingly appears to play a crucial role in the formation of stars and the evolution of galaxies.

The task of extracting all the information from the photographs, of measuring precisely the positions and image strengths of tens of thousands of stars on each, has been beyond the capacity of available measuring devices; only a few hundred selected stars on each photograph could be examined. This has severely restricted the research programmes of astronomers. For example, the search for newly-formed stars, which are very heavily obscured by clouds of interstellar dust surrounding them, has been limited to a few very small parts of our Galaxy of stars.

The GALAXY machine was conceived to overcome these limitations, to enable astronomers to make full use of the information they can record at the telescope. The application to astronomy of modern methods of automatic control and data handling has been a feature of the work of the Royal Observatory, Edinburgh under its present Director, Professor H. A. Brück, C.B.E.

## The Measuring Problem

The light from a single star is focused by the telescope to form a spot of light only a few tens of micrometres across. The light is scattered and absorbed by the photographic emulsion; the brighter the star, the further the light spreads out in the emulsion, so that when the photograph is developed (it is of course a negative) the images of bright stars are larger and more dense grey spots than those of faint stars. The measurement of the strength of a star image is consequently a matter of measuring its size and density, sizes typically lying in the range from tens to hundreds of micrometres.

A suitable machine is required to do three things: to find the images of the stars on the photograph, to measure their positions, and to measure their sizes and densities. It has to do these with precision and at high speed.

The requirements laid down for the GALAXY machine were that the precision of measurement should be 1 $\mu$m in the position of a star image and 0·25 $\mu$m in the size, and that the machine should find and measure a thousand star images an hour, entirely automatically.

## The GALAXY Machine and its Method of Operation

The basic conception of GALAXY was due to Dr. P. B. Fellgett (now Professor of Cybernetics and Instrument Physics in the Applied Physics Department at Reading University). Four main features were decided upon: a cathode-ray tube to scan the photograph with a spot of light, for finding the star images and measuring their sizes and densities; a precise mechanical carriage to hold and position the plate with an accuracy better

than 1 $\mu$m; a system developed by Ferranti Limited for measuring the carriage position to 1 $\mu$m; and an electronic system similar to a computer to control the operations.

GALAXY works as follows. To find the star images the photograph is scanned by a small spot of light, produced by a cathode ray tube and projected down to a chosen size, 16 µm across being typical. The light passes through the photograph and is measured by a photoelectric cell. The passage of the spot of light over a star image is then detected by the cell as a reduction in brightness, and the position at which the event occurred is recorded. With this resolution of 16 µm, the plates currently being measured are searched at a rate of 30mm$^2$/min, ten thousand stars being found and recorded per hour.

When the star images have been found, the carriage carrying the photographic plate is moved to put each star in turn beneath a scanning system working at high magnification, for a more detailed examination of each image.

The spot of light is now only 1 µm across, and this is scanned in a spiral pattern over the image. The amount of light passing through and around the image is again measured by a photo-electric cell. If the image is not centred on the spiral pattern, more light passes through one side than through the other, and the carriage is moved until equality is obtained. The position of the carriage is measured, and in this way the position of the image is determined in units of 1 µm. Meanwhile, the measurements of the amounts of light passing through different parts of the image

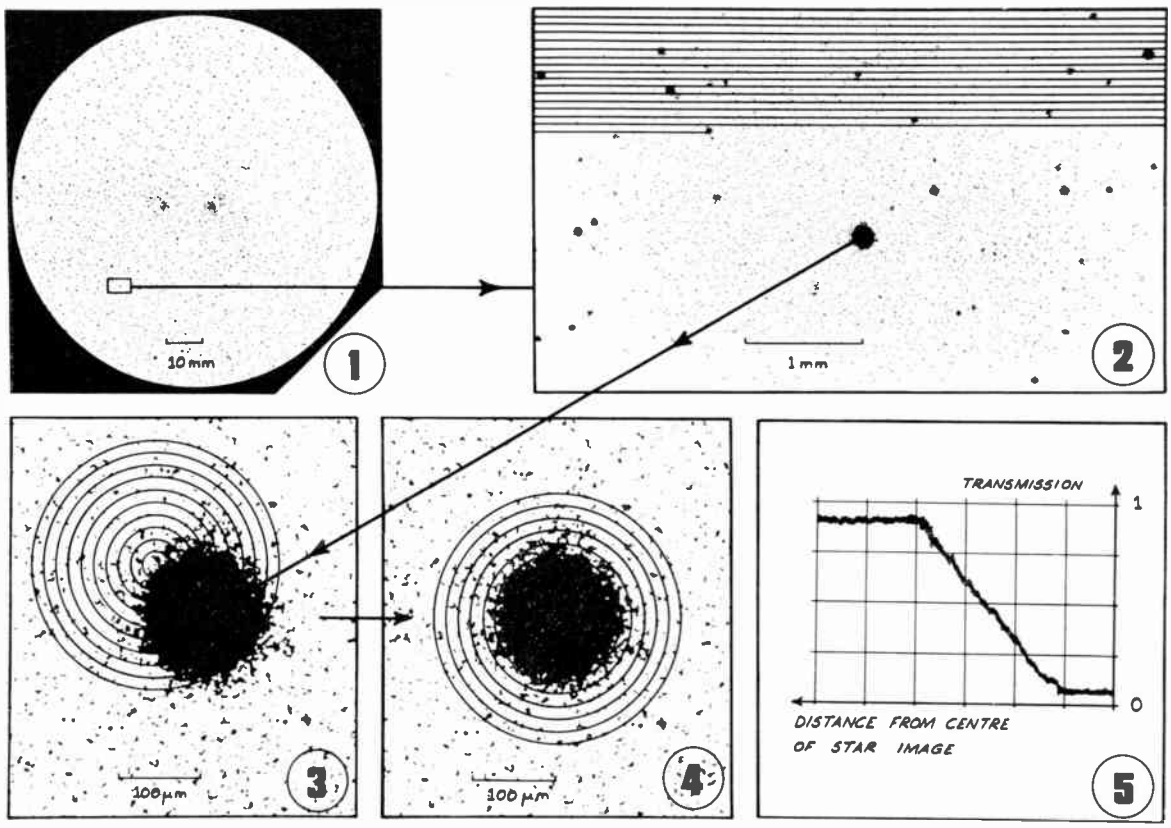


Method of operation of the GALAXY measuring machine at the Royal Observatory, Edinburgh

(1) A typical photograph taken with the Schmidt telescope. The stars have produced black images on the negative. A typical photograph contains 40 000 images. An area of the negative is selected for measurement.

(2) The selected area of the negative enlarged. GALAXY searches the selected area for star images, using linear scanning.

(3) A single star image greatly enlarged. GALAXY scans the star image, using concentric circle scanning.

(4) The same star image; GALAXY centres the star image and measures its position to 1 µm.

(5) Drawing of the oscilloscope display on GALAXY. The profile of the star image is measured with an uncertainty of 0·25 µm.

are being examined by the control system in order to determine the image structure. A measurement of the strength of the image is obtained, in units of 0·25 μm: this measurement is directly related to the brightness of the star photographed. The measurements of position and brightness are coded and output recorded on computer tape, at the rate of a thousand stars an hour, for subsequent analysis in the Observatory's computer.

## Engineering Details

The machine basically is a high accuracy two-dimensional co-ordinate table fitted with means of precise photo-electric examination of star images on a photographic plate. Since accuracies of the order of 1 μm are involved, the construction must be very rigid and hence large and heavy, the overall dimensions of the machine itself being 2·45 m × 1·85 m × 2·15 m high (8 ft × 6 ft × 7 ft) and the weight 3·6 tons. The base is a hollow webbed casting on which is mounted a carriage with compounded X and Y movements on linear ball races with a high degree of linearity and orthogonality. Three V-grooves are mounted on the carriage which locate three ball-ended screws on the plate carrier.

Two cathode-ray tubes of the micro-spot type with their scanning assemblies and optical systems are rigidly mounted to a bridge casting over the carriage, so that the plate can be positioned relative to their optical axes, the resulting variations in light transmission being detected by two photomultipliers mounted below the carriage level.

X and Y movements are measured by two linear glass gratings having 100 lines/mm using the well-established two-phase moiré technique with division of the cycle by ten, giving a basic measuring unit of 1 μm. The actual position of the carriage is given by two six-stage octal counters which are continuously updated by information from the measuring units. Carriage movements are actuated by two hydraulic rams controlled by electro-hydraulic valves, operated by servo amplifiers to which position and velocity feedback are applied.

All electronic circuitry and controls are mounted in two 6 ft high 19 in racks forming a single floor-standing unit. Circuitry is assembled on pluggable printed circuit cards and consists partly of discrete component and partly of microcircuit type.

Operation of the equipment consists of going through an automatic datum setting routine, followed by a *search mode* in which the plate is scanned in columns 8·192 mm wide by the combination of a linear scan on the search cathode-ray tube and mechanical indexing of the carriage in the orthogonal direction. This operation uses the low magnification optical system and gives an output on 8-channel paper tape of the approximate X and Y co-ordinates of images found. Also incorporated in this list of 'finding co-ordinates' are those of a group of reference images which have been preselected and measured, and are repeated every thousand images. This tape is now used as an input for the second operation, namely the *measurement mode*, after carrying out a second automatic datum routine now to refer co-ordinates to the optical axis of the high magnification system. Each pair of co-ordinates is read in turn by a photoelectric tape reader, followed by a digital positioning operation which brings the corresponding image into the field of view of the 256 μm diameter spiral scan. Control of the servos, which has been digital up till this moment, is handed over to the analogue signals derived from the image photomultiplier, causing centring of the image in the field. This is followed by the comparison of the density profile of the image against radius with 1024 standard profiles contained in a core store. The address of the matching profile and the co-ordinates of the image centre to 1 μm uncertainty are output on 8-channel paper tape. This complete operation takes an average 4 seconds per image. This means that the group of reference images are measured every hour, and so the measurements are not dependent on absolute calibration as an off-line computer examination can compensate for long-term drift.

Since the measurement mode optical system requires a short focus microscope objective, means must be provided to maintain focus in spite of variations in photographic emulsion height. This is achieved by mounting the lens system in a stainless steel barrel, centred by an air-bearing, whose weight is relieved by an air-balance system which allows the lens unit to rest on the emulsion surface with a downward thrust of about 3 grammes.

## Progress of the Project and Performance of the Machine

The design and construction of the whole system was entrusted to the Scientific Instrument Control Department of Ferranti Limited at Dalkeith, Midlothian, now Faul Coradi Scotland Limited, Haddington, East Lothian. In September 1965 a detailed design study of the system was begun by the manufacturer together with Dr. V. C. Reddish of the Royal Observatory, Edinburgh, who has been the astronomical consultant throughout, and when this was completed in June 1966 it formed the basis of a contract signed in August of that year. It was then estimated that the whole machine including associated control systems would be completed in three years. The mechanical carriage system was constructed by Sogenique Limited and delivered to Edinburgh in

April 1967, and the cathode-ray scanners were developed by Ferranti Limited, Moston, Manchester.

The various parts of the GALAXY system were connected up and tested together for the first time in March 1969. During the succeeding months a number of minor modifications have been made but the design as a whole has proved to be satisfactory. The machine was put through a series of increasingly demanding tests and by the end of June it had become apparent that its performance was exceeding expectations. Positions were being measured with a precision of 0·5 μm, better by a factor of two than that demanded by the specification, and image sizes were measured with a precision 20% better than specified. Intensive trials of the machine in the following three months showed that this performance was maintained, and the machine was formally accepted in October. It was immediately put to measuring photographs taken as part of one of the Observatory's programmes —the search for newly-formed stars almost hidden by dense obscuring clouds of interstellar dust. By the end of the year, colours and brightnesses of about forty thousand stars had been obtained from measurements of more than a quarter of a million star images. The Observatory's astronomers now face a major task in programming the computer to deal with the output of the GALAXY machine.

### Postscript

Since the machine was first switched on last March it has been run for more than two thousand hours, with no major breakdown and a negligible amount of time lost through minor faults.

# FORTHCOMING CONFERENCES

### Conference on Trunk Telecommunications by Guided Waves

The conference on trunk telecommunications by guided waves which was to have been held at the Institution of Electrical Engineers, Savoy Place, London, W.C.2, in September 1969, and was postponed, will now be held from Tuesday, 29th September to Friday, 2nd October 1970.

The aim of the conference is to survey and to assess current achievements, problems and prospects in the development of trunk telecommunications systems by guided waves at millimetric and optical frequencies. Special attention will be paid to:

systems aspects, modulation and multiplexing techniques
guiding structures, transmission imperfections
installation and fabrication
terminal and repeater equipment
measurement techniques
components.

Offers of contributions to the conference programme are invited. Intending contributors should submit a 250 word synopsis of their paper to the I.E.E. Conference Department without delay; full (2000 word) manuscripts will be required by 1st June 1970.

The conference is being organized by the I.E.E. in association with the I.E.R.E. and the Institute of Electrical & Electronics Engineers. Further details will be available in due course from the Manager, Conference Department, I.E.E., Savoy Place, London, W.C.2.

### Radiological Protection Problems

The Commission of the European Communities, in collaboration with the Centre of Atomic and Nuclear Physics of the Faculty of Science of the University of Toulouse, is organizing an international symposium to be held from 3rd–6th November 1970 at Toulouse, France, on 'Radiological Protection Problems associated with Parasitic X-ray Emission from Electronic Products'.

The aim of the symposium is to enable electronics engineers, technical inspection bodies, public-health and occupational-safety authorities to carry out exchanges of views and experience. Electronic products to be considered include rectifying valves, transmitting valves, thyratrons, klystrons, magnetrons, electron microscopes and television receivers and the provisional scope covers the following:

possible sources of parasitic X-rays, and experimental results;
methods of measuring soft X-ray emission;
biological aspects of exposure to soft X-rays;
means of reducing parasitic X-ray emission;
performance standards, testing and inspection methods for electronic products.

Offers of papers and requests for registration forms and further information may be obtained from:

Mr. E. A. Hampe, Commission of the European Communities, Directorate-General for Social Affairs, Directorate for Health and Safety, 29 rue Aldringer, Luxembourg (G.D. of Luxembourg).

U.D.C. 535.374:621.373

# A Sealed-off Beryllia Tube Argon Ion Laser

*By*

**P. C. CONDER**†

and

**H. FOSTER**†

*Reprinted from the Proceedings of the I.E.R.E. Conference on 'Lasers and Opto-Electronics' held at the University of Southampton on 25th to 28th March 1969.*

An argon ion laser is described in which the discharge is confined by a beryllia capillary tube. This has enabled the current density in the discharge to be increased to more than 600 A $cm^{-2}$ with negligible gas clean-up. Sealed-off lasers have been life tested for more than 1000 hours without the need for a gas replenishing system and have shown less than 10% change in output. The total output of 1·5 W can be increased to more than 3 W by the application of a magnetic field. This performance is obtained from a 3 mm bore, 30 cm long plasma tube with an argon pressure of 0·7 torr.

## 1. Introduction

The rare gas ion lasers which were first discovered as pulsed systems now produce more c.w. power and the widest choice of wavelengths of any class of laser operating in the visible wavelength range. From the several hundred wavelengths reported[1] the highest powers are obtained from transitions between the excited states of the argon ion.

The essential parts of a basic argon laser are as shown in Fig. 1. The high current density needed to achieve high power operation is obtained by concentrating a d.c. discharge in a narrow bore water cooled tube. A by-pass tube between the cathode and anode regions prevents build-up of gas pressure at one end. An axial magnetic field is sometimes used to increase the laser output. In the early designs of argon ion laser the discharge tube has usually been of silica.

## 2. Power and Life Limitations

Saturated output of the argon laser is not achieved in a sealed-off device and the maximum powers obtainable are limited by the technology of the gas discharge tube. As the current through the laser is increased beyond the threshold for laser action the output power rises quadratically with current since both electron density and ion ground state density are proportional to the current. Discharge current densities of several hundred A $cm^{-2}$ at gas pressure of a few tenths of a torr are required to be confined in a 2 to 3 mm bore capillary. More than 80% of the input power is dissipated in the discharge tube, corresponding to 200 W per cm length of the capillary. These severe operating conditions can cause serious damage to the plasma confinement structure and to achieve a reasonable working life, strict limits have been imposed on the input drive power. These limits are set by sputtering, disintegration and overheating of the plasma confinement structure, gas clean-up and cathode poisoning.

The silica used in the conventional argon lasers has excellent thermal shock resistance but its low thermal conductivity results in a very high inside wall temperature. Gas clean-up into the hot silica leads to a rapid fall in the argon pressure with resulting deterioration of performance. The clean-up problem has been overcome to a limited extent by the provision of a gas-replenishing system. The life of a silica tube laser has been mainly determined by erosion of the tube by ion bombardment and subsequent breakage.

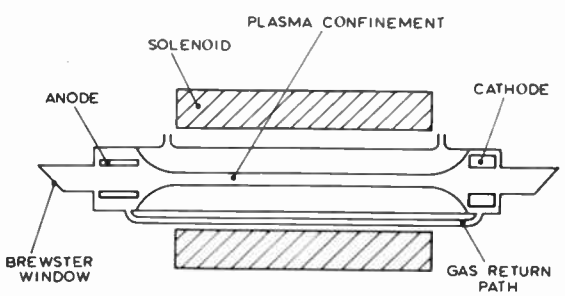


Fig. 1. Components of a d.c. ion laser.

Alternative methods of confining the discharge by the use of segmented metal or graphite structures have been used but a gas replenishing system has been necessary to obtain a useful life.[2]

## 3. Choice of Beryllia

The properties of the discharge tube materials previously used are responsible for some of the argon laser problems. A survey of materials with some suitable properties reveals that choice is limited by the availability of very straight small bore tubes and the ability to make joints consistent with high vacuum

† Services Electronics Research Laboratory, Baldock, Herts.

**Table 1.** Properties of some discharge tube materials

| Material | Thermal conductivity cal/cm.s degC | Thermal expansion deg $C^{-1}$(0–100°C) | Thermal shock $cal.s^{-1}\ cm^{-1}$ | Melting point °C | Electrical resistivity ohm.cm |
|---|---|---|---|---|---|
| Silica | 0·0035 | $0{\cdot}55\times10^{-6}$ | 13·0 | ~1600 | $>10^{13}$ |
| Alumina | 0·054 | $6{\cdot}9\times10^{-6}$ | 1·5 | ~2100 | $>10^{13}$ |
| Boron Nitride | 0·023 to 0·145 | 0 to $2{\cdot}3\times10^{-6}$ | | ~2800 | $1{\cdot}2\times10^{12}$ |
| Beryllia | 0·525 | $5{\cdot}4\times10^{-6}$ | 11·7 | 2573 | $>10^{13}$ |
| Graphite | 0·3 | $3{\cdot}6\times10^{-6}$ | 310 | ~3500 | $3\times10^{-6}$ |
| Vitreous Carbon | 0·01 to 0·02 | $2{\cdot}0\times10^{-6}$ | | | 1 to $5\times10^{-6}$ |
| Molybdenum | 0·346 | $4{\cdot}9\times10^{-6}$ | | 2622 | $5{\cdot}7\times10^{-6}$ |
| Tungsten | 0·476 | $4{\cdot}45\times10^{-6}$ | | 3382 | $5{\cdot}3\times10^{-6}$ |
| Copper | 0·92 | $16{\cdot}4\times10^{-6}$ | | 1083 | $1{\cdot}5\times10^{-6}$ |
| Aluminium | 0·57 | $23{\cdot}5\times10^{-6}$ | | 660 | $2{\cdot}6\times10^{-6}$ |

technology. These materials with some relevant properties are listed in Table 1. Some metals are included but are not considered suitable because of their high sputtering rates.

Of the insulating materials beryllia is unique with a high thermal conductivity and good thermal shock resistance. Discharge tube experiments confirmed its suitability provided that the technology problems could be overcome and that no toxic hazard would arise following ion bombardment.

### 3.1 *Toxic Considerations*

The toxicity of beryllia is associated with dust or fine particles which can be inhaled. Precautions are necessary to prevent concentration exceeding the recommended limits.[3] Clean, fired beryllia components present no toxic problems. A beryllia discharge tube could be a source of fine particles if beryllia were eroded by ion bombardment in a similar way to silica in the early ion lasers. An accumulation of particles in the laser and in the vacuum processing system could then lead to contamination levels exceeding the recommended limits.

Chemical or spectroscopic tests for contamination levels can readily be carried out at several stages in the construction and operation of beryllia discharge tubes. Such tests have shown safe levels at all times though strict cleaning procedures at some stages are necessary to prevent an accumulation of contamination. Tests on discharge tubes which have been life tested have also shown safe levels, indicating that erosion of beryllia by the discharge is not significant.

### 3.2 *Thermal and Mechanical Considerations*

Due to superior thermal conductivity of beryllia, it becomes possible to use a thicker wall tube than with silica while maintaining a lower internal wall temperature. The larger external surface area to the tube which results from this, permits the removal of a greater heat load. A limit to the wall thickness is reached when the stresses due to temperature difference become too high and a compromise has to be be made.

The inner surface temperature of the beryllia tube can be calculated from

$$K = \frac{\mathrm{d}Q}{\mathrm{d}t}\,\frac{\log_e(r_2/r_1)}{2\pi(T_1 - T_2)}$$

where

$K$ = thermal conductivity.
$\frac{\mathrm{d}Q}{\mathrm{d}t}$ = power per unit length.
$r_1, r_2$ = inner and outer radius of tube.
$T_1, T_2$ = inner and outer wall temperature.

Taking values of

$K$ = 1·88 W/cm degC (100°C)
$\frac{\mathrm{d}Q}{\mathrm{d}t}$ = 180 W/cm (at 40 A discharge current).
$T_2$ = 373°K
$r_2$ = 0·35 cm
$r_1$ = 0·15 cm

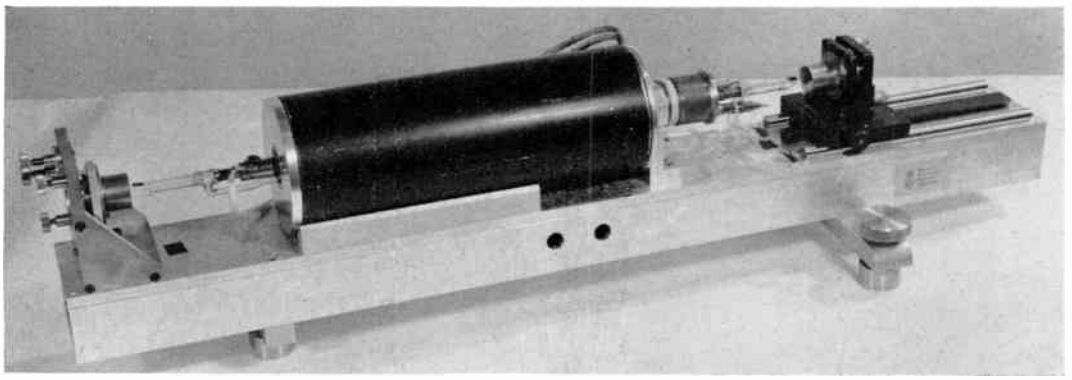

Fig. 2. Beryllia tube laser.

from which the inner surface temperature $T_1 = 386°K$.

A similar calculation for a typical silica tube laser dissipating 80 W/cm at 20 A gives an inner surface temperature of 900°K.

The inner surface temperature of the silica tube determines the maximum safe continuous operating level. This limitation is removed by the use of beryllia and the power input to the discharge may be raised until limited by boiling of the cooling water.

### 3.3 *Vacuum Technology of Beryllia*

Beryllia can be used for vacuum device construction if ceramic metallizing and high temperature soldering techniques are reliable. The vacuum joints have to be carefully designed and tested to withstand subsequent temperature cycling. In order to provide a surface for soldering, the beryllia is first metallized and then nickel plated. Differences in thermal expansion between the beryllia, metal and solder can lead to failure of the joint if excessive stresses are created and this can be avoided by the choice of suitable materials. These considerations of the use of beryllia have led to the present design.

## 4. General Requirements for a Sealed-Off Device

In addition to the beryllia design considerations outlined above, a number of other restrictions are placed on the choice of tube components and method of fabrication. In order that the low pressure of spectrally pure argon gas within the device should not become contaminated, stringent standards of high vacuum technology have been employed. All materials, brazed or welded joints and tube components are of low vapour pressure and have been designed to withstand the usual rigorous vacuum tube processing and cathode activation.

## 5. The Beryllia Laser

In this design of argon laser (Fig. 2) the gas discharge is laterally confined by a straight small bore beryllia tube. The d.c. discharge is maintained between an anode and a concentrically mounted impregnated cathode of sufficient area to provide 40 A emission. The ends of the laser are terminated by Brewster-angle windows of optically flat Spectrosil.

A gas return path is provided by a glass tube which connects the cathode housing to the outer end of the anode. This is necessary to reduce the pressure difference which would be created due to gas pumping[4] during operation of the high current discharge. The tube is external to the main discharge and returns within the bore of the solenoid. Since the solenoid will not withstand the elevated temperature used during vacuum processing the design permits the solenoid to be fitted to the discharge tube after seal-off.

The discharge tube, anode, cathode housing and magnet are cooled by a 3 gallons/min (13·5 l/min) flow of recirculated de-ionized water and a heat exchanger of 8 kW capacity transfers the heat to mains cooling water. The use of de-ionized water prevents short circuit of the discharge when high starting voltages are applied to the tube and avoids the build-up of scale which would create a thermal barrier between the beryllia tube and the cooling water.

## 6. Magnet Design

The application of a magnetic field to an argon ion laser can produce an increase in output and efficiency.[5] The gain of the laser depends on the charged particle density and this is increased with the application of an axial magnetic field. The laser output enhancement obtained varies with the strength of the magnetic field and with the other variable parameters of the laser.

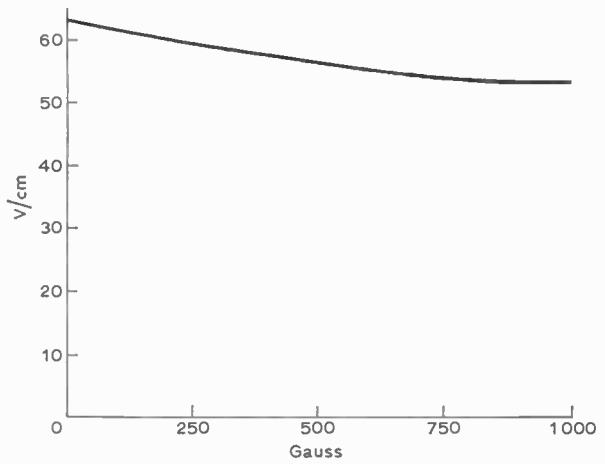


Fig. 3. The effect of magnetic field on discharge voltage gradient.

Another effect of the magnetic field is a reduction in the axial voltage gradient in the discharge at a fixed current, as shown in Fig. 3. The power input to the discharge for a fixed current is thus reduced, giving an increase in efficiency.

Consistent with the compact beryllia tube laser design, a magnet of minimum size and weight to provide a uniform axial magnetic field of 1000 gauss was designed. The solenoid winding is 1200 turns of aluminium foil 0·012 mm thick and coated with 0·005 mm epoxy insulation. The completed magnet is 10·16 cm (4 in) diameter, 31·75 cm (12·5 in) long, weighs 4·32 kg (9½ lb) and incorporates water cooling on internal and external surfaces. The 3·16 cm (1¼ in) diameter bore of the solenoid locates and supports the laser and the gas by-pass tube.

## 7. Power Supply

The voltage-current characteristic of the beryllia discharge tube is shown in Fig. 4. A high direct voltage is required to initiate the discharge and as a small current is passed through the gas the maintaining voltage falls. The discharge now behaves as a low negative resistance as the current is increased. A load resistance is in circuit in this range to maintain control of the discharge current. Above about 10 amperes the tube becomes a positive resistance and the load is shorted out. A well-stabilized constant current supply is necessary.

The power supply for the beryllia tube laser comprises a starting circuit capable of 1000 V, ½ A, followed by a main power unit delivering 350 V, 40 A, with current control and incorporating an automatically controlled load resistor. Magnet and cathode heater supplies are incorporated in the same unit and to prevent damage to the laser a controlled starting procedure is necessary. This is achieved by an interlock system which prevents initiation of the discharge until high current operating conditions are satisfied.

## 8. Performance

A number of lasers constructed in the manner described have been built and tested. The extent of the improvements made possible by the use of beryllia instead of silica may be seen by reference to Table 2.

**Table 2.**

Comparison of silica and beryllia tube laser

| | Silica | Beryllia |
|---|---|---|
| Total output power (without magnet) | 0·5 W | >1 W |
| Total output power (with magnet) | 1·0 W | >3 W |
| Overall efficiency | 0·016% | 0·056% |
| Life | 150 hours | >1000 hours |
| Gas clean-up rate | 20 μm l/hour | 0·12 μm l/hour |
| Gas replenishing frequency | 8 hours | nil |
| Gas pressure | 0·2 torr | 0·7 torr |
| Active discharge length | 60 cm | 30 cm |
| Discharge tube internal diameter | 3 mm | 3 mm |
| Discharge tube external diameter | 5 mm | 7 mm |
| Discharge current | 20 A | 40 A |
| Tube voltage | 265 V | 165 V |
| Power input per cm length | 80 W | 180 W |
| Axial magnetic field | 1000 gauss | 1000 gauss |

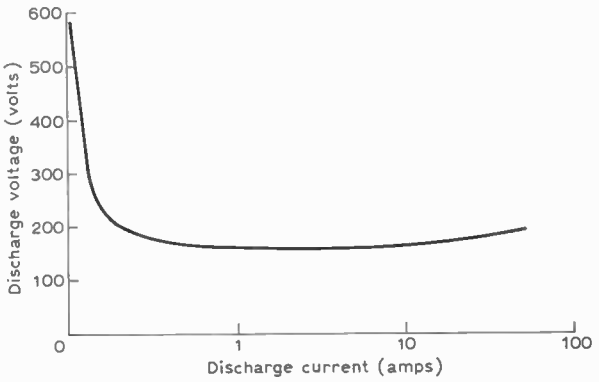


Fig. 4. The voltage/current characteristic.

A typical output characteristic of the beryllia tube laser is shown in Fig. 5. The total output power is plotted as a function of discharge current at various magnetic fields.

The results shown are for multi-mode, multi-wavelength output. The optical cavity consisted of a 3 metre radius of curvature low transmission mirror and a flat 8% transmission mirror at a separation of 65 cm. Uniphase output at slightly reduced power can be obtained by the use of a longer radius of curvature mirror. Single wavelength operation can be obtained by the usual methods, such as the insertion of a suitable dispersion prism within the optical cavity. Table 3 shows the total range of wavelengths available from this design of laser. Approximately 40% of the total output power is available at either of the principal wavelengths of 488 nm (4880 Å) or 514·5 nm (5145 Å).

**Table 3.**
Laser output with selected mirror transmissions

| Wavelength Å | Mirror Transmission % | Laser Output mW |
|---|---|---|
| 5287 | 1 | 45 |
| 5145 | 7 | 1300 |
| 5017 | 4 | 140 |
| 4965 | 3 | 420 |
| 4880 | 5 | 1300 |
| 4765 | 4 | 600 |
| 4727 | 6 | 225 |
| 4658 | 1 | 10 |
| 4579 | 3 | 140 |

To obtain optimum performance at any other wavelength it is necessary to use lower transmission mirrors to compensate for the lower gain for these transitions.

As seen in Table 2 the efficiency of the beryllia laser is more than three times that of a silica tube laser. This is because of the higher current in the discharge. Reference to the discharge $V/I$ characteristic in Fig. 4 shows that with increasing current through the discharge the power input is almost linear. The output power rises quadratically with increasing discharge current and therefore a higher current leads to an increase in efficiency.

The significant features of the performance of the beryllia tube laser from the data in Table 2 are the

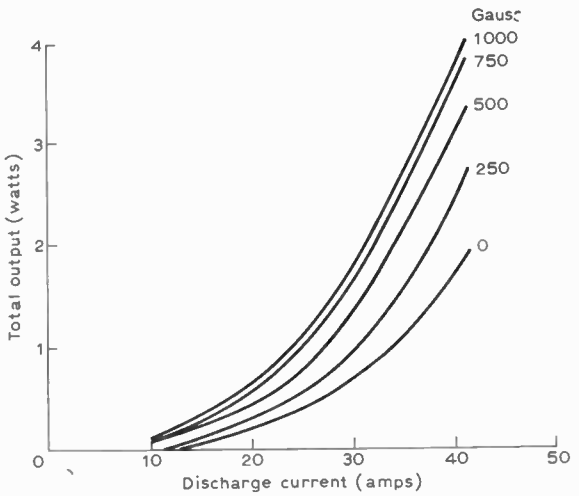


**Fig. 5.** Laser output as a function of discharge current at different magnetic fields.

low gas clean-up rate, the high optimum gas pressure and the long life at high output power. Life tests on two lasers were obtained by day and night operation with frequent switching off and re-starting to simulate a laser in use. After 1000 hours when the test was terminated the output power had fallen by less than 10%.

The gas pressure in the laser was monitored by a Pirani gauge in a half-litre gas ballast volume attached to the laser, and the variation of argon gas pressure during the life of beryllia and silica tube lasers is shown in Fig. 6. It will be apparent that the very low gas clean-up rate makes a gas replenishing system unnecessary for a beryllia tube laser.

The higher optimum gas pressure may be explained by the cooler internal surface temperature of a beryllia discharge tube (Sect. 3.2). The gas temperature in the region of the walls is influenced by the temperature of the tube wall.

The gas density $\rho_g$ in the discharge is given by

$$\rho_g = \frac{T_w \rho_w}{T_g}$$

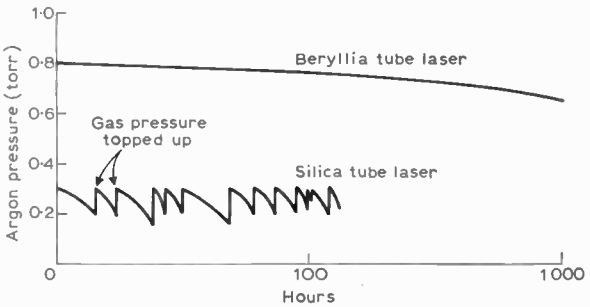


**Fig. 6.** Variation of argon gas pressure during laser life.

where $\rho_w$ = gas density near the wall
$T_w$ = gas temperature near the wall
$T_g$ = gas temperature in the discharge.

Thus the lower the wall temperature the lower will be the gas density in the discharge. Argon laser gain is proportional to the product of tube radius and normalized gas density[1], hence the beryllia tube laser requires a higher initial cold filling pressure.

It will be seen that the use of higher gas pressures results in a shorter mean free path in the gas and leads to a reduction in the gas clean-up rate. In the region of the discharge near the wall, the mean frec path is given by

$$\lambda_w = \frac{\lambda T_w P}{T_0 P_w}$$

where $\lambda = 6{\cdot}32 \times 10^{-8}$ at n.t.p.
$T_0 = 273°K$
$P = 760$ torr
$P_w$ = pressure near wall
(cold-fill pressure = 0·7 torr)

This gives the value of $\lambda_w$ as approximately 0·1 mm which is a factor of ten shorter than for a typical silica tube confined plasma.

The shorter mean free path in the gas can be expected to reduce or prevent erosion of the beryllia by the discharge. Results of the tests for beryllia powder contamination as described in Sect. 3.1 indicate that a beryllia tube is not eroded by the discharge under the conditions used for the life test.

## 9. Discussion

The encouraging performance and life test results of sealed-off beryllia tube lasers leads to a consideration of extensions to the design described.

A change of any one parameter of the laser requires adjustment of the other variable parameters to achieve optimum performance, and scaling laws require experimental confirmation. The gas pressure, discharge current, magnetic field strength and tube diameter and length are all inter-related and modify the gain of the laser, so that re-optimization of the output is therefore necessary.

A higher output power per unit length could be obtained by further increasing the current density in the plasma. With no power supply limitations the current can be increased to the point where boiling of the cooling water takes place on the outside surface of the beryllia. A well optimized design for maximum heat extraction[6] might allow a current of up to 100 A to be used but other limitations would arise at lower currents. A cathode capable of this emission would require some development but a more serious limitation would be set by damage to mirrors and Brewster windows at an estimated laser output of 15 W. Damage to some optical components has been observed at the 5–10 W level. A more fundamental limit would be reached at current densities above 1000 A cm$^{-2}$, where resonance radiation trapping can occur between the lower laser levels and the ion ground state leading to a destruction of the population inversion.

Another approach to attain a higher output power would be to increase the tube diameter and length whilst maintaining the same current density and thus provide a larger volume of excited gas. A larger tube diameter would also reduce the laser power density which should then extend the operating range before the mirror damage threshold is reached. A longer discharge tube would require a higher starting voltage and a reasonable estimate would be to increase the length of the present compact design by a factor of 2 thus doubling the laser output for the same current. The gas pumping problem would be accentuated in a long tube. Careful re-design of the by-pass tube would be necessary to maintain the optimum pressure in the plasma and to prevent a discharge breakdown in the by-pass tube at the higher starting voltage required.

The features of a beryllia discharge tube could be exploited in another way by a further reduction in size of the present compact design. For example, if the plasma tube were reduced from 30 cm to 10 cm giving an overall laser length of about 30 cm, a total output of a few hundred milliwatts could be expected.

## 10. Conclusion

The argon laser described is made possible by overcoming the technological problems encountered in the use of beryllia for a sealed-off discharge tube. The improved performance of the laser is due to the properties of beryllia. Long life and low gas clean-up features are obtained when good standards of high vacuum technology are maintained and when cathode emission is adequate throughout life.

Evidence that a toxic hazard does not arise when beryllia is used under the conditions described has established confidence in its use and further exploitation of its properties as a plasma confinement material is possible.

A practical sealed-off argon ion laser with a long life will improve the usefulness and the reliability of the device and make it a more successful competitor for visible laser applications. Although the efficiency of the laser is comparable with other visible lasers, to obtain the output powers quoted a large and expensive power supply is required. However, the cost per watt-hour of laser output will be comparable. Sealed-off ion lasers using other gases have similar problems to those of the early argon ion lasers. It is likely that the beryllia discharge tube design will provide a

similar improvement for these lasers to that obtained for argon. Devices other than lasers which use a low pressure gas discharge may also benefit from the low gas clean-up and high dissipation properties of beryllia.

## 11. Acknowledgments

The authors would like to acknowledge the invaluable technical contributions of their colleagues at the Laboratory.

The paper is published by permission of the Ministry of Defence.

## 12. References

1. Bridges, W. B. and Chester, A. N., 'Spectroscopy of ion lasers', *I.E.E.E. J. Quantum Electronics*, **QE-1**, pp. 66–84, May 1965.
2. Hernqvist, K. G. and Fendley, J. R., 'Construction of long life argon lasers', *I.E.E.E. J. Quantum Electronics*, **QE-3**, No. 2, pp. 66–72, February 1967.
3. Ferreira, L. E., 'Recommended Practices for Safe Handling of Beryllium Oxide Ceramics', Symposium on Materials and Electron Device Processing, S.T.P. No. 300, American Soc. for Testing and Materials, 1961.
4. Gordon, E. I. and Labuda, E. F., 'Gas pumping in continuously operated ion lasers', *Bell Syst. Tech. J.*, **43**, No. 4, pp. 1827–9, July 1964.
5. Labuda, E. F., Gordon, E. I. and Miller, R. C., 'Continuous-duty argon ion lasers', *I.E.E.E. J. Quantum Electronics*, **QE-1**, No. 6, pp. 273–9, September 1965.
6. Brauer, H., 'Heat Transfer in Annular Clearances with Forced Convection and Local Boiling'. (Translation) TRG Information Series 343 (R), (H.M. Stationery Office, London, 1964).

*Manuscript received by the Institution on 25th March 1969. (Paper No. 1302/CC64)*



# Computer Control of Motorway Signals

More than 800 miles of motorways in England and Wales are to be equipped with motorway signals linked to a network of ten on-line computers made by GEC-Elliott Traffic Automation Ltd. The company is supplying ten MARCH 9050 on-line computers, communications links, standard programs and special modular applications software. Altogether the orders cover the provision of five computer centres, and 12 motorway control offices.

Computer centres will be located at Scratchwood, Hook, Perry Barr, Almondsbury and Westhoughton. The separate control offices, which are to be manned by traffic police operators, will be at Preston, Chester, Winchester, Guildford, Almondsbury, Devizes, Kidlington, Cwmbran, Scratchwood, Welwyn, Perry Barr, and Warwick. Each computer centre will house the two MARCH 9050 computers working in parallel together with MARCH input and output channels providing facilities for controlling motorway signals and communications links with the control offices, as well as automatic telex and data links.

Video data terminals, emergency telephone panels and display diagrams will be linked to a local computer centre. Using the alpha-numeric keyboard on the video data display, the police operators at each control office will set up any or all of the signals to display warnings of hazards, instruct traffic to slow down or stop, and advise of lane changes and obstructions. Information displayed on the motorways is also shown on the video data terminals, enabling operators to check the operation of the motorways signals.

Basically the Elliott ARCH 9050 central processor each MARCH 9050 has a 16k core store. Two computers, linked via a standard MARCH interface, are to be located in each computer centre. Normally input data are fed to both computers, but only one machine will be the control computer. Self-checking programs are to run continuously and, if at any time a computer fails a test, executive control of the real-time situation is automatically switched to the other computer and details of the fail condition are passed immediately to to the nearest maintenance unit.

One of the most significant features of the GEC-Elliott Traffic Automation on-line computer systems is that all hardware and software is designed to modular standards. For example, the central processors, data links, inputs/outputs and other items of the systems hardware are developed from readily available, compatible units in current production.

On the software covering standard programs and special applications a fully modular approach will be used, making it especially simple in future orders for U.K. and world markets to adapt the programs to suit special applications and differing legal requirements in traffic control situations. In addition to the standard MARCH 9050 supervisory program, GEC-Elliott Automation are supplying module packages for operation of the central processor, control office, traffic control and weather surveillance. Programs for data transmission and test facilities will incorporate the possibility of full remote access for future program development and off-line processing of data.

# Contributors to the *Journal*

**A. Ponder** obtained the B.Sc degree of London University in general science while at the University College of Leicester and he subsequently studied electronics subjects at Borough Polytechnic and the West Ham College of Technology. Following his national service in the Royal Signals, he worked in the development laboratories of the Brimar Valve Division of Standard Telephones and Cables Ltd., and of Elliott Nucleonics Ltd. for several years. He then joined the Advanced Development Laboratory of Associated Electrical Industries (Woolwich) Ltd., where he remained for over eight years, until he became redundant as a result of the A.E.I.–G.E.C. merger. He is at present a consultant.

**Professor J. E. Flood** graduated from Queen Mary College, University of London. After war-time service at the Admiralty Signal Establishment, Haslemere, he worked on the development of line transmission systems with Standard Telephones and Cables, Ltd., and research on electronic telephone exchanges at the Post Office Research Station. In 1953 he joined Siemens Brothers, Ltd. Later this company became part of Associated Electrical Industries, Ltd., and he became chief engineer of the Advanced Development Laboratories of the Telecommunications Division. He was appointed Professor of Electrical Engineering at the University of Aston in Birmingham in 1965, and is now Head of the Electrical Engineering Department.

**Dr. K. C. Kao** received his degrees of B.Sc.(Eng.) and Ph.D. from London University. He is a principal research engineer at Standard Telecommunication Laboratories Limited, heading a team engaged in research into optical communication systems. He holds an honorary Senior Research Fellowship at Queen Mary College, London. Dr. Kao is a Member of the Institution of Electrical Engineers and represented that Institution on the Organizing Committee for the I.E.R.E. Conference on Lasers and Opto-Electronics in 1969.

**T. W. Davies** graduated in physics from the University of Leeds in 1966 and spent a period on postgraduate work in quantum electronics at the University of Southampton. He is now a research engineer in the optical communication systems group at Standard Telecommunication Laboratories.

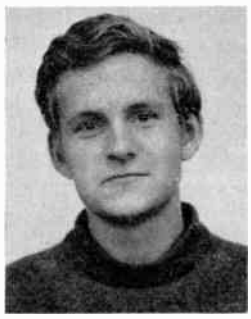

**R. Worthington** received a B.Sc.(Special) degree in Physics at University College, London, and is now a research engineer at Standard Telecommunication Laboratories working in the optical communications system group.

**Douglas Lewin** has been a lecturer in digital systems in the Department of Electronics at Southampton University since 1967. His previous appointment was lecturer in computer engineering at Brunel University (1962-67) and before that he was a digital systems engineer at the Marconi Research Laboratories (1959-52). He studied physics at Northampton Polytechnic (now City University) and systems engineering at the University of Surrey where he obtained his M.Sc. degree. Mr. Lewin is currently engaged in research in the field of computer science, particularly the computer-aided design of digital systems and symbol processing machines. He is author of a recent book on 'Logical Design of Switching Circuits'.

U.D.C. 535.3

# Coherent Light Scattering Measurements on Single and Cladded Optical Glass Fibres

*By*

**K. C. KAO,**
B.Sc., Ph.D., C.Eng., M.I.E.E.†

**T. W. DAVIES,** B.Sc.†

**R. WORTHINGTON,** B.Sc.†

*Reprinted from the Proceedings of the I.E.R.E. Conference on 'Lasers and Opto-Electronics' held at the University of Southampton on 25th to 28th March 1969.*

This paper considers the scattering, at normal incidence, of a laser beam by single and cladded optical glass fibres with a view to estimating their radii and refractive indices. For parallel and perpendicular polarizations of the incident light, the scattered intensity was calculated using the wave theory. The scattering pattern from a single fibre was also calculated by geometrical optics. The light scattered by a cladded fibre in air was photographed for fibres of three different overall diameters. A similar experiment was conducted for the fibre immersed in a liquid having a refractive index near to that of the cladding. Matching was achieved by thermal means.

In both cases considered, the experimental results were found to be in agreement with theoretical results. For a cladded fibre in air, information about the core could not be obtained but a measurement of the angular fringe spacings and positions enabled the cladding diameter and index to be calculated. For a cladded fibre immersed in an index matching liquid, it was found that a measurement of the angular positions of minimum intensity enabled the core diameter to be calculated.

## List of Principal Symbols

| | |
|---|---|
| $a,b$ | radius of core and outer radius of cladding respectively. |
| $\lambda,\lambda_0$ | wavelength of incident radiation in a medium, in vacuum |
| $x = 2\pi a/\lambda_0$ | size parameter of cylinder of radius $a$. |
| $p$ | central ray phase shift $= 2x\lvert M-1\rvert$. |
| $m_2,m_1,m_0$ | refractive indices of core, cladding and air respectively. |
| $M = m_2/m_1$ | relative index. |
| $J_n$ | Bessel function of the first kind. |
| $H_n^{(2)}$ | Hankel function of the second kind. |
| $T_1$ | angular amplitude function of scattered radiation: Case I, $\mathbf{E} \parallel$ to fibre axis. |
| $T_2$ | angular amplitude function of scattered radiation: Case II, $\mathbf{E} \perp$ to fibre axis. |
| $I_1$ | angular intensity function of scattered radiation: Case I, $\mathbf{E} \parallel$ to fibre axis. |
| $I_2$ | angular intensity function of scattered radiation: Case II, $\mathbf{E} \perp$ to fibre axis. |

## 1. Introduction

Recently reported experiments[1,2] have shown that angular scattering measurements provide a very accurate means of determining the radius and refractive index of submicron glass and silica fibres.

This paper considers further the value of making light scattering measurements using coherent radiation on single and cladded optical glass fibres with a view to estimating their radii and refractive indices. The determination of these parameters is particularly difficult in the case of optical waveguide fibres, which are characterized by a very small core radius and only a small difference between the core and cladding refractive indices (Fig. 1)

## 2. Rigorous Solution of Maxwell's Equations for Concentric Cylinders

The problem of an infinitely-long single circular cylinder has been treated by Lord Rayleigh[3] for the case of a plane wave at normal incidence and by Wait[4] for the case of oblique incidence. The solutions in these treatments are general for all sizes and refractive indices. Van de Hulst[5] also deals with scattering by a single cylinder. The theory has been extended to cover the case of a cylinder and concentric sheath at normal incidence[6] and at oblique incidence.[7]

The concentric cylinder problem amounts to solving Maxwell's equations with two sets of boundary conditions. The method is to separate the vector wave equation in curvilinear coordinates which have been chosen in such a way that the surface of the cylinder coincides with one of the coordinate surfaces. The field outside the cylinder can be represented by an infinite series of trigonometric functions and Bessel functions of integer orders. The series converge slowly for large values of $x$, but this difficulty has been overcome by using Debye's[8] asymptotic representation of

† Standard Telecommunication Laboratories Ltd., Harlow, Essex.

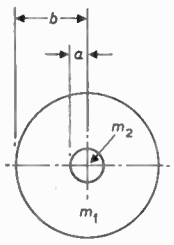


| Parameters | Typical values |
|---|---|
| Core radius ($a$) | 2μm |
| Core refractive index ($m_2$) | 1·52 |
| Overall radius ($b$) | 50μm |
| Cladding refractive index ($m_1$) | 1·50 |

**Fig. 1.** Cross-section of dielectric fibre waveguide (not to scale).

the Bessel functions. Figure 2 shows the configuration for the case of a normally incident plane wave scattered by a cylinder and concentric sheath. The rectangular and cylindrical polar coordinates are depicted and the refractive indices $m_0$, $m_1$, $m_2$ apply to the regions shown. Any plane polarized incident wave can be resolved into the horizontally and perpendicularly polarized components shown in the diagram.

The following analysis of the scattering problem is based on the treatments given by Van de Hulst,[9] Lind and Greenberg,[10] and Kerker and Matijevic.[6]

The incident plane wave travelling (in vacuum) in the $x$-direction is represented by

$$u_0 = \exp[-j\omega t] \sum_{n=-\infty}^{\infty} (-j)^n J_n(kr) \exp[jn\theta]$$

This is the form of the scalar wave in cylindrical coordinates.

For the wave inside the cylinder, the radial component is the Bessel function of the first kind $J_n(m_2kr)$ to maintain regularity at $r = 0$.

For the scattered wave, we use the Hankel function of the second kind $H^{(2)}(kr)$ to obtain the condition of finiteness at infinity.

The field outside the cylinder is due to the superposition of the incident and scattered waves.

Case I, (E ∥ to axis):

$$(r > b) \qquad u = \sum_{n=-\infty}^{\infty} F_n[J_n(m_0kr) - b_n^0 H_n^{(2)}(m_0kr)]$$

$$(b > r > a) \; u = \sum_{n=-\infty}^{\infty} F_n[B_n^1 J(m_1kr) - b_n^1 H_n^{(2)}(m_1kr)]$$

$$(r < a) \qquad u = \sum_{n=-\infty}^{\infty} F_n B_n^2 J_n(m_2kr)$$

Case II, (E ⊥ to axis):

$$(r > b) \qquad v = \sum_{n=-\infty}^{\infty} F_n[J_n(m_0kr) - a_n^0 H_n^{(2)}(m_0kr)]$$

$$(b > r > a) \; v = \sum_{n=-\infty}^{\infty} F_n[A_n^1 J_n(m_1kr) - a_n^1 H_n^{(2)}(m_1kr)]$$

$$(r < a) \qquad v = \sum_{n=-\infty}^{\infty} F_n A_n^2 J_n(m_2kr)$$

where

$$F_n = (-1)^n \exp[jn\theta + j\omega t]$$
$$k = 2\pi/\lambda_0$$

$a_n$, $b_n$, $A_n$ and $B_n$ are undetermined coefficients.

The coefficients are determined by solving the equations obtained from the boundary conditions that $mu$, $m\partial u/\partial r$, $m^2 v$ and $\partial v/\partial r$ are continuous at $r = a$ and $r = b$. The equations and the solutions for the coefficients describing the scattered field [$a_n^0$ and $b_n^0$] are given by Kerker and Matijevic[6] in the form of quotients of $4 \times 4$ determinants involving Bessel and Hankel functions.

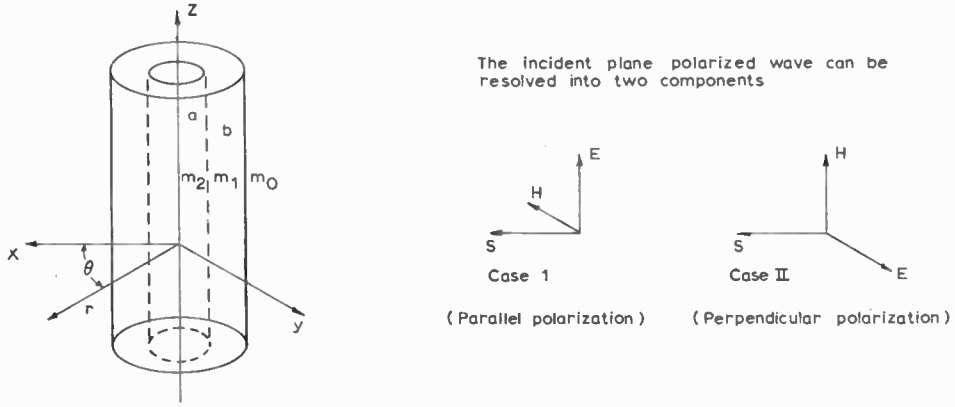


**Fig. 2.** Coordinates and vectors for scattering of a normally incident plane wave by concentric cylinders (after Kerker and Matijevic[6]).

The principal asymptotic form of the Hankel function is

$$H_n^{(2)}(kr) \simeq \left[\frac{2}{\pi kr}\right]^{\frac{1}{2}} \exp\left[-jkr+j(2n+1)\pi/4\right]$$

for $kr \gg 1$ and $kr \gg n$.

Van de Hulst[9] shows that the scattered field at infinity is given by a function $u$ which has the form

$$u = \left[\frac{2}{\pi kr}\right]^{\frac{1}{2}} \exp\left[-jkr+j\omega t-j3\pi/4\right]T_1(\theta)$$

for $kr \gg 1$ and for the incident **E** vector parallel to the cylinder axis (Case I).

The amplitude function of the scattered wave is

$$T_1(\theta) = \sum_{n=-\infty}^{\infty} b_n^0 \exp\left[jn\theta\right]$$

$$= b_0^0 + 2\sum_{n=1}^{\infty} b_n^0 \cos(n\theta)$$

Similarly, for the case of **E** perpendicular to the cylinder axis (Case II)

$$T_2(\theta) = a_0^0 + 2\sum_{n=1}^{\infty} a_n^0 \cos(n\theta)$$

Only coefficients of positive order are needed because

$$b_n^0 = b_{-n}^0, \quad a_n^0 = a_{-n}^0$$

The $E_z$ component of the electric field vector is proportional to $|u|^2$. Therefore, if $I_0$ is the incident intensity, the intensity of light scattered in the direction $\theta$ at a large distance $r$ from the cylinder is

$$I_1 = \left(\frac{2}{\pi rk}\right)\left|T_1(\theta)\right|^2 I_0, \qquad \text{for Case I}$$

and

$$I_2 = \left(\frac{2}{\pi rk}\right)\left|T_2(\theta)\right|^2 I_0, \qquad \text{for Case II}$$

These forms of the angular intensity distribution apply also to a homogeneous single cylinder and to any number of concentric cylinders. However, the coefficients of the amplitude functions for the scattered wave become more difficult to calculate as the number of concentric cylinders increases. In the simplest case, that of a single cylinder, the coefficients are given by

$$b_n^0 = \frac{\begin{vmatrix} J_n(m_0\alpha) & J_n(m_1\alpha) \\ m_0 J_n'(m_0\alpha) & m_1 J_n'(m_1\alpha) \end{vmatrix}}{\begin{vmatrix} H_n(m_0\alpha) & J_n(m_1\alpha) \\ m_0 H_n'(m_0\alpha) & m_1 J_n'(m_1\alpha) \end{vmatrix}}$$

$$a_n^0 = \frac{\begin{vmatrix} m_0 J_n(m_0\alpha) & m_1 J_n(m_1\alpha) \\ J_n'(m_0\alpha) & J_n'(m_1\alpha) \end{vmatrix}}{\begin{vmatrix} m_0 H_n(m_0\alpha) & m_1 J_n(m_1\alpha) \\ H_n'(m_0\alpha) & J_n'(m_1\alpha) \end{vmatrix}}$$

where $\alpha = kb(=ka)$ and $m_1 = m_2$. The primes denote derivations with respect to the argument.

## 3. Geometrical Optics Solution for Large Cylinders[11]

The case of coherent light scattering by an uncladded dielectric cylinder in air will be treated.

Let the glass have refractive index $m$. The scattered light will have cylindrical symmetry. The diffraction pattern in the far-field produced by laser illumination of the fibre is that due to a slit of width $2b$.

Near the forward direction $\phi = 0$, the diffracted light has an amplitude comparable to that of the refracted and reflected light, and the minima have an angular spacing of $d\phi = \lambda/2b$.

The refracted and singly reflected light will interfere over the range $\phi = 0$ to $\phi = 2\cos^{-1}(1/m)$ or about 96° for $m = 1{\cdot}5$.

The path difference between rays 1 and 2 before and after passing through the cylinder will now be calculated. (See Fig. 3.)

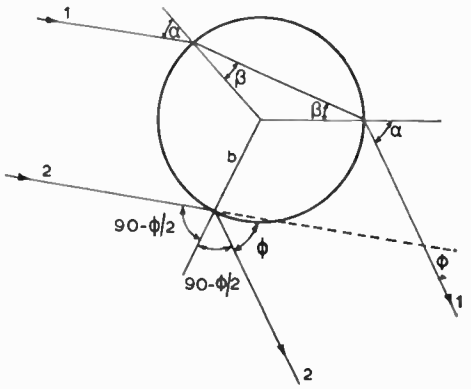


**Fig. 3.** Calculation of path differences.

Only the case of perpendicular polarization will be treated as the results for parallel polarization are easily obtainable from these.

Let this path difference be $\Delta$.

Then

$$\Delta = 2b\sin\phi/2 + 2mb\cos\beta - 2b\cos\alpha - \frac{\lambda}{2}$$

Eliminating $\alpha$ and $\beta$, we get

$$\Delta = 2b\sin\phi/2 + 2b\sqrt{1+m^2-2m\cos\phi/2} - \frac{\lambda}{2}$$

Equating $\Delta = k\lambda$, for $k = 0, 1 \ldots$ will give the angular positions of the maxima.

Primary and secondary rainbows will occur between 150° and 180° and from 70° to 100° respectively. These will considerably modify the angular fringe spacing calculated above.

## 4. Practical Considerations in Optical Fibre Scattering Measurements

The accurate computation of scattering parameters and their variation with small changes in the properties of the scatterer is a direct way of determining the usefulness of scattering measurements in the study of optical waveguide fibres.

An experimental study of a fibre core may involve measurements of either the angular scattering pattern of the core alone, or the modulation of the overall pattern by the component due to the core. If the refractive index difference between the core and cladding is much less than that between the cladding and the surrounding air or vacuum, the light scattered by the core is likely to be swamped by the greater intensity of scattered light from the cladding especially around the forward direction. The core scattering could be investigated more directly if the fibre were immersed in a liquid with a refractive index matching that of the fibre cladding. In practice, this means matching the refractive indices to much better than 1%. The matching liquid would have to be free from any suspension of particles which could cause scattering and introduce a high level of background noise to the fibre scattered signal.

The scattering problem of a cladded fibre in a matching liquid (of large extent and slightly lower refractive index) reduces to that of a thin cylinder in an infinite medium of refractive index $m_1$. If the wavelength of the scattered light is $\lambda_0$ in vacuum, the size parameter of the cylindrical core is now

$$x = \frac{2\pi a m_1}{\lambda_0}$$

$$\simeq 15 \quad \text{for } a = 1\ \mu\text{m and } \lambda_0 = 633\ \text{nm}.$$

The phase parameter $p = 2x(M-1)$ becomes

$$p = 2x\left|\frac{m_2}{m_1} - 1\right|$$

$$= \frac{4\pi a}{\lambda_0}|m_2 - m_1|$$

$$\simeq 0{\cdot}2 \quad \text{for } |m_2 - m_1| \simeq 0{\cdot}01$$

The scattering is now due to an object with a moderate value of $x$ and a small value of $p$.

## 5. Theoretical Computation

A computer program has been written for the calculation of the angular distribution of intensities scattered by a single fibre immersed in an infinite medium of refractive index $m_1$.

The scattered intensities have been calculated for the cases of the incident plane waves having parallel and perpendicular polarizations, and also their ratio.

Particular attention was paid to the evaluation of the Bessel functions. The IBM library subroutine which uses the backward interpolation formula has been adapted. The $n$ orders of the Bessel function of a particular argument are generated simultaneously in a single array.

$$H_n(\alpha) = J_n(\alpha) - jY_n(\alpha) \quad \text{where } \alpha = \frac{2\pi}{\lambda_0} m_1 a$$

and

$$Y_{n+1}(\alpha) = -\frac{2}{\pi\alpha}\frac{1}{J_n(\alpha)} + \frac{J_{n+1}(\alpha)}{J_n(\alpha)} Y_n(\alpha)$$

are used for calculating $H_n(\alpha)$ with $Y_0(\alpha)$ from the series representation. The accuracy of the Bessel functions is a parameter which can be varied. It was fixed at 0·001. This was found to be adequate for $\alpha$ up to 20.

*Case I:* with $m_1 = 1$ and $m_2$ around 1·50; $\alpha$ is taken from 4 to 20.

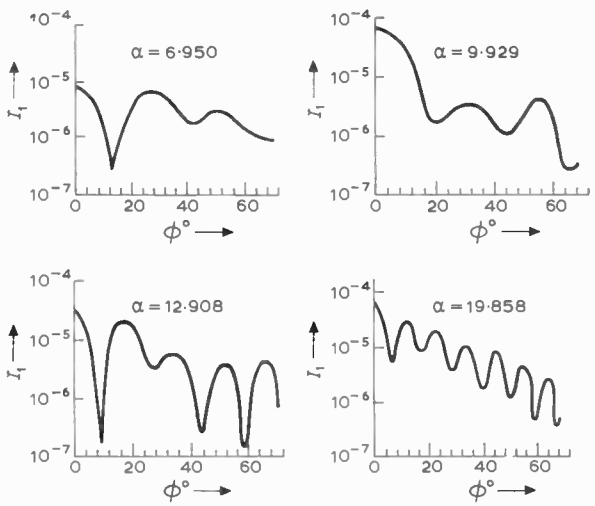


**Fig. 4.** Intensity scattering by a single fibre of refractive index 1·50 in air for various values of $\alpha$, for the case of parallel polarization of the incident light. The incident beam has unit intensity.

Referring to Fig. 4, it will be seen that, as $\alpha$ increases, the angular distribution pattern becomes more complex and requires more points for detailed characterization. The program, however, can easily cope for $\alpha$ up to 20 which corresponds to a fibre diameter of about $7\lambda$.

*Case II:* $m_1 = 1{\cdot}526$ and $m_2 = 1{\cdot}621$; $\alpha$ is taken from 4 to 15.

Figure 5 shows a similar tendency to Case I. There is a decrease in the level of the scattered energy compared to Case I.

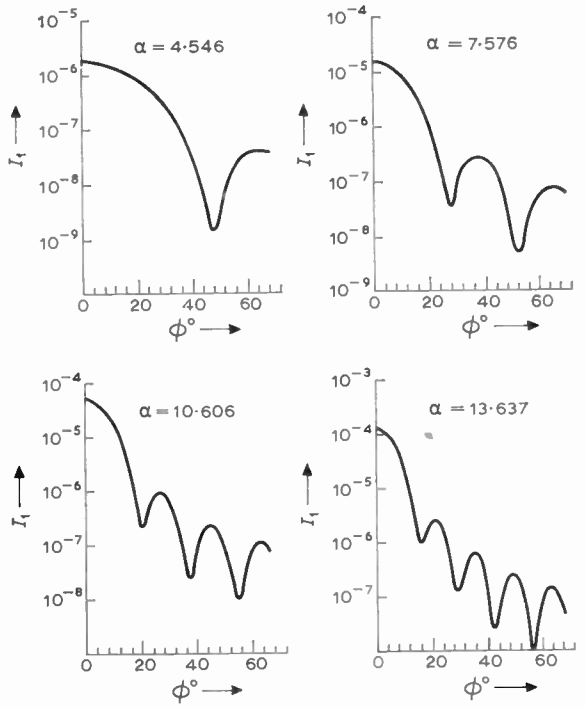


**Fig. 5.** Intensity scattering by a cladded fibre immersed in an index matching liquid for various values of α, for the case of parallel polarization of the incident light. The incident beam has unit intensity.

$$M = \frac{m_2}{m_1} = 1{\cdot}06. \quad M_2 = 1{\cdot}526$$

## 6. Experimental Procedure and Results

For single and cladded fibres in air, the angular scattering patterns are obtained by direct photographic recording. (See Fig. 6.) The fibre was mounted in the centre of a powder X-ray camera and was illuminated perpendicularly by a helium-neon laser of wavelength 0·6328 μm. For a cladded fibre in air the intensity of the light scattered by the core is approximately $(a/b)^2$ times the intensity of the light scattered by the cladding. Hence for $b = 25a$, the scattered intensity ratio is 0·16%. For such a fibre, the scattering pattern will give negligible information about the core.

However, the overall diameter may be measured by correlating the angular fringe spacing with the overall diameter. This was done in the following manner.

### 6.1. Angular Separation of the Fringes

The following is valid if $(b/\lambda) \gg 1$.

For $\mathbf{E}_\perp$,

Path difference $\Delta$

$$= 2b \sin \phi/2 + 2b[1 + m^2 - 2m \cos \phi/2]^{\frac{1}{2}} - \frac{\lambda}{2}$$

$$\frac{d\Delta}{d\phi} = b \cos \phi/2 + \frac{mb \sin \phi/2}{\sqrt{1 + m^2 - 2m \cos \phi/2}}$$

For neighbouring minima or maxima, $d\Delta = \lambda$

Therefore

$$d\phi = \frac{\lambda}{b\left[\cos \phi/2 + \dfrac{m \sin \phi/2}{\sqrt{1 + m^2 - 2m \cos \phi/2}}\right]}$$

Figure 7 shows a minima at 60° for $m = 1{\cdot}526$. The shape of the graph is independent of the fibre size for large fibres.

### 6.2. Experimental Results

The diameters of the fibres were measured with an accurate micrometer. For comparison purposes a travelling microscope was used to measure the fringe spacing $d\phi$ about $\phi$ on the films. An average over

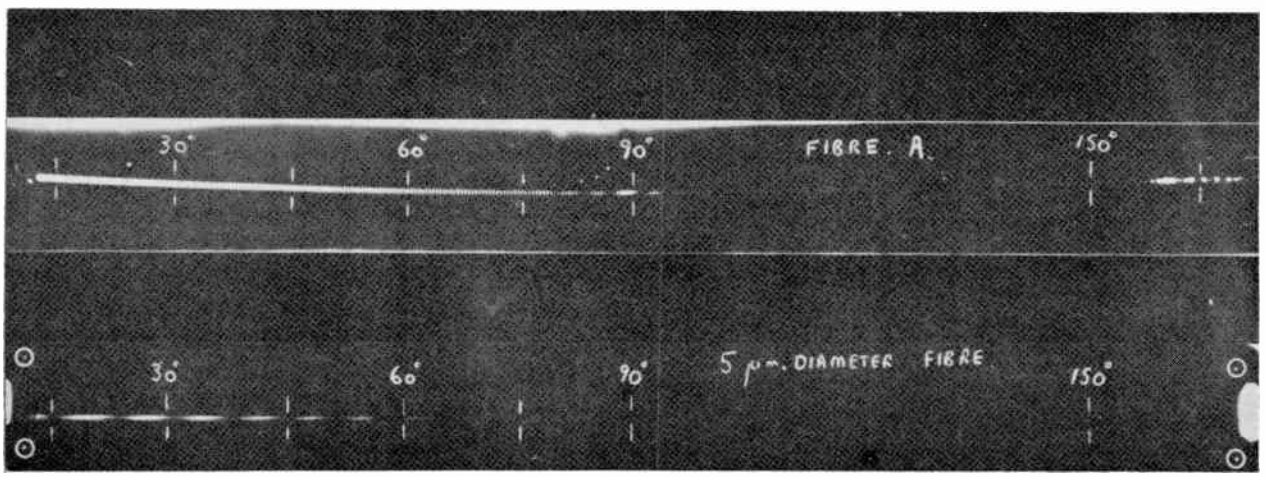


**Fig. 6.** Photographs of the scattering patterns. The fibres are in air.

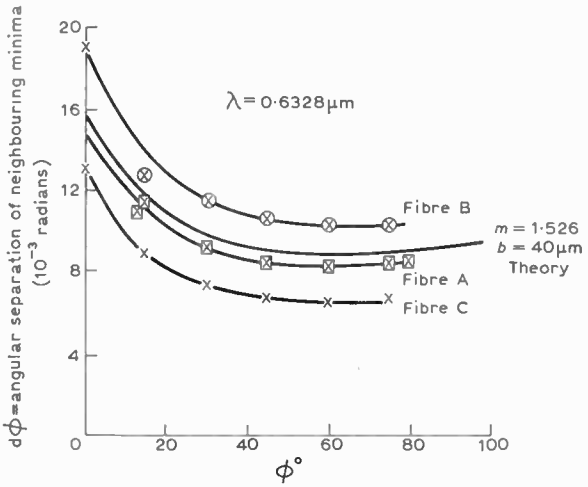


Fig. 7. Angular separation of fringes.

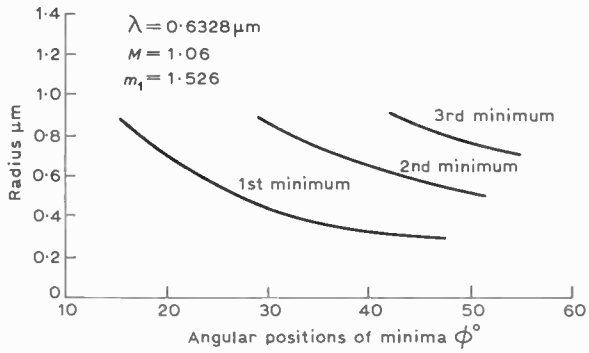


Fig. 8. Scattering by fibre core.

10 fringes was taken to estimate an average value for each $d\phi$. Table 1 shows the results. These are also plotted in Fig. 7.

In practice, considerably more accurate results can be obtained by using a photomultiplier on an angular scale to detect the fringe positions. Readings were not taken for $\phi$ greater than 75° since the secondary rainbow caused a different pattern from the one derived above.

In practice the waveguide will be made from glasses having refractive indices in the range 1·45 to 1·7. It was found using geometrical optics, for this refractive index range, that a fibre of given diameter has a negligible change in fringe spacing (near $\phi = 60°$) with refractive index variation but the fringes themselves (near $\phi = 60°$) shifted by 0·8° for a 1% variation in refractive index $m$. Thus for a fibre of given diameter which is made from glasses in this refractive index range, the fringe spacing is independent of whether the fibre is cladded or single. This ensures that the above method is valid for the diameter measurement of cladded fibres. If now the fringe position is measured, the cladding refractive index may be determined.

The coherent light scattering patterns produced by fibres with diameters down to 1 μm in air were also observed. A pyrex rod was heated and pulled over a bunsen flame. The fine fibre was mounted with extreme care. The resulting pattern showed its first minimum at about 20°. This corresponds to a radius of about 1 μm (see Fig. 4 top right).

For fibres immersed in a liquid medium with refractive index near to that of the cladding, the scattered light is clearly visible. This light is due to scattering by the core. The liquid used was di-bromo ethane having $n^{20} = 1·54$; this was contained in a thin walled glass beaker. The fibre used had a cladding of about 1·53 at the D line. By heating the liquid on an electrical hot plate, matching was achieved. This particular small core fibre showed its first minimum at about 22°. This corresponds to a core radius of about 0·6 μm (see Fig. 8). For fibres having core sizes less than 0·3 μm the scattering pattern was dominated by scattering from centres in the liquid. Figure 8 indicates a way of determining the core diameter by means of index matching. However, the relative index $M$ must be known approximately since

**Table 1.** Experimental results

| | Fibre A $m = 1·526$ | | Fibre B $m = 1·562$ | | Fibre C $m = 1·579$ | |
|---|---|---|---|---|---|---|
| Diameter from micrometer reading μm | 84±1 | | 67±1 | | 109±1 | |
| | $\phi$° | $d\phi \times 10^4$ radians | $\phi$° | $d\phi \times 10^4$ radians | $\phi$° | $d\phi \times 10^4$ radians |
| Experimental results | 13 | 111±3 | | | | |
| | 15 | 115±3 | 15 | 127±3 | 15 | 88±2 |
| | 30 | 93±2 | 30 | 115±3 | 30 | 73±2 |
| | 45 | 85±2 | 45 | 108±3 | 45 | 68±2 |
| | 60 | 83±2 | 60 | 103±3 | 60 | 64±2 |
| | 75 | 84±2 | 75 | 104±3 | 75 | 67±2 |
| Diameter from fringe spacing at 60 μm | 85·3±0·8 | | 69·4±0·6 | | 111·2±1·5 | |

it was found using the wave theory that the fringe positions shifted by 1/3° for a 1% variation in $M$.

## 7. Discussion and Conclusion

The use of a laser source for scattering experiments enabled well-defined angular intensity distribution patterns to be easily obtained by photographic means and by suitable narrow field of view detectors.

It has been demonstrated that the application of scattering techniques to the measurement of refractive indices and radii of single and cladded fibres could yield useful results over a wide range of fibre sizes provided that experimental techniques were suitably arranged. The techniques are particularly useful for single fibres from 1 to 100 μm. The method can be used as a means of monitoring fibre diameters during production.

For cladded fibres, the technique is expected to resolve a core diameter of 0·6 μm in a uniform cladding of index difference 1% from the core.

The complexity of the results stresses the need for careful interpretation of experimental data based on a sound theoretical background.

## 8. References


1. Farone, W. A. and Kerker, M., 'Light scattering from long-submicron glass cylinders at normal incidence', *J. Opt. Soc. Amer.*, **56**, pp. 481–6, April 1966.
2. Cooke, D. and Kerker, M., 'Photometer for measurement of the light scattered by large submicron cylinders at both perpendicular and oblique incidence', *Rev. Sci. Instrum.*, **39**, pp. 320–3, March 1968.
3. Lord Rayleigh, 'On the electromagnetic theory of light'. *Phil. Mag.*, **12**, pp. 81–101, August 1881.
4. Wait, J. R., 'Scattering of a plane wave from a circular dielectric cylinder at oblique incidence', *Canad. J. Phys.*, **33**, pp. 189–95, May 1955.
5. Van de Hulst, H. C., 'Light Scattering by Small Particles', (Wiley, New York, 1957).
6. Kerker, M. and Matijevic, E., 'Scattering of electromagnetic waves from concentric infinite cylinders', *J. Opt. Soc. Amer.*, **51**, pp. 506–8, May 1961.
7. Farone, W. A. and Querfeld, C. W., 'Electromagnetic scattering from radially inhomogeneous infinite cylinders at oblique incidence', *J. Opt. Soc. Amer.*, **56**, pp. 476–80, April 1966.
8. Debye, P., *Physik Z.*, **9**, p. 775, 1908.
9. Van de Hulst, H. C., *op. cit.*, Chap. 15.
10. Lind, A. C. and Greenberg, J. M., 'Electromagnetic scattering by obliquely oriented cylinders', *J. Appl. Phys.*, **37**, pp. 3195–203, July 1966.
11. Gebhart, J. and Schmidt, S., 'Interference effects of thin transparent glass fibres in coherent illumination', *Z. Angew. Phys.*, **19**, No. 2, pp. 141–143, April 1965.


*Manuscript received by the Institution on 7th February, 1969.* ( *Paper No. 1303/IC19.*)



## STANDARD FREQUENCY TRANSMISSIONS—January 1970

*(Communication from the National Physical Laboratory)*

| Jan. 1970 | Deviation from nominal frequency in parts in $10^{10}$ (24-hour mean centred on 0300 UT) | | | Relative phase readings in microseconds N.P.L.—Station (Readings at 1500 UT) | | Jan. 1970 | Deviation from nominal frequency in parts in $10^{10}$ (24-hour mean centred on 0300 UT) | | | Relative phase readings in microseconds N.P.L.—Station (Readings at 1500 UT) | |
|---|---|---|---|---|---|---|---|---|---|---|---|
| | GBR 16 kHz | MSF 60 kHz | Droitwich 200 kHz | *GBR 16 kHz | †MSF 60 kHz | | GBR 16 kHz | MSF 60 kHz | Droitwich 200 kHz | *GBR 16 kHz | †MSF 60 kHz |
| 1 | — 300·1 | 0 | + 0·1 | 649 | 551·6 | 17 | — 300·0 | 0 | + 0·1 | 655 | 560·9 |
| 2 | — 300·1 | — 0·1 | 0 | 650 | 552·6 | 18 | — 299·9 | — 0·1 | + 0·1 | 654 | 561·6 |
| 3 | — 300·0 | — 0·2 | 0 | 650 | 554·4 | 19 | — 300·2 | 0 | + 0·1 | 656 | 561·8 |
| 4 | — 299·9 | — 0·1 | 0 | 649 | 555·4 | 20 | — 300·1 | — 0·1 | + 0·1 | 657 | 562·4 |
| 5 | — 300·1 | — 0·1 | 0 | 650 | 556·2 | 21 | — 299·9 | 0 | + 0·1 | 656 | 562·8 |
| 6 | — 300·2 | — 0·1 | 0 | 652 | 557·0 | 22 | — 300·0 | 0 | + 0·1 | 656 | 562·8 |
| 7 | — 300·2 | 0 | + 0·1 | 654 | 557·0 | 23 | — 300·0 | 0 | + 0·1 | 656 | 562·6 |
| 8 | — 300·0 | 0 | + 0·1 | 654 | 557·0 | 24 | — 299·8 | 0 | 0 | 654 | 562·4 |
| 9 | — 300·1 | 0 | 0 | 655 | 556·6 | 25 | — 299·9 | 0 | + 0·1 | 653 | 562·7 |
| 10 | — 300·1 | — 0·1 | 0 | 656 | 557·4 | 26 | — 300·0 | — 0·1 | + 0·1 | 653 | 563·7 |
| 11 | — 300·0 | — 0·1 | 0 | 656 | 558·2 | 27 | — 299·9 | 0 | + 0·2 | 652 | 563·8 |
| 12 | — 300·2 | — 0·1 | 0 | 651 | 569·2 | 28 | — 299·9 | — 0·1 | + 0·1 | 651 | 565·2 |
| 13 | — 300·1 | 0 | 0 | 652 | 568·8 | 29 | — 300·0 | — | + 0·1 | 651 | — |
| 14 | — 300·1 | — 0·1 | 0 | 653 | 560·2 | 30 | — 300·0 | 0 | + 0·1 | 651 | 564·8 |
| 15 | — 300·1 | — 0·1 | 0 | 654 | 560·8 | 31 | — 299·8 | 0 | + 0·1 | 649 | 565·0 |
| 16 | — 300·1 | 0 | 0 | 655 | 560·8 | | | | | | |

All measurements in terms of H.P. Caesium Standard No. 334, which agrees with the N.P.L. Caesium Standard to 1 part in $10^{11}$.

Note: The frequency offset of GBR for 1970 is $-300 \times 10^{-10}$

* Relative to UTC Scale; $(UTC_{NPL} - Station) = +500$ at 1500 UT 31st December 1968.

†Relative to AT Scale; $(AT_{NPL} - Station) = +468{\cdot}6$ at 1500 UT 31st December 1968.

# LETTERS

### Weighing Vehicles in Motion

I have just been reading Mr. Ferguson's paper in the August issue of *The Radio and Electronic Engineer*.† It was only after seeing his Fig. 8 that I realized something which I should have thought of before, namely that weighing in a limited time involves simply the problem of integrating over a fixed period a constant signal accompanied by unknown alternating signals or 'noise'. For every operation in the time domain there is a corresponding operation in the frequency domain, so that observing the signal for a sharply bounded time corresponds to passing the signal through a (frequency) filter of $\sin x/x$ form.‡ The frequency 'side-lobes' corresponding to an abrupt cut in time cause the result to include significant contributions from components with periods shorter than the integration time. The design of window functions to minimize this has been discussed by Blackman and Tukey§ and in particular the Hamming window $\frac{1}{2}(1{\cdot}08+0{\cdot}92\cos\pi\tau/2T)$ is very similar to Mr. Ferguson's weighting function.

The only constructive point arising from this treatment is to note that all this work assumes that the amplitude of the interfering components remains constant during the period of observation. If the damping is appreciable, even better results ought to be obtainable by using a correspondingly adjusted weighting function which would be asymmetric in favour of the later part of the period of integration.

D. A. Bell

Department of Electronic Engineering,
The University, Hull. *8th December 1969.*

With regard to Professor Bell's letter the main point appears to be the proposal that an asymmetric 'weighting' function should be applied. There is in practice very slight damping during the weighing period and the amount of damping varies with the type and condition of the vehicle being weighed. No specific degree of asymmetry would be ideal nor is presetting prior to each weighing a practicable proposition. To justify the additional cost of introducing asymmetry, some real advantage would be required.

In my paper, I made the point that greater attenuation could be obtained with more complex 'weighting' functions. As the complexity of the function increases so does the complexity of the electronic circuitry required to reproduce it. Another factor of equal importance is the need for a closer approximation to the theoretical curve in order to achieve higher performance standards. In practice a compromise is reached between accuracy of reproduction and complexity of function, the selection of which requires considerable skill and experience.

A. C. Ferguson

W. & T. Avery Limited,
Development Unit,
Tame Bridge,
Walsall, Staffordshire. *16th January 1970.*

### Advertisements in the Journal

In this world of pecuniary embarrassment, it was with some trepidation that I read in the Annual Report of the Institution's desire for increased advertising revenue. I do, of course, appreciate the financial advantage accruing from advertising, but I would like to make a plea: please don't encourage this aspect of the *Journal!* So many technical publications are cluttered with a mass of advertising jargon, that it is pleasing to open a copy of the *Journal* and thumb through this quality dissemination of knowledge, unhindered by the usual exhortations to buy. If advertising revenue is a necessity, would it not be possible to confine this activity to the *Proceedings*, especially as it is now to be published monthly? Personally, I would be extremely happy if this is a practical proposition and I feel that such a move would only serve to enhance the quality and reputation of the *Journal.* Do any other readers hold similar views?

Ian E. Shepherd

3 Aylwin Close,
Basingstoke, Hants. *8th October 1969.*

[We have much sympathy with Mr. Shepherd. The fact is that the proportion of members' subscriptions which can be allocated towards the cost of producing the *Journal* is not sufficient without the assistance of revenue from advertisements. It will have been noted that subscriptions to the *Journal* payable by non-members (libraries, etc.) have had to be increased with effect from January 1970 (see *The Radio and Electronic Engineer* for November 1969, page 250).

The proposal that advertisments should be confined to the *Proceedings of the I.E.R.E.* is at first sight a reasonable one: the *Proceedings* is published for members in Great Britain only and separate, similar publications are produced in India and Canada for members in those countries. There are however important reasons for placing advertisements in the *Journal.* Regrettably British electronics companies in general are reluctant to advertise their products in overseas publications and hence would be unlikely to support the Institution to the same extent even if advertisements appeared in all three *Proceedings.* It is the Institution's view that British products *should* be advertised abroad and *The Radio and Electronic Engineer* is therefore the medium through which this can be done most effectively because of its wide circulation.

However, the writer may be assured that advertisements which appear in the *Journal* are selective in that the Institution reserves the right to decline any inappropriate announcement. In any case advertisements are kept completely separate from the technical contents of the *Journal* and the proportion of technical contents to advertisements is well above the level customary in commercial journals.—Editor.]

† Ferguson, A. C., 'Weighing vehicles in motion', *The Radio and Electronic Engineer*, **38**, No. 2, pp. 109–119, August 1969.
‡ Bennett, R. R. and Fulton, A. S., 'The generation and measurement of random noise', *J. Appl. Phys.*, **22**, p. 1187, 1951.
§ Blackman, R. B. and Tukey, J. W., 'The Measurement of Power Spectra' (Dover, New York, 1959).

UDC 681.12 : 681.38

# Automatic, On-line Calibration of Flowmeters

*By*

**P. RIDLEY,**
P.Eng., C.Eng., M.I.E.R.E.†

This paper describes a method of calibrating digital output flowmeters of the turbine meter type whilst the meters are in use. No interruption of the metering process is involved during calibration. In the specific application for which the system was designed, the volumes of batches of refined petroleum products 'shipped' in an oil pipeline are metered to an accuracy of 0·05%. Meter calibration cycles are initiated automatically when product types or flow rates change.

## 1. Introduction

The flow of liquids and gases is frequently measured using turbine flowmeters which can be cheap, robust and reliable. (Fig. 1.) Although the accuracy of this type of meter is typically 0·25% of the nominal value of output pulses per volume through the meter, repeatability is often as high as 0·01%. It is possible, therefore, to measure flow very accurately once the meter calibration factor has been determined.

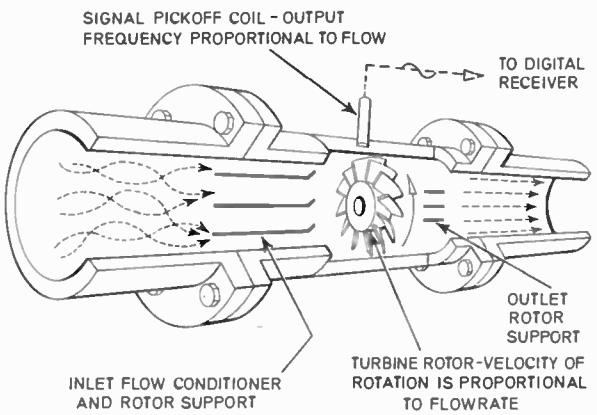


**Fig. 1.** Basic operation of turbine flowmeter.

One method of accurate measurement is to calibrate the flowmeter off-line and supply calibration curves as shown in Fig. 2. However, accurate metering to better than 0·1% becomes a complicated task.

An improved method is to calibrate on-line by passing a known volume ($V$) of product through the flowmeter and counting the number of pulses ($P$) generated. The ratio $P/V$ is the calibration factor ($F$) in pulses per unit volume. This can be applied to the total meter pulse count ($P_x$) to give the total volume ($V_x$) through the meter, i.e.

$$V_x = \frac{P_x}{F}.$$

† Formerly Serck Controls Limited, Leamington, Warwickshire; now with Northern Electric Co. Ltd., Research and Development Laboratories, Ottawa, Ontario, Canada.

This technique has been used, with all computations carried out off-line.

A further improvement is to carry out the flow correction (i.e. the determination of volume throughput $V_x$) automatically on-line once the calibration factor has been computed off-line. Systems of this type are frequently used.

The system described here permits fully automatic on-line calibration and flow correction. Any significant change in parameters that are known to affect calibration (e.g. flow rate, viscosity) automatically initiate a meter calibration cycle.

## 2. General System *(See Figs. 3 and 4)*

### *2.1 Prover Volume*

In order to determine the known volume of the product, $V$, a section of the pipeline, the prover loop, has two detectors fitted some distance apart, the volume between them being known accurately.

When calibration of a meter is to be carried out, a polyurethane sphere is injected into the prover loop and is pushed along by the product. As the sphere passes the first (START) detector, counting of meter pulses is initiated, continuing until the sphere passes the second (STOP) detector.

The meter factor is computed from $F = P/V$. However, $V$, the volume of the prover and hence the volume of product between START and STOP detectors, varys with pipe temperature because of cubical expansion.

Let the volume of the prover loop be $V_p$ at 60°F (15·5°C) then

$$V = V_p[1+(t-60)E_M]$$

where $t$ is the prover temperature in deg F and $E_M$ is the cubical expansion factor for the pipe.

Therefore

$$F = \frac{P}{V_p[1+(t-60)E_M]} \qquad \text{.....(1)}$$

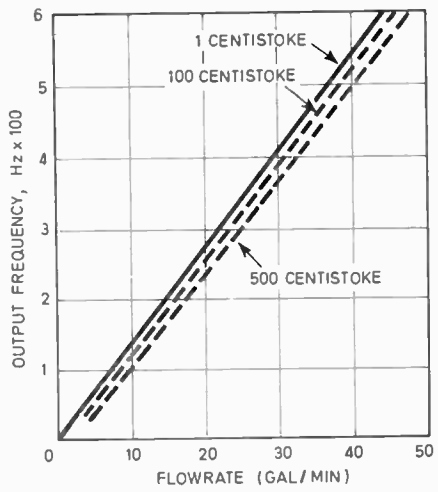


(a) Plot of frequency versus volumetric flow.

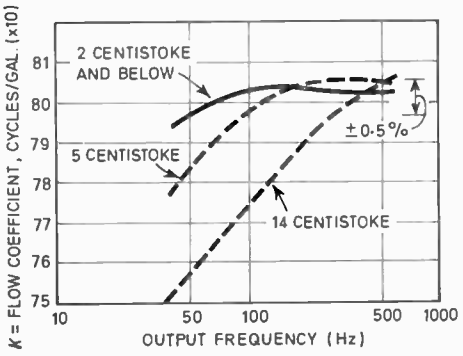


(b) Cycles per gallon plotted against output frequency.

### 2.2 Meter Serviceability

Before computing a meter factor, checks are carried out on the accuracy and repeatability of the meter. This necessitates two cycles of the sphere in the prover, the pulse count corresponding to the first cycle being checked to be within 10% of the nominal figure. The second pulse count is then checked to be within 0·01% of the first.

**Fig. 2.** (left) Presentation of calibration data and development of the calibration curve.

Turbine meter calibration data can be presented in two ways. A plot of frequency versus volumetric flow rate can be used as shown in (a), the ideal being a straight line through zero. Note that as the viscosity increases, the frequency output at a given flow rate decreases as a result of the viscous drag.

To achieve the degree of readability compatible with the inherent accuracy of the turbine flowmeter, a more practical method of showing the data is to plot the slope of the curve in (a) against frequency. This plot is a curve of frequency divided by flow rate versus frequency or, by eliminating the time factor, cycles per gallon versus frequency. The parameter cycles per gallon, the vertical axis of the curve in (b), is termed the 'flow coefficient' or $K$. The ideal plot of $K$ versus frequency is a straight horizontal line.

The sample data shown by the solid line in (b) deviate from the ideal by no greater than 0·5% of rate down to the minimum frequency that determines the limit of the linear range of the meter. At any point above this minimum linear frequency, $K$ can be applied to any frequency measurement. The linear range of $K$ depends on fluid viscosity, as exhibited for one meter design by the dashed curve shown in (b).

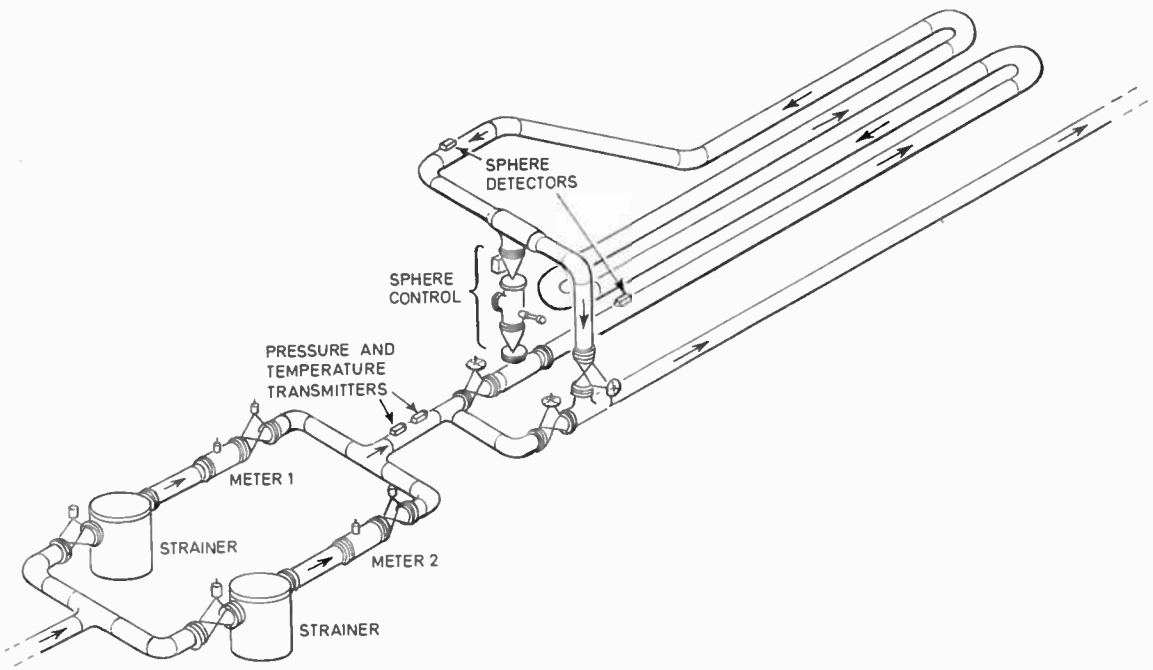


**Fig. 3.** Typical meter and prover installation.

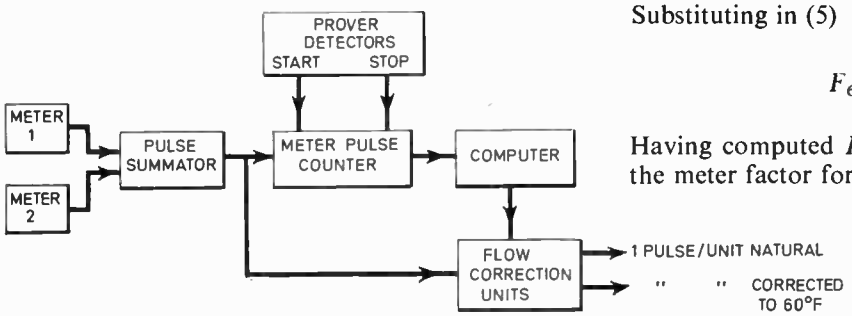


Fig. 4. System block diagram.

Failure of either check starts off another accuracy check, three successive failures causing a PROVER FAIL alarm to be given.

On completion of satisfactory prover cycles, a new meter factor is computed.

### 2.3 Flow Measurement

The computed meter factor is applied to the meter output to give the natural volume of product passing the meter. However, this is the volume at product temperature $t$, whereas, for inventory purposes, the volume at 60°F is required.

The relationship between $V_t$ and $V_{60}$ is

$$V_{60} = V_t[1+(60-t)E] \qquad \text{.....(2)}$$

where $E$ is a correction factor for the particular product being shipped.

For a volume of product at temperature $t$, $V_t$, let the number of meter pulses be $P$, then

$$P = V_t \times F \qquad \text{.....(3)}$$

For the equivalent volume of 60°F, $V_{60}$

$$P = V_{60} \times F_{60} \qquad \text{.....(4)}$$

From (3) and (4)

$$V_t \times F = V_{60} \times F_{60}$$

or

$$F_{60} = \frac{V_t}{V_{60}} \times F \qquad \text{.....(5)}$$

From (2)

$$\frac{V_t}{V_{60}} = \frac{1}{1+(60-t)E}$$

Substituting in (5)

$$F_{60} = \frac{F}{1+(60-t)E}$$

Having computed $F$, it is then possible to determine the meter factor for corrected volume of product.

The corrected factor $F_{60}$ is applied to the meter output to measure corrected flow.

Since the corrected factor is dependent upon temperature, frequent checks are made on the product temperature and a new factor computed if a change of 0·2 deg F or more occurs.

### 2.4 Flow Rate

Meter pulses are counted over a 10-second interval and flow rate computed from:

$$\text{flow rate} = \frac{\text{volume}}{\text{hour}}$$

$$= \frac{\text{pulses}}{10 \text{ seconds}} \times \frac{\text{volume}}{\text{pulses}} \times \frac{10 \text{ seconds}}{\text{hour}}$$

$$= \frac{\text{pulses}}{10 \text{ seconds}} \times \frac{1}{F} \times 360$$

$$= \frac{360}{F} \times \frac{\text{pulses}}{10 \text{ seconds}}$$

Because the meter calibration may vary with flow rate, a 10% change in flow rate initiates a new prover cycle.

## 3. Design Details

### 3.1 Meter Pulse Summator

Normally only one meter is in use except when changing from one to the other. However, since it is possible to have both in line together, meter outputs are fed into a summator which converts the two asynchronous outputs into a train of timed pulses.

### 3.2 Meter Pulse Counter (Fig. 5)

Pulses are counted either over the prover volume for meter factor computation or over 10 seconds for flow rate.

The counter comprises five decade counters, each of which is a four-bit binary counter arranged to reset every ten counts.

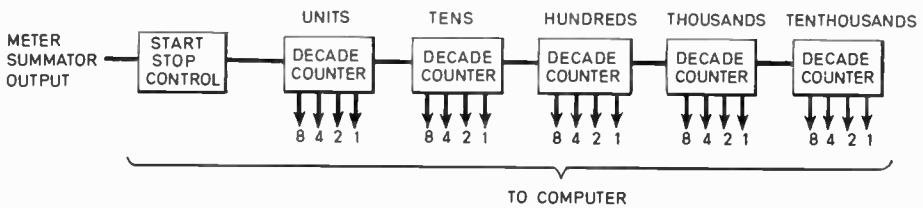


Fig. 5. Meter pulse counter.

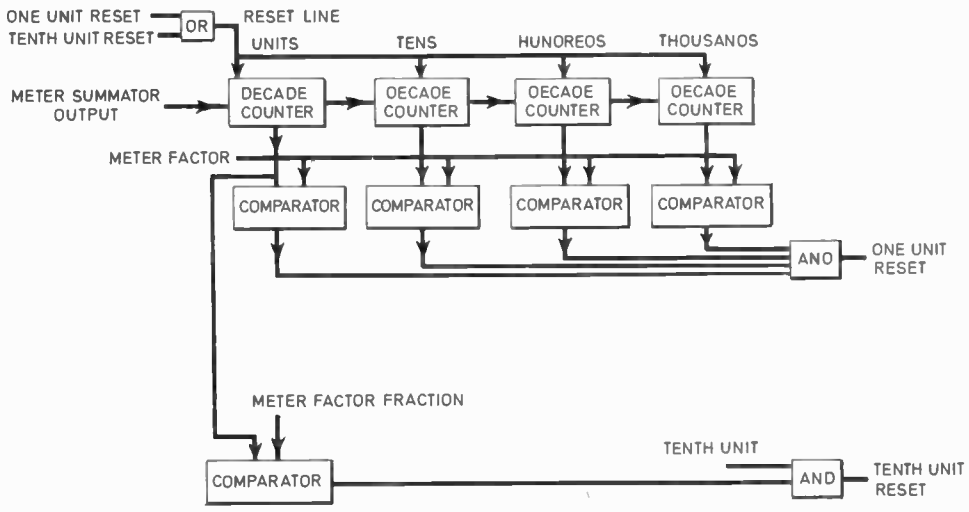


**Fig. 6.** Flow correction unit.

If no meter calibration cycle is in process, meter pulses are counted for a flow-rate computation. When the computer has read in the pulse count, the counter is reset and counts pulses again for another flow-rate computation. During meter calibration cycles, flow rate computation is inhibited and the counter controlled by the prover START and STOP detectors. Following a prover stop signal, either a meter accuracy or repeatability check is demanded.

### *3.3 Flow Correction (Fig. 6)*

Flow correction is applied to the meter by counting meter summator pulses in a four-decade counter until the count is equal to the computed meter factor, when the counter is reset and a one-unit volume pulse generated.

Because of the accuracy required, the meter factor is computed to one decimal place, the fractional part being applied every ten units. For example, let the meter factor be $abcd.e$ pulses per unit of product. Every $abcd$ pulses, a one unit pulse is generated, but every tenth unit an extra '$e$' pulses are counted. The total pulse count for ten units is $9 \times abcd + (abcd + e) = 10\ abcd + e = 10\ (abcd.e)$ pulses as required.

### *3.4 Computer*

The equipment could be used with almost any general purpose, on-line, time-sharing computer providing a suitable interface is available.

Where the computer is only required for meter calibration it would be uneconomical to use a general-purpose machine; therefore, a special purpose computer has been designed and is described in the Appendix.

## 4. Conclusion

The calibration of turbine-type flowmeters can be carried out quickly and easily without any interruption of the metering process.

Calibration factors are applied automatically to the meter outputs to give immediate indication of meter throughput without tedious manual calculations.

## 5. Acknowledgments

The method of determining a volume of product using a calibrated section of the pipeline was developed by Pipeline Technologists (U.K.) Ltd. to whom thanks are due for the co-operation received throughout this project.

Figures 1 and 2 are reproduced with the kind permission of Fischer & Porter (Canada) Ltd.

The author would like to thank the Directors of Serck Controls Ltd. for permission to publish this paper.

## 6. Appendix: Special Purpose Computer

### *6.1 Central Processor*

Since much of the information used in the computation is available in binary coded decimal (b.c.d.) and decimal display of meter factor and flow rate is required, a b.c.d. arithmetic unit was decided upon.

As no great speed is required, a single cycle of the sphere in the prover taking at least $2\frac{1}{2}$ minutes, series–parallel arithmetic was chosen, each bit of a b.c.d. digit being operated on in parallel, with the b.c.d. digits processed serially.

Addition, subtraction, multiplication and division are required, therefore the arithmetic unit comprises

a full, single digit b.c.d. adder–subtractor capable of operating on two inputs $a$ and $b$ and a carry bit from a previous arithmetic operation. Replacement of results is into the source of $a$ or $b$.

All the arithmetic operations add, subtract, multiply and divide on full length numbers can be reduced to the basic operations add, subtract or shift on single digits of the numbers in a particular sequence, the shift function being the addition of zero to the digit being shifted, with replacement in a lower or higher digit position.

### *6.2 Basic Orders*

The basic functions of the arithmetic unit are:

F0—Add $a$ to $b$
F1—Subtract $b$ from $a$

The add function becomes a transfer when $a$ or $b$ are made '0'.

F2—Transfer $a$—($b$ inhibited)
—Transfer $b$—($a$ inhibited)

These orders are carried out on single b.c.d. digits.

### *6.3 Long Orders*

These are combinations of basic orders carried out in particular sequence to perform arithmetic on two multi-digit numbers $A$ and $B$, where $A$ and $B$ have 5 digits each $A_4A_3A_2A_1A_0$ and $B_4B_3B_2B_1B_0$.

#### 6.3.1. Add $A$ and $B$

The sequence of events is:

In interval P0—Add $A_0$ to $B_0$
,, ,, P1— ,, $A_1$ ,, $B_1$ and any carry from P0
,, ,, P2— ,, $A_2$ ,, $B_2$ ,, ,, ,, ,, P1
,, ,, P3— ,, $A_3$ ,, $B_3$ ,, ,, ,, ,, P2
,, ,, P4— ,, $A_4$ ,, $B_4$ ,, ,, ,, ,, P3

#### 6.3.2 Subtract $B$ from $A$

In interval P0—Sub. $B_0$ from $A_0$
,, ,, P1— ,, $B_1$ and any carry from P0 ,, $A_1$
,, ,, P2— ,, $B_2$ ,, ,, ,, ,, P1 ,, $A_2$
,, ,, P3— ,, $B_3$ ,, ,, ,, ,, P2 ,, $A_3$
,, ,, P4— ,, $B_4$ ,, ,, ,, ,, P3 ,, $A_4$

#### 6.3.3 Transfer $A$ to $B$

In interval P0—Add $A_0$ to 0 Replace in $B_0$
,, ,, P1— ,, $A_1$ ,, 0 ,, ,, $B_1$
,, ,, P2— ,, $A_2$ ,, 0 ,, ,, $B_2$
,, ,, P3— ,, $A_3$ ,, 0 ,, ,, $B_3$
,, ,, P4— ,, $A_4$ ,, 0 ,, ,, $B_4$

#### 6.3.4 Transfer $B$ to $A$

In interval P0—Add 0 to $B_0$ Replace in $A_0$
,, ,, P1— ,, 0 ,, $B_1$ ,, ,, $A_1$
In interval P2—Add 0 to $B_2$ Replace in $A_2$
,, ,, P3— ,, 0 ,, $B_3$ ,, ,, $A_3$
,, ,, P4— ,, 0 ,, $B_4$ ,, ,, $A_4$

#### 6.3.5 Multiply $A \times B$. Result in accumulator

This expands to $(A_4A_3A_2A_1A_0) \times (B_4B_3B_2B_1B_0)$ which can be written

$$\begin{array}{rll} A_4A_3A_2A_1A_0 & \times(B_0)+ & \text{PP0} \\ A_4A_3A_2A_1A_0 & \times(B_1)+ & \text{PP1} \\ A_4A_3A_2A_1A_0 & \times(B_2)+ & \text{PP2} \\ A_4A_3A_2A_1A_0 & \times(B_3)+ & \text{PP3} \\ A_4A_3A_2A_1A_0 & \times(B_4)+ & \text{PP4} \\ \hline C_9C_8C_7C_6C_5C_4C_3C_2C_1C_0 & & \end{array}$$

Each partial product PP is obtained by adding the multiplicand into an accumulator $B$ times, the product being built up as each partial product is accumulated. The sequence of events then is:

In cycle 0 (CY0) form the partial product PP0 by adding $A$ to the accumulator (C) $B_0$ times. This is a sequence as in 6.3.1 for the addition of $A$ to $B$ where $B$ becomes the accumulator $C$, therefore in

CY0 P0—Add $A_0$ to $C_0$
P1— ,, $A_1$ ,, $C_1$ and any carry from P0
P2— ,, $A_2$ ,, $C_2$ ,, ,, ,, ,, P1
P3— ,, $A_3$ ,, $C_3$ ,, ,, ,, ,, P2
P4— ,, $A_4$ ,, $C_4$ ,, ,, ,, ,, P3
P5— ,, $C_5$ ,, ,, ,, ,, P4

A check is then carried out by subtracting '1' from $B_0$ and testing the result for '0'. If it is not '0', a further full addition of $A$ into the accumulator is carried out and '1' is subtracted from $B_0$ again. The sequence is repeated until $B_0$ is reduced to '0' when the accumulator will hold PP0 and the next partial product can be started in CY1.

CY1 P0—Add $A_0$ to $C_1$
P1— ,, $A_1$ ,, $C_2$ and any carry from P0
P2— ,, $A_2$ ,, $C_3$ ,, ,, ,, ,, P1
P3— ,, $A_3$ ,, $C_4$ ,, ,, ,, ,, P2
P4— ,, $A_4$ ,, $C_5$ ,, ,, ,, ,, P3
P5— ,, $C_6$ ,, ,, ,, ,, P4

'1' is then subtracted from $B_1$ and $B_1$ tested as before to determine whether or not further additions are required. When $B_1$ has been reduced to '0' the accumulator holds PP0+PP1 and the next partial product is started in CY2.

These sequences are repeated for CY2, CY3 and CY4, at the end of which the accumulator holds the full double-length product.

#### 6.3.6 Divide $C/A$. Result in $B$

Division is achieved by using a non-restoring algorithm in which the divisor is first subtracted from

the dividend until the difference is negative, the number of subtractions being stored until a negative result is found, when the divisor is shifted to the right and added to the previously-found negative result a number of times until the result is positive. The number of additions is subtracted from the first number of subtractions until the positive result is found, when the divisor is shifted to the right and subtracted from the previous positive result. This is repeated five times.

As an example evaluate 5194 ÷ 2776.

| | | |
|---|---|---|
| | | + − + − |
| | | 2·2 8 9 = 2·080 − 0·209 = 1·871 |
| | | 2776)5 1 9 4− |
| 2 × 2776 Subtracted | | 5 5 5 2 |
| Result −ve | carry 1 | 9 6 4 2 0+ |
| 0·2 × 2776 Added | | 5 5 5 2 |
| Result +ve | carry 1 | 1 9 7 2 0− |
| 0·08 × 2776 Subtracted | | 2 2 2 0 8 |
| Result −ve | carry 1 | 9 7 5 1 2 0+ |
| 0·009 × 2776 Added | | 2 4 9 8 4 |
| | | 0 0 0 1 0 4 |

There are therefore five cycles during which the number in $A$ is subtracted from or added to that in the accumulator a number of times until a carry is generated. The number of additions or subtractions is subtracted or added to the result.

The sequence of events is therefore:

CY0 P0—Subtract $A_0$ from $C_4$
P1— ,, $A_1$ and any carry from P0 ,, $C_5$
P2— ,, $A_2$ ,, ,, ,, ,, P1 ,, $C_6$
P3— ,, $A_3$ ,, ,, ,, ,, P2 ,, $C_7$
P4— ,, $A_4$ ,, ,, ,, ,, P3 ,, $C_8$
Add 1 to $B_4$. Repeat until a carry occurs in P4.

CY1 P0—Add $A_0$ to $C_3$
P1— ,, $A_1$ ,, $C_4$ and any carry from P0
P2— ,, $A_2$ ,, $C_5$ ,, ,, ,, ,, P1
P3— ,, $A_3$ ,, $C_6$ ,, ,, ,, ,, P2
P4— ,, $A_4$ ,, $C_7$ ,, ,, ,, ,, P3
Subtract 1 from $B_3$. Repeat until a carry occurs in P4.

These cycles are repeated up to CY4, at the end of which register $B$ holds the required quotient.

### 6.4 Master Sequence

Inspection of the sequences of basic orders used for the various long orders indicates that all long orders can be based on a master set of sequences as follows:

| *Interval* | *Instruction* |
|---|---|
| P0 | Add/Sub $A_0$ and $B_x$ |
| P1 | ,, ,, $A_1$ ,, $B_{(x+1)}$ |
| P2 | ,, ,, $A_2$ ,, $B_{(x+2)}$ |
| P3 | ,, ,, $A_3$ ,, $B_{(x+3)}$ |
| P4 | ,, ,, $A_4$ ,, $B_{(x+4)}$ |
| P5 | ,, ,, $A_5$ ,, $B_{(x+5)}$ |
| P6 | ,, ,, 1 ,, $B_x$ |
| P7 | ,, ,, 1 ,, $B_{(y+1)}$ |
| P8 | ,, ,, 1 ,, $B_{(y+2)}$ |
| P9 | ,, ,, 1 ,, $B_{(y+3)}$ |
| P10 | ,, ,, 1 ,, $B_{(y+4)}$ |

Adoption of the master set of sequences permits the use of a relatively simple basic timing arrangement to control all the orders in the computer.

#### 6.4.1 Single cycle orders

For ADD, SUBTRACT and TRANSFER long orders, only intervals P0 to P4 are used, P5 to P10 being jumped and $x$ is '0'. There is only one cycle P0 to P4 for each order.

#### 6.4.2 Multiplication

In MULTIPLICATION, to produce PP0, intervals P0 to P5 are used, addition taking place between $A$ and the accumulator, therefore $B$ in the master sequence list is made to be the accumulator address.

Having added $A$ into the accumulator, $B_0$ is reduced by 1 in P6 and a check made for $B_0$ being zero.

Intervals P7 to P10 are jumped and $x$ and $y$ are zero.

When PP1 is being produced intervals P0 to P5 are again used as for PP0. In P7, $B_1$ is reduced by 1. Intervals P6 and P8 to P10 are jumped, $x$ is 1 and $y$ is zero. The remaining partial products are formed in the same way, with $x$ being increased for each PP.

### 6.4.3 Division

For DIVISION, in CY0 P0 to P4, subtraction of $A$ from the accumulator is carried out, followed in P10 by the addition of 1 to $B_4$. The subtraction is repeated until the result goes negative, with 1 added to $B_4$ each time. Intervals P0 to P4 are used, P5 to P9 jumped, P10 used and $x$ and $y$ are zero.

In CY1 P0 to P4, $A$ is added to the accumulator, with 1 subtracted from $B_3$ in P9, any carry resulting from the subtraction being taken from $B_4$ in P10.

Intervals P0 to P4 are used, P5 to P8 jumped, P9 and P10 used and $x$ and $y$ are zero.

These alternating sequences of subtraction and addition are repeated in CY2 to CY4.

*Manuscript first received by the Institution on 19th June 1969 and in final form on 2nd December 1969. (Paper No. 1304/IC20.)*



## The Author

**Peter Ridley** (M. 1969; G. 1964) received his technical education at Carlisle Technical College and at the Heriot-Watt College, Edinburgh. He passed Part A of the Institution's Graduateship Examination in November 1961, being awarded the S. R. Walker Prize as the outstanding candidate of that year; in May 1964 he succeeded in Part B of the Examination. In 1964 Mr. Ridley received an appointment with Serck Controls Ltd. of Leamington Spa, Warwickshire, as a design engineer and was promoted to senior engineer in 1968. He joined the scientific staff of Northern Electric Research and Development Laboratories, Ottawa, Ontario, last July. Mr. Ridley was transferred to Corporate Membership of the Institution in March 1969 and in July he registered as a Professional Engineer (P.Eng.) with the Association of Professional Engineers of Ontario.

# LECO'70—London Engineering Congress, 1970

The most comprehensive engineering congress ever held in Great Britain, if not in the world, opens at the Royal Festival Hall, London, on 4th May 1970. The theme of the Congress is "The Challenges facing the Engineering Profession in its Services to the Community". Speakers have been invited from industry, public corporations, municipal authorities, government departments, the universities and other education authorities, research organizations and the trade unions.

LECO'70 is being organized by the Council of Engineering Institutions, which has co-ordinated the resources of its 14 chartered engineering institution members—representing over 250,000 professional engineers—planning the Congress. The scale of the Congress is such as to attract world wide attention and a substantial attendance from overseas is expected. Already over 2,000 requests for registration forms, including more than 350 from 41 countries have been received.

The Opening Address will be given by the Minister of Technology on Monday, May 4th. H.R.H. The Duke of Edinburgh, President of C.E.I., will close the congress on May 7th and will present the first Mac-Robert Award medals at this time.

The Congress opens at the Royal Festival Hall, London, on 4th May 1970 with an afternoon Registration of Delegates, followed by the Opening Address, and an evening Conversazione and buffet supper. On each of the three subsequent days the mornings will be devoted to Plenary Sessions for all delegates. The afternoon sessions will be more detailed and divided into eight groups covering individual engineering topics.

Plenary Session subjects are:

*Innovation and Industrial Growth and their Consequences in Human Terms.*

Speakers: Lord Nelson, Chairman, G. E. and E. E. Companies Ltd., P. G. Masefield, Chairman, British Airports Authority; Dr. F. E. Jones, Managing Director Mullard Ltd.; and I. Maddock, Controller Industrial Technology, Ministry of Technology.

*New Engineering Materials and Design.*

Speakers: Prof. J. E. Gordon, Professor of Materials Technology, University of Reading and Dr. H. M. Finniston, Deputy Chairman, British Steel Corporation.

*Conservation and Development of Resources.*

Speakers: N. A. F. Rowntree, Director, Water Resources Board and Dr. A. Parker, Chemical Engineering Consultant.

*International Co-operation (including work in developing countries metrication, standards and quality assurance).*

Speakers: Sir Frederick Warner, Messrs. Cremer and Warner, and G. B. R. Feilden, Deputy Director, B.S.I.

*Education of the Engineer and Engineering Manpower Deployment.*

Speakers: Sir Arnold Lindley, Chairman, E.I.T.B., and Sir Derman Christopherson, Vice-Chancellor, University of Durham.

A total of 28 Group Sessions covers the whole engineering spectrum from microelectronics to ship design, from instruments to hovercraft, from motorways to computers, from petro-chemicals to exploiting the sea bed in search of minerals.

The seven papers to be presented in the Group I Sessions have been arranged jointly by the I.E.R.E. and the I.E.E. Details of these papers will be given in the March issue of the *Journal*.

The two final Group Sessions are of interest to all engineers and these will be held as parallel Combined Sessions for general attendance by delegates on Thursday afternoon, May 7th.

The first of these Sessions is on Education and Training and the papers are:

'*Education and deployment: a survey of* 10 *years' output of engineers and applied scientists*' by
Prof. A. S. Roberts, University of Leeds.

'*Education of engineers for managing innovation*' by
Prof. B. Downs, Loughborough University.

The two papers to be presented in the Combined Group Session on Quality Assurance Standards and Metrication are:

'*Some responsibilities of government for standardization and quality assurance*' by
A. H. A. Wynn, Head of Standards Division, Ministry of Technology.

'*Standards and metrication*' by
T. A. L. Paton, Sir Alexander Gibb and Partners.

Throughout the Congress the accent will not only be on current developments in various engineering disciplines but also their impact on society, on the new challenges facing the engineer and his own changing role in society, and how the growing interdependence of different engineering disciplines may best be developed to the National advantage.

The Chairman of the Organizing Committee of LECO'70 is Sir Eric Mensforth, C.B.E., M.A., D.Eng., C.Eng., the recently elected Chairman of C.E.I. for 1970. The I.E.R.E. representative on the Papers Committee is Dr. G. L. Hamburger, C.Eng., a member and past chairman of the Institution's Programme and Papers Committee.

Intending delegates may obtain a preliminary programme booklet, which includes a registration form, from LECO'70 Congress Office, c|o Institution of Production Engineers, 10 Chesterfield Street, London, W1X 8DE.